Optical Cellular Delivery and Intracellular Sensing of fN Forces Using Gold Nanoparticles

Miao Li

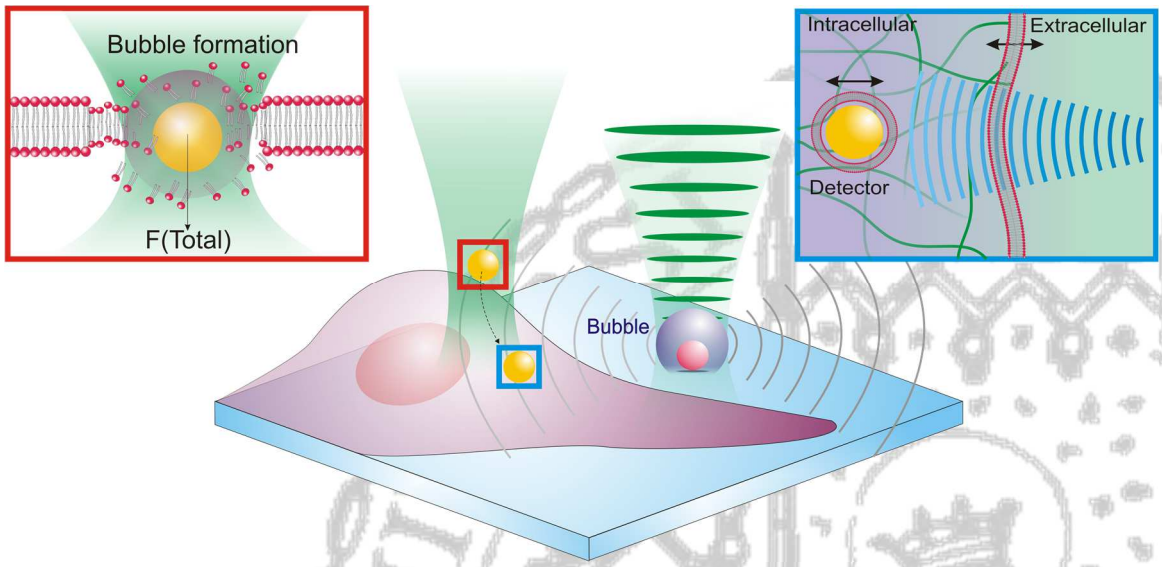

München 2016

Optical Cellular Delivery and Intracellular Sensing of fN Forces Using Gold Nanoparticles

Miao Li

München 2016

Optical Cellular Delivery and Intracellular Sensing of fN Forces Using Gold Nanoparticles

Miao Li

Dissertation

an der Fakultät für Physik

der Ludwig-Maximilians-Universität

München

vorgelegt von

Miao Li

aus Kunming, China

München, 29th April 2016

Erstgutachter: Prof. Dr. Jochen Feldmann

Zweitgutachter: Prof. Dr. Joachim Rädler

Tag der mündlichen Prüfung: 21st June 2016

Cover image: Optically injecting a gold nanoparticle into a living cell for probing the force pulses optothermally generated in the vicinity of the cell

Publications and Contributions to Conferences and Workshops

Scientific publications of the results in this work:

- M.Li, T. Lohmüller and J. Feldmann
  Optical Injection of Gold Nanoparticles into Living Cells
  Nano Letters, 15, 770−775 (2015)
- M.Li, C. Zensen, T. Lohmüller and J. Feldmann
  Measuring fN force using gold nanoparticles in living cells. In preparation

Conferences and workshops:

- Oral presentation “Optical injection of gold nanoparticles into living cells”
  Workshop on Photonics and Optoelectronics, Hirschegg-Kleinwalsertal, Austria. September/October 2014
- Poster presentation “Optical injection of gold nanoparticles into living cells”
  CeNS Workshop Venice 2014 "Walk and Talk at the Nanoscale", Venice, Italy. September 2014
- Oral presentation “Optical printing and injection of gold nanoparticles into living cells”
  "Biosensing and Nanomedicine VII", SPIE Optics + Photonics Symposium 2014, San Diego, U.S. 17th August 2014

Acknowledgement

First and foremost, I would like to thank **Professor Jochen Feldmann**, my supervisor and the Chair of Photonics and Optoelectronics group (PhOG) in LMU München, for giving me the opportunity to conduct research in his excellent group. I am grateful for every productive discussion we had and all his supports both scientifically and personally. It has been a great honor for me to be one of his Ph.D. students and to work with him for three years.

Many thanks to my Ph.D. advisor **Dr. Theobald Lohmüller**, for his contribution as a subgroup leader and every single helpful discussion about projects and problems.

Thanks also to **Professor Joachim Rädler** for providing the cell culture facilities and **Gerlinde Schwake**, **Susanne Kempter**, and **Peter Röttgermann** for providing technical supports in cell, which keeps my research projects going well.

Thanks go to my colleague **Carla Zensen** for the excellent teamwork. I appreciate her sound knowledge of theoretical modeling and programming, as well as the fruitful discussions and her helpful suggestions.

I would also like to thank **Dr. Alexander Urban** and my sub-group members **Christoph Maier, Patrick Urban,** and **Carla Zensen,** for their efforts and time in proof-reading and correcting of my thesis.

Express thanks also to my former and current roommates: **Dr. Wei Li**, **Dr. Michael Fedoruk**, **Anastasia Babynina**, **Christoph Maier**, **Jasmina Sichert** and **Yu Tong**, for their help in all aspects and pleasures we had together. Thanks to **Patrick Urban** for his supports in IT, to **Dr. Spas Nedev** who help me a lot personally, to **Dr. Jaekwon Do** for his tips in doing Ph.D. research, to my Chinese friends: **Dr. Ming Fu**, **Dr. Tianyue Zhang**, **Dr. Yongzheng Xing**, **Fang Zhou** and **Tao Zhang** for the relaxing time we spent together.

I would further like to thank our secretary **Gerlinde Adam**, technicians **Stefan Niedermaier**, **Martin Vogel**, **Christian Holopirek** and **Katja Lyons** for their bureaucratic and technical supports during my Ph.D. research. Moreover, of course, thanks to all Ph.D., Master, Bachelor students in this group for providing a very friendly and pleasant atmosphere for any help they provided me. Thanks to the whole **PhOG** who provides me an excellent international working environment that I have a chance to work with people from every continent of the world. This is an amazing experience that I will never forget in my life.

Last and most certainly not least I wish to thank my **family** in China, for their endless love and support.

Table of Contents

Kurzfassung

Gold-Nanopartikel sind in den vergangenen Jahren zu einem wichtigen Werkzeug der Nanowissenschaften geworden. Die starke Kopplung zwischen sichtbarem Licht und Goldnanopartikeln verursacht zum einen eine große nichtradiativen Energieumwandlung, das sogenannte plasmonische Heizen, welches einen kontrollierbaren Temperaturanstieg in der Partikelumgebung ermöglicht. Zum anderen wirken auf Goldnanopartikel optische Kräfte, die für deren optische Manipulation genutzt werden können. In dieser Dissertation wird gezeigt, wie diese Effekte für das Injizieren einzelner Nanopartikel in Zellen sowie für intrazelluläre Messungen verwendet werden können.

Zuerst wird eine neuartige Methode, um Goldnanopartikel (80nm Durchmesser) in lebende Zellen einzubringen, vorgestellt. Dazu werden diese zuerst durch optische Kräfte mit einem fokussierten Laserstrahl auf die Oberfläche lebender Zellen aufgebracht. Anschließend können die Goldnanopartikel einzeln durch eine Kombination aus plasmonischem Heizen und optischen Kräften injiziert werden. Der Prozess wurde sowohl durch chemische, als auch durch optische Methoden charaktierisiert. Weiter wurde beobachtet, dass die erfolgreiche Partikelinjektion mit der Ausbildung einer Kavitationsblase einhergeht, welche eine Perforation der Zellmembran verursacht. Die Überlebensrate der Zellen für diesen Prozess lag dabei bei über 70%.

Der zweite Teil dieser Arbeit beschäftigt sich mit der Nutzung von Goldnanopartikeln, welche in lebende Zellen entweder injiziert oder durch Endozytose eingeschleust wurden, als Messsonden durch Fourieranalyse ihrer Trajektorien. Durch das periodische Heizen eines Goldnanopartikels in Zellnähe wird eine Kavitationsblase erzeugt, die einen periodischen Kraftübertrag auf die Zelle verursacht, was zu Nicht-Gleichgewichts Fluktuationen der Detektorpartikel in der Zelle führt. Die spektrale Leistungsanalyse der Partikelbewegung gibt sowohl Aufschluss über die physikalischen Eigenschaften der Partikelumgebung, als auch über die Größe der wirkenden Kraft.

Abstract

Gold nanoparticles (AuNPs) have emerged as a powerful tool in nanoscience. The light-AuNP interaction gives rise to several applications, among which the plasmonic heating and optical forces have received great interest. The former enables the controllable increase of the temperature at the gold nanoparticle surface, while the latter allows for the remote manipulation of a single gold nanoparticle using light. This thesis presents studies on how these properties can be used in the application of single particle cellular delivery and intracellular sensing.

First, a novel optical way to deliver the gold nanoparticles to a single living cell is presented. It is shown that the individual gold nanoparticles (80 nm in diameter) can be patterned on the surface of living cells with a continuous wave laser beam. Then, these optically printed gold nanoparticles can be injected into the cell, one-by-one, through a combination of plasmonic heating and optical forces. Both chemical and optical methods were used to characterize the optical injection process. It was also found that successful optical injection was achieved by the generation of bubbles that perforated the cell membrane. The cell survival rate was maintained above 70% during the injection process.

Second, this study shows how gold nanoparticles that were injected or endocytosed into a living cell were used as detectors and precisely readout the local perturbations by Fourier analysis of their motions. The perturbations were generated by heating a gold nanoparticle that was sitting in the vicinity of the cell using a chopped laser beam. The heating induced the periodic formation of a cavity bubble around the particle and sent out a series of force pulses that were applied to the cell, causing non-equilibrium fluctuations to the movement of the detector particles inside the cell. We demonstrate that the power spectral analysis of particle motion reveals the physical characteristics of the nanodetector environment and the quantity of the applied force.

Abbreviations

AFM	Atomic force microscopy
ATCC	American Type Culture Collection
AuNPs	Gold nanoparticles
CCD	Charge-Coupled Device
CCR	Clausius-Clapeyron Relation
CHO	Chinese hamster ovary
CO_2	Carbon dioxide
CW	Continuous wave
DFM	Dark field microscopy
DMSO	Dimethyl sulfoxide
EDTA	Ethylenediaminetetraacetic acid
EthD-1	Ethidium Homodimer-1
FCS	Fetal Bovine Serum
FFT	Fast Fourier transformation
fN	Femtonewton
fps	Frame per second
FWHM	Full width at half maximum
LSPR	Localized surface plasmon resonance
MSD	Mean square displacement
NA	Numerical aperture
PC	Phosphatidylcholine
PE	Phosphatidylethanolamine

PI	Phosphatidylinositol
pN	Piconewton
PS	Phosphatidylserine
PSD	Power spectral density
RME	Receptor-mediated endocytosis
rpm	Revolutions per minute
SD	standard deviation
SERS	Surface enhanced Raman spectroscopy
SM	Sphingomyelin
SPT	Single particle tracking

Chapter 1

Introduction

Gold nanoparticles (AuNPs) have a long history of use, dating back to Roman times when people stained glass, ceramics, enamel pottery, and clothes with metallic nanoparticles[1]. Throughout this long period however, there was no understanding of the mechanisms that give rise to the colors of the small metal particles until 1908[2], when the German physicist Gustav Mie quantitatively explained the size-dependent optical properties of metal spheres, and a clear mathematical foundation was established. Currently, with the development of various methods for the controlled synthesis and functionalization of materials on the nanoscale, gold nanoparticles have attracted considerable interest as a novel platform for the development of nanotechnology and nanomedicine[3-6].

The interest in gold nanoparticles comes from their unique properties when interacting with light. One of the most important characteristics of gold nanoparticles is the localized surface plasmon resonance (LSPR; *i.e.,* the resonant oscillation of free electrons in the gold upon interacting with incident light[7]). This interaction results in some fundamental effects electrically, optically, and thermally around the gold nanoparticle, which has found numerous applications in imaging and therapeutic aspects. For example, the enhanced electrical fields around the gold nanoparticles have been applied to surface-enhanced Raman spectroscopy (SERS), which allows the gold nanoparticles to be used for sensing intracellular molecules[8-10] or monitoring drug metabolism in living cells[11]. The enhanced absorption cross-section of the gold nanoparticles enables their use as an ideal nanoscopic heat source. A gold nanoparticle absorbs light efficiently at the particle plasmon resonance, which leads to a strong local temperature rise within picoseconds of irradiation with laser light[12, 13]. This strong increase in temperature of the gold nanoparticles on a nanoscopic scale has already found applications that range from nanomaterial fabrication[14] to cancer thermal therapy[15, 16]. One of the most extensively

studied thermal responses of laser heated gold nanoparticles is the water vaporization around the gold nanoparticle (*i.e.* bubble formation). It is suggested that the surface temperature of a gold nanoparticle can easily surpass the water boiling point under laser irradiation[17, 18], when water around the gold nanoparticle becomes superheated until bubbles form from an explosive boiling during water spinodal decomposition. This process has been used for enhanced image contrast and gene delivery[19-21]. In addition, the enlarged amount of light scattering and absorbing properties of the gold nanoparticle also leads to enhanced photon momentum transfer to the particle (*i.e.,* optical forces), which enables the spatial and temporal control of gold nanoparticles and has enabled applications in material science[22-24] and biological science[25, 26].

Among all of the biological applications of gold nanoparticles, including imaging, biosensing, and drug delivering, the particles must be in contact with living cells or sent into the interiors of the cells to act as handles for cellular manipulation. However, this is not a natural process since the cell membrane is almost impermeable to large molecules or particles, which makes active nanoparticle delivery across the membrane barrier difficult. Current biochemical strategies primarily employ carrier molecules such as dendrimers[27], liposomes[28], and polymers[29] for cell transfection, but most of these strategies are only capable of treating an entire population of cells simultaneously. To achieve more controllable cellular delivery for precise intracellular measurement or sensing, a strategy for a single particle delivery to a single cell at one time is required.

Since the first presentation of the 'gene gun'[30], there have been a number of studies investigating possible mechanisms for single cell molecular delivery (e.g., physical means such as electroporation[31], sonoporation[32], and optical approaches using laser light[33, 34]). For optical methods, living cells are usually treated with a tightly focused pulse laser beam, which generates a transient hole in the cell membrane. Small molecules, such as nucleic acids[35-37], drugs[38], and nanoparticles[39], are allowed to diffuse passively into the cell through the hole that remains open for a short period of time. Although such laser-assisted photoporation is contactless, efficient, and specific (i.e., cells can be singled out from an entire cell population), the generation of membrane pores, however, requires nano- to femtosecond laser pulses which have high peak intensities. It therefore imposes a potential threat to cell viability through photodamage. In the study that is presented in

this thesis, the gold nanoparticles, not only as intracellular manipulation handles but as themselves, can provide a solution to establishing a less harmful approach for light-assisted optical cellular delivery by taking advantage of their plasmonic properties. As mentioned above, the drastic increase in temperature of gold nanoparticles upon laser irradiation can lead to an increase in membrane permeability[40, 41] or the formation of nanobubbles[20, 42, 43], which results in mechanical disruption of the cell membrane and the formation of pores[44]. These effects have successfully been used for laser-induced gene transfection of eukaryotic cells[21, 45, 46] through the photoporation of cell membranes with localized heating[47, 48] or laser-mediated cavitation[49, 50]. Gold nanoparticles, at the same time, are also subject to optical forces when they are irradiated with a focused laser beam[22, 51]. In other words, a gold nanoparticle can be pushed and heated simultaneously under the illumination of a resonance laser beam. These combined properties have been used to inject gold nanoparticles into lipid vesicles (GUVs) [52]. However, to date, it has not been achieved to inject a single nanoparticle directly into living cells by using a single cw laser beam. The first experimental part of this thesis demonstrates how to use light to guide the gold nanoparticles to the surface of a living cell and overcome the barrier of a cellular membrane to optically insert a single gold nanoparticle into the cell.

Gold nanoparticles have also been widely applied as biosensors to study various micro-scale or nano-scale processes[53-55]. In a recent study, Ohlinger *et al.* first introduced the concept of the 'nano-ear', which is capable of detecting the vibrations of fluid on microscopic length scales with an estimated sensitivity that is six orders of magnitude below the threshold of human hearing[56]. The principle of this concept was based on the Fourier analysis of the motions of an optically trapped gold nanoparticle with a response to the acoustic vibrations. The vibration was created by the periodical plasmonic heating of the gold nanoparticles in close vicinity of the optical trap. Since this vibration is a result of a series of mechanical force pulses that are sent through the liquid, if this concept can be applied to living cells, it will provide a novel approach to studying cell mechanics. Recent reports have shown that the mechanical stimulation of living cells plays an important role in regulating essential cellular processes[57, 58]. For instance, externally applied forces are increasingly recognized as major regulators of cell structures and functions and are capable of changing gene expression[59], altering cell migration[60, 61], influencing stem cell differentiation[62, 63], and regulating disease states[64, 65]. However, how

these forces apply and propagate through different intracellular structures and across the cell membrane is not yet well understood. The measurement of these forces in a single cell requires tools with unique spatial resolution and sensitivity.

Force spectroscopy has become a powerful tool for investigating the force and displacement properties of biomolecules. Techniques such as atomic force microscopy (AFM), magnetic tweezers, and optical tweezers are currently employed to measure and apply forces to a single biomolecule[66]. However, challenges still exist when performing the same or similar measurements in living cells due to the crowded, inhomogeneous, and sensitive physiological conditions that are found in the interior of the cells. AFM requires a physical probe, which is not applicable to intracellular measurements under normal circumstances. The large size and relatively high stiffness of the cantilevers 10–10^5 (pN/nm), which impose a large minimal force (10 pN), make it difficult to study the forces that are associated with many biological processes and structures[67]. Moreover, a direct mechanical contact between the AFM probe and the cell increases the possibility of physical damage[68, 69]. Magnetic and optical tweezers are less invasive manipulation techniques and possess good measurement throughput (30 cells per hour)[70], but the former is only for unidirectional force measurement and requires micro-sized bead as a probe[71], while the latter increases the risk of localized heating or photodamage since the cells are exposed to a long period of laser illumination[72]. In addition, applying *in vitro* calibrated optical tweezers to the in *vivo* measurement is challenging since the presence of cellular structures will lead to variations in the refractive index around trapped particles, resulting in changes in the spring constant of the tweezers with respect to the viscous medium[26]. Although it is possible to calibrate the optical trap directly in the cytoplasm[73], this method still requires multiple steps and can only achieve the measurement at one randomly selected position at one time[74, 75].

The second experimental part of this thesis demonstrates a new concept: how gold nanoparticles can be used as external signal sources and intracellular biosensors to locally apply and detect forces in living cells. This method uses an indirect and contactless method of force manipulation of living cells, which is more simple, efficient, and sensitive than conventional tools of trade.

This thesis starts with an introduction to the theoretical foundations that are related to these studies. Chapter 2 presents fundamental knowledge for understanding the experiments in this thesis. The chapter begins with a section that discusses light-AuNP interactions, including a series of physical responses of the gold nanoparticles to the light. The localized surface plasmon resonance of the gold nanoparticles is discussed in detail. Plasmonic heating and optical forces are also introduced in this part. This information is essential knowledge for understanding the experiments on laser printing and the injection of gold nanoparticles into a living cell as discussed in Chapter 4. The following sections primarily describe the physical principles of the motion of particles. This provides a general understanding of the experiments in Chapter 5.

Chapter 3 describes the experimental setups and methods. The working principles of a dark field microscope and a fluorescence microscope and their accessories that were used in this work are introduced. In the sections of the experimental methods, the techniques for basic cell culture and single gold nanoparticle optical manipulations are described.

The main experimental parts of this thesis are described in Chapter 4 and Chapter 5. Chapter 4 describes a novel way to optically deliver gold nanoparticles to the cell membranes and then inject the single gold nanoparticle into the living cell using a focused laser beam. The optical injection mechanisms are discussed in detail. The second experimental part (Chapter 5) focuses on the application of gold nanoparticles inside of the living cells. The idea is to use intracellular gold nanoparticles as biosensors to probe the fN forces, which are optothermally generated outside of the cell by plasmonically heating a gold nanoparticle with a modulated laser beam to induce the formation of the bubbles. The significance of this experiment is to achieve sensitive force spectroscopy in *vivo* by providing an elegant way to apply and probe the external forces inside of the cell at the single particle level, thus offering broad applicability for investigating the heterogeneous nature of intracellular processes.

The last chapter 6 briefly concludes the work of my Ph.D. thesis and provides an overview of the possible prospects of this research.

Chapter 2

Fundamentals

This chapter starts with an introduction of the fundamental theoretical background that is relevant to this thesis. Section 2.1 discusses the theory of light-metal interactions. How a gold nanoparticle responds to electromagnetic waves on the basis of the dielectric function of gold is illustrated. The localized surface plasmon resonance that is excited on the gold nanoparticle is discussed in detail as well. Theories on how a gold nanoparticle can convert light into heat and how optical forces are generated on the gold nanoparticle are also introduced. These theories are important for understanding the laser printing and injecting of a gold nanoparticle into a cell. This section is followed by a short section about the interactions of gold nanoparticles and living cells. The natural barrier ability of the cell membrane and endocytosis pathway is introduced. This section provides knowledge that will be useful when reading about the following concepts: how the detector particles enter the cell and why it is necessary to develop new cellular delivery strategies. In the last section, the fundamentals of the motion of particles are introduced. The analytical tools that were used in Chapter 5 are discussed in detail.

2.1 Interactions of Gold Nanoparticles and Light

The interaction of light with metallic nanoparticles gives rise to special properties. Incident electromagnetic waves can induce the collective oscillation of free electron gas in gold, which is known as a localized surface plasmon in gold nanoparticles. Depending on the size and shape of the gold nanoparticles, the plasmons show a resonance behavior with light at a broad peak frequency. The absorption of light results in a rapid temperature increase at the gold nanoparticle surface and the optical forces on the particle. This section begins with an explanation of the localized surface plasmon resonance of gold nanoparticles and then discusses the optical and thermal properties of gold nanoparticles in detail.

2.1.1 Localized Surface Plasmon Resonance of Gold Nanoparticles

The dielectric function of gold and the plasma frequency

The relationship between the incident electromagnetic wave and the irradiated metal structure can be described by the dielectric function of the metal. This function is based on the free electron model, which is also known as the Drude–Sommerfeld model[76]; this model assumes that the valence electrons of the metallic particle are detached from their positive ion cores, forming free electron gas. Therefore, only the collisions between free electrons and the surrounding atomic nuclei are taken into account. The dielectric function ε_r builds a connection between the external electromagnetic field and the dielectric response of the free electron gas:

$$\varepsilon_r(\omega) = 1 - \frac{\omega_p^2}{\omega^2 + i\gamma\omega} \tag{2.1},$$

where ω is the frequency of the external electromagnetic field and $\gamma = 1/\tau$ is the collision frequency, which describes the damping of electrons by collisions with atomic

nuclei. τ is known as the relaxation time of the free electron gas, which is typically in the order of 10^{-14} s for gold at room temperature, corresponding to $\gamma = 100$ THz[76].

Here, ω_p is the plasma frequency of the free electron gas, which is the natural property of a material and provides a deeper physical understanding of the optical material properties; when $\omega > \omega_p$, the collective motion of electrons cannot follow the rapid oscillation of the external electric field, resulting in light passing through the material without interactions. If $\omega < \omega_p$, the electric field is slow enough to interact with the oscillating electrons, and this results in the reflection and the absorption of light by the material.

Localized surface plasmon resonance

When light is incident on a metallic nanoparticle, the electrons inside of the particle oscillate in response to the oscillating electromagnetic field. The curved surface of a nanoparticle provides an effective restoring force to the driven electrons that results in a resonance, if the frequency of the applied electric field is close to the plasma frequency of the collective electron oscillation. This resonance is called 'localized surface plasmon resonance', a diagram of which is shown in **Figure 2.1**. An electromagnetic wave with a certain frequency, ω, irradiates a gold nanoparticle with dielectric function $\varepsilon_r(\omega)$, which is surrounded by the medium with dielectric constant ε_m and polarizes it. Meanwhile, another electromagnetic wave is induced around the gold nanoparticle because of the driven oscillation of electrons inside of the gold nanoparticle.

Quasi-static approximation

The simplest model for analyzing the interaction of a nanoparticle with the electromagnetic field is the quasi-static approximation[76]. The assumption is that the size of the particle is much smaller than the wavelength of an incident light, such that the phase of the incident beam is constant over the entire volume of the nanoparticle.

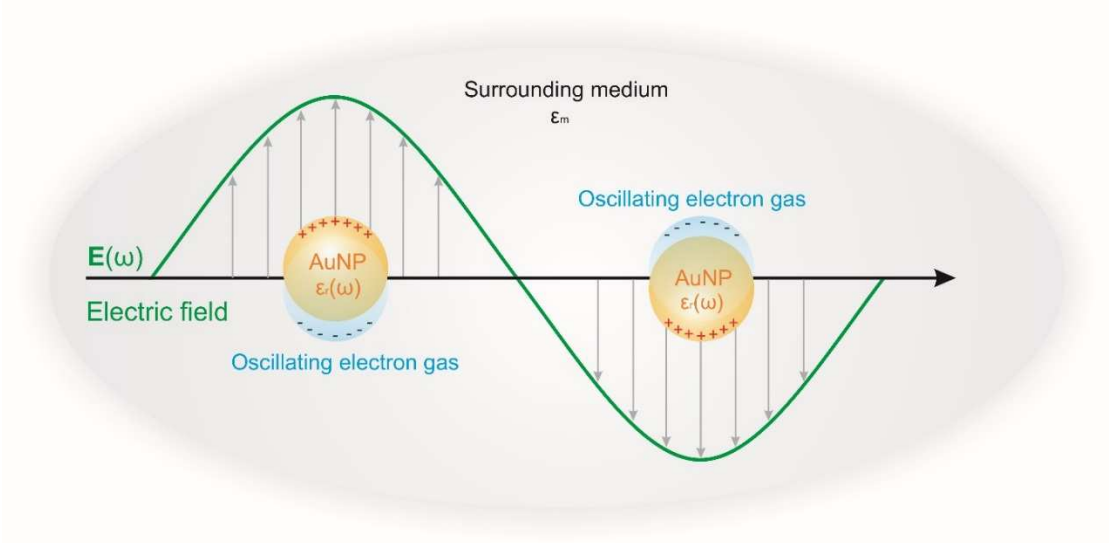

Figure 2.1 | The formation of a localized surface plasmon in the gold nanoparticle

Through analysis with the simplest geometry, a homogeneous and isotropic sphere with radius a and dielectric function $\varepsilon_r(\omega)$, located in the isotropic medium with a dielectric constant ε_m, the complex polarizability α of a small sphere of sub-wavelength in diameter in the electrostatic approximation[76] can be obtained:

$$\alpha = 4\pi a^3 \frac{\varepsilon_r(\omega) - \varepsilon_m}{\varepsilon_r(\omega) + 2\varepsilon_m} \qquad (2.2).$$

This equation has the same functional form as the Clausius–Mossotti relation and shows that the polarizability of a metal nanoparticle is dependent on the wavelength of incident light, as the dielectric function is related to the frequency of light. This equation also indicates a strong dependence of the resonance frequency on the dielectric constant of the surrounding medium (i.e., the resonance red shifts with increasing ε_m), which suggests that metal nanoparticles are ideal candidates for sensing changes in the refractive index of the medium, an application of which is presented in Chapter 3.

However, the quasi-static approximation is not justified for a particle with a larger size as the phase changes of the driving field become significant over the large particle volume. Thus, a more precise approach is required.

Extended quasi-static approximation

As discussed above, the quasi-static approximation breaks down when applied to larger particles because of the retardation effects over the larger volume of the particle; there is another expression for the polarizability of a metallic nanoparticle with volume V (V is valid for all particle sizes). It is a straightforward expansion of the first transverse electromagnetic mode (TEM) of the Mie theory[77]:

$$\alpha = \frac{1 - \left(\frac{1}{10}\right)[\varepsilon_r(\omega) + \varepsilon_m]x^2 + O(x^4)}{\left[\frac{1}{3} + \frac{\varepsilon_m}{\varepsilon_r(\omega) - \varepsilon_m}\right] - \frac{1}{30}[\varepsilon_r(\omega) + 10\varepsilon_m]x^2 - i\frac{4\pi^2\varepsilon_m^{3/2}}{3}\frac{V}{\lambda^3} + O(x^4)} \times V \qquad (2.3).$$

In this equation, a significant difference compared to the quasi-static approximation is the quadratic term in the numerator and the denominator, which includes the retardation effect of the electromagnetic field over the volume of the nanoparticle that leads to the shift of the plasmon resonance. The polarizability for the optical force calculation in this thesis is obtained from this equation.

Mie theory

In 1908, Gustav Mie developed a theory that addresses the scattering and absorption of an electromagnetic wave by a spherical particle to explain the colors of colloidal gold particles in the solution[78]. This theory provides a solution for light scattering by a sphere particle, which is embedded in a homogeneous and isotropic medium that is illuminated by a plane wave and is valid for all nanoparticle sizes and optical wavelengths because the dipole contribution is considered as well as the contribution of higher orders of multiple expansions. Here, an important physical quantity is introduced: the cross-section, which can be defined as the net rate at which electromagnetic energy (W_{abs} or W_{abs}) crosses the surface of an imaginary sphere that is centered on the particle, divided by the

intensity of incident irradiance (I_{inc})[79]. Thus, the absorption (C_{abs}) and scattering cross-section (C_{scat}), respectively, can be written as follows:

$$C_{\mathrm{abs}} = \frac{W_{abs}}{I_{inc}} \tag{2.4}$$

$$C_{\mathrm{scat}} = \frac{W_{sca}}{I_{inc}} \tag{2.5}.$$

The sum of equations (2.4) and (2.5) is the extinction cross-section (C_{ext}). It represents the amount of energy that is removed from the incident field because of absorption and scattering by the particle:

$$C_{ext} = C_{abs} + C_{scat}. \tag{2.6}$$

Using the boundary conditions for the electromagnetic field at the edge of the particle, equations (2.4) and (2.5) can be extended to[80]:

$$C_{scat} = \frac{2\pi}{|k|^2}\sum_{n=1}^{\infty}(2n+1)(|a_n|^2 + |b_n|^2) \tag{2.7}$$

$$C_{ext} = \frac{2\pi}{|k|^2}\sum_{n=1}^{\infty}(2n+1)Re(a_n + b_n) \tag{2.8},$$

where k is the wave vector of the incident electromagnetic wave, a_n and b_n are the Mie-coefficients from the multipole expansions, and n is the multipole order ($n = 1$ corresponds to the dipole mold). The Mie-coefficients are as follows[80]:

$$a_n = \frac{m\psi_n(mx)\psi_n'(x) - \psi_n(x)\psi_n'(mx)}{m\psi_n(mx)\xi_n'(x) - \psi_n(x)\xi_n'(mx)} \tag{2.9}$$

$$b_n = \frac{m\psi_n(mx)\psi_n'(x) - m\psi_n(x)\psi_n'(mx)}{m\psi_n(mx)\xi_n'(x) - m\psi_n(x)\xi_n'(mx)} \tag{2.10}$$

where $x = 2\pi a/\lambda$, the size parameter of the particle of radius a irradiated with light at wavelength λ; m is the ratio of the complex refractive index of the particle and the surrounding medium; and the Riccarti-Bessel functions are ψ_n and ξ_n. In this thesis, the cross-section of the gold nanoparticles was calculated using the program MQMie. An example in **Figure 2.2** illustrates that the cross-section presents size dependency and is sensitive to the surrounding medium.

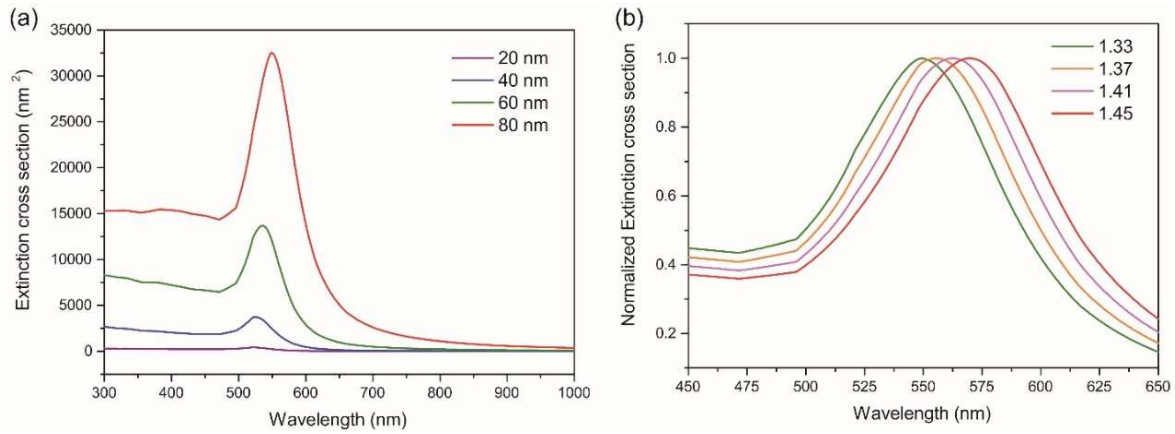

Figure 2.2 | Extinction cross-section of the gold nanoparticle. (a) With increasing particle size, the plasmon resonance peak shifts to longer wavelengths and the magnitude of the cross-sections increases. (b) With an increasing refractive index of the surrounding medium, the plasmon resonance of an 80 nm gold nanoparticle shows a red shift.

2.1.2 Thermal Properties of Gold Nanoparticles

As discussed above, gold nanoparticles present strong scattering and absorption of light at a specific wavelength in the visible and near-infrared region due to their localized plasmon resonances. Due to the much larger absorption cross-section of a gold nanoparticle compared to its geometric cross-section, it can collect light from a much larger area. For a gold nanoparticle, the larger the particle size, the greater the absorption efficiency[81]. When a gold nanoparticle is irradiated by an electromagnetic wave, the

coherent oscillation of electrons results in the elastic scattering of the incident wave, while the incoherent oscillation of electrons leads to increasing temperature inside the gold nanoparticle. This process is reported to happen in the order of picoseconds, using femtosecond excitation lasers[82-84].

Plasmonic heating of gold nanoparticles

To explain and understand this internal process, we assume the simplest case: that a gold nanoparticle is in its ground state (T=0 K) before laser excitation, and all of the quantum states below the Fermi energy are occupied, while all of the states above the Fermi energy are unoccupied. When excited with a laser pulse that is shorter than the electron-phonon energy relaxation time, part of the electrons are excited above the Fermi energy. At this point, the electron distribution is in the non-thermal equilibrium state with regard to the Fermi-Dirac distribution[85]. These non-thermal electrons then relax (thermalize) by electron-electron scattering without losing the absorbed photon energy. This process happens within one picosecond[86, 87]. This electron-electron interaction produces a hot-electron gas, and the temperature of an electron can reach several thousands of degrees Celsius. Within the next 1 to 10 picoseconds[88-90], the electron-phonon interaction leads to a temperature equilibration between the electron and the lattice subsystems, resulting in homogeneous heating of the gold nanoparticle. After reaching thermal equilibrium, the gold nanoparticle transfers the heat to the surrounding medium. As the excited electrons above the Fermi level lose their energy to the phonons, leading to the cooling of the electron gas, the Fermi-Dirac distribution narrows and the whole system returns to its ground state before laser excitation within one nanosecond, depending on the size of the gold nanoparticle[91]. This internal process is also applied for continuous wave excitation, and the surface temperature of a gold nanoparticle will be constant in the thermal equilibrium state.

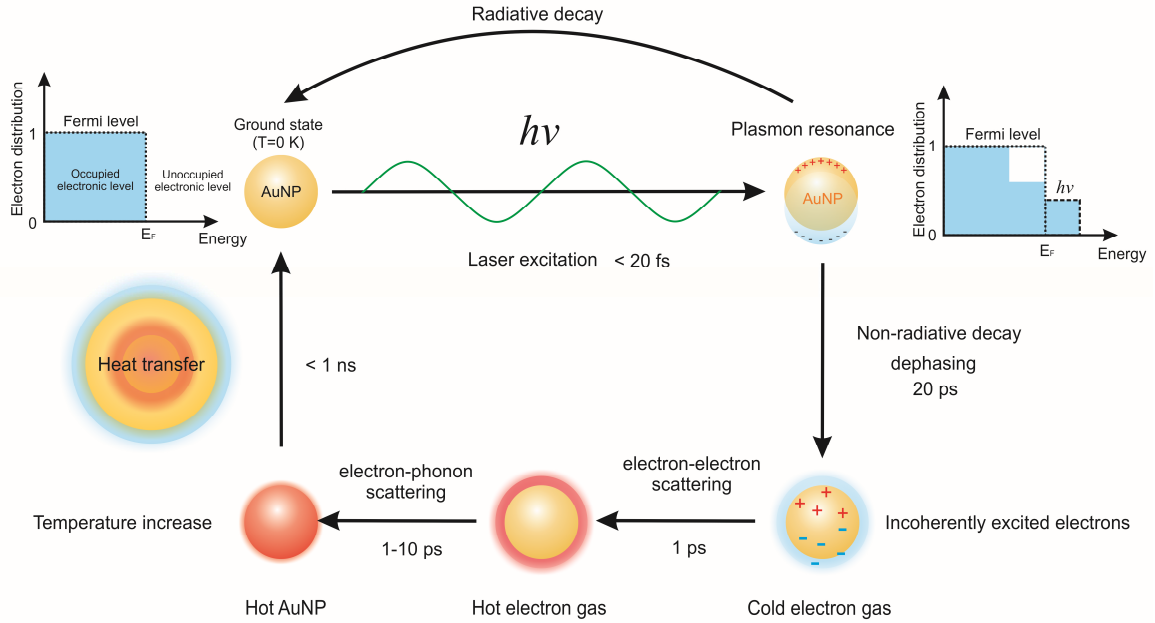

Figure 2.3 | Plasmonic heating processes of a gold nanoparticle upon laser excitation.

Heat distribution and bubble generation around cw laser heated gold nanoparticles

As described in the previous section, a gold nanoparticle can absorb photon energy and generate heat inside of itself efficiently. The generated heat will diffuse rapidly and heat the surrounding medium. Depending on the temperature increase, the gold nanoparticle and surrounding medium experience various thermophysical responses, as shown in **Figure 2.4**. In this thesis, we are particularly interested in the formation of bubbles around the gold nanoparticle under continuous wave (cw) resonance laser illumination.

Many studies during the past decade have reported photothermal bubble generation induced around plasmonic nanoparticles, mainly under pulsed laser excitation[17, 20, 92]. This effect has applications in photothermal therapy[93, 94], cell membrane optoporation[95, 96], drug/gene delivery[97], and photoacoustic imaging[98]. However, studies on photothermal bubble generation under cw illumination are recent, and their applications are less investigated. In 2011, Hühn et al.[99] were the first to hypothesize that superheating causes the generation of bubbles around nanoparticles under cw laser heating. Afterward, a

series of studies reported by Baffou et al.[42] and Halas et al.[100] illustrated in detail the achievements and mechanism of generating bubbles on nanoparticle arrays or a single gold nanoparticle. Following is a brief summary of the physics behind bubble generation around the gold nanoparticle under cw plasmonic heating.

When irradiated by a cw laser beam, a gold nanoparticle is heated because of the non-radiative decay. The heat from the nanoparticle is transferred into the surrounding liquid, resulting in a steady-state thermal gradient. Depending on the input laser power, the liquid can be heated above its boiling point without a liquid-gas interface appearing. This metastable state is known as superheating, which can be explained by the existence of the surface tension of the liquid. When a bubble forms, its inner pressure (P_B) reads as follows[101]

$$P_B = P_0 + \frac{2\gamma}{R_B} \tag{2.11},$$

where γ is the surface tension of the liquid, P_0 is the ambient pressure, and R_B is the radius of the bubble. To generate a bubble, the liquid temperature must be raised slightly above its boiling point to create enough vapor pressure to overcome the surface tension and ambient pressure. Another effect that prevents the formation of bubbles is the energy barrier at the liquid-gas interface[101]:

$$\Delta E = 4\pi {R_B}^2 \gamma \tag{2.12}.$$

Bubble formation occurs only when this energy barrier is overcome. The main reason that the water superheating is not usually observed is that most surfaces of the containers are endowed with small impurities, scratches, or cavities, which are potential nucleation centers. The presence of these nucleation centers during heating lowers the energy barrier[99]. However, if a gold nanoparticle is deposited on a particularly clean and flat glass substrate in water, most of the nucleation centers for bubble growth are avoided, which leads to superheating of the surrounding liquid. Without heterogeneities, the nucleation of vapor bubbles must occur from a vapor embryo that exceeds a critical radius to grow spontaneously. As the temperature increases, the free energy barrier decreases until the

temperature reaches the spinodal decomposition temperature (SDT) of water. At this temperature, a phase transition occurs without the presence of nucleation[43] centers (i.e., the homogeneous bubble nucleation grows over time). Another critical reason that water superheats around a nanoparticle is that the space, size, and amount of surrounding liquids that are heated are restricted by the nanoscaled size of the gold nanoparticle. In other words, the gold nanoparticle only heats a small volume of water, which limits the possible cavities of the dissolved gas or other heterogeneities in liquid that facilitate bubble nucleation. This temperature confinement, together with the other considerations discussed above, traps the water in a metastable state above the normal boiling point until the SDT reaches a point where the bubbles begin to grow.

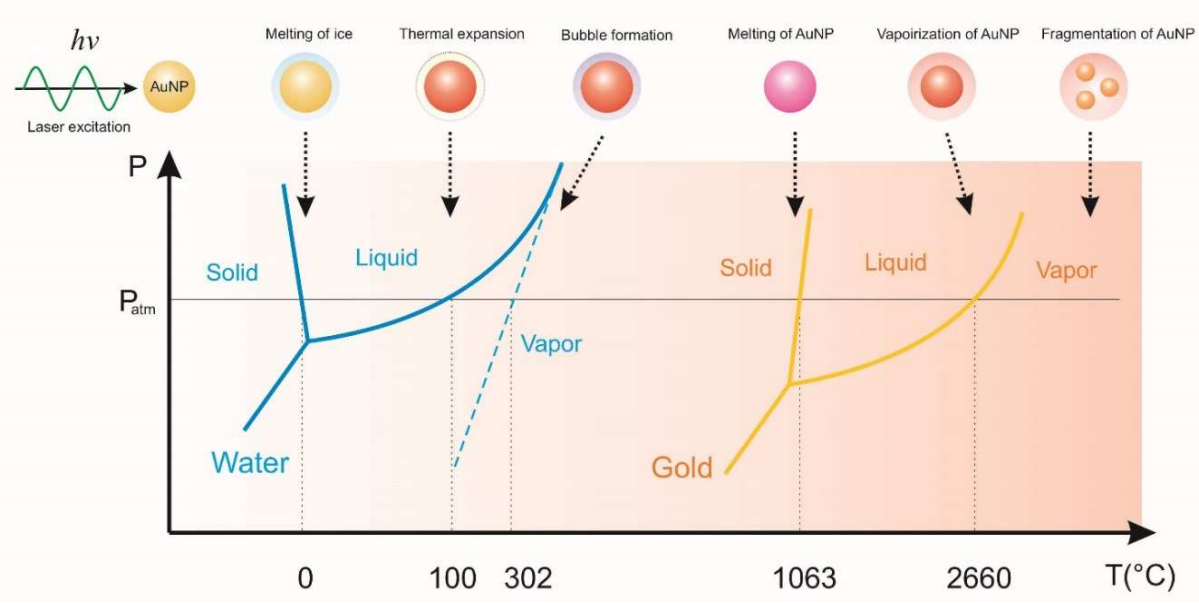

Figure 2.4 | Schematic illustration of thermophysical responses of a laser heated gold nanoparticle and its surrounding medium. As the laser power increases, the gold nanoparticle surface temperature increases, which results in different thermophysical responses. The phase diagram shows the thermodynamic equilibrium states with the solid lines and the spinodal curve of water (non-equilibrium) in the dashed line (Adapted from Qin *et al.*[102]).

To quantitatively calculate the amount of heat that is generated on a gold nanoparticle, the heat transfer equation is used to describe the transferring of the heat[12]:

$$\rho(\boldsymbol{r})C_p(\boldsymbol{r})\frac{\partial T(\boldsymbol{r},t)}{\partial t} - \nabla k(\boldsymbol{r})\nabla T(\boldsymbol{r},t) = Q \quad (2.13),$$

where $\rho(\vec{r})$ is the mass density of gold, $C_p(\vec{r})$ is the heat capacity of gold at constant pressure, $k(\vec{r})$ is the thermal conductivity of gold, $\vec{r}$ and t are the spatial coordinate and time, respectively. Q is the local heat density per gold volume.

When irradiated with a continuous wave laser beam, the generated and dissipated thermal energies of the gold nanoparticle are constant, and the thermal steady-state is reached at the time when the temperature distribution inside of the system is constant. The steady-state temperature increase around a gold nanoparticle can be expressed as follows[12]:

$$\Delta T(\boldsymbol{r}) = \frac{QV}{4\pi k_m \boldsymbol{r}} \quad (2.14),$$

where Q is the thermal energy of the heat source, V is the gold nanoparticle volume, k_m is the heat conductivity, and $\boldsymbol{r}$ is the distance to the heat source.

Figure 2.5 shows the temperature distribution around gold nanoparticles with different sizes in water that are illuminated by the same laser beam, or one gold nanoparticle that is irradiated with different laser powers. The detailed method for calculation and simulation is described in the **Appendix**. This figure demonstrates that the maximum temperature is at the surface of the gold nanoparticle and is linearly proportional to the incident laser power. The temperature at the gold nanoparticle surface can reach several hundred degrees rapidly with a small amount of laser power. This property makes gold nanoparticles ideal candidates for a nano heat source, and they have been widely used in nanomedicine[13].

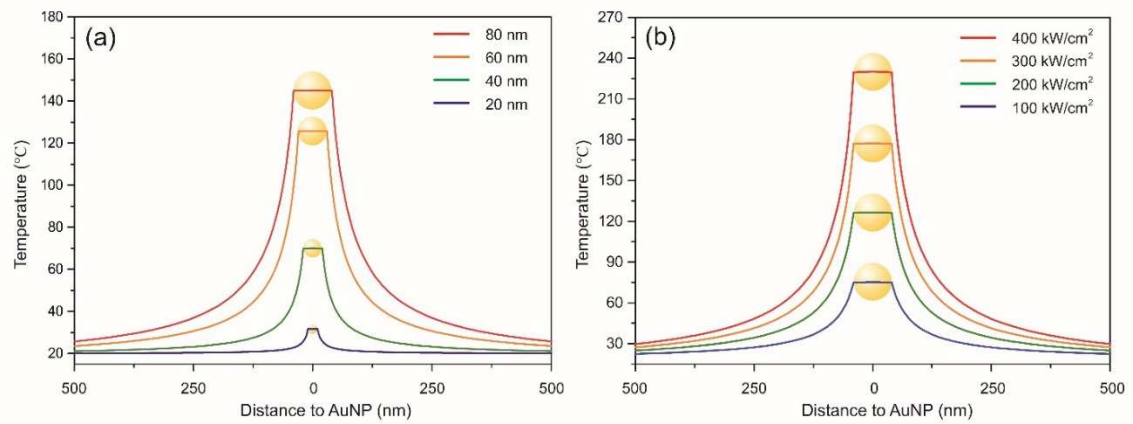

Figure 2.5 | Temperature distributions around the plasmonically heated gold nanoparticle in water. (a) Gold nanoparticles with different sizes in water are irradiated with a CW laser beam at a power density of 237 kW/cm^2. The temperature decreases as an order of 1/r to the center of the gold nanoparticle. (b) Heat distribution of a gold nanoparticle with a diameter of 80 nm heated with a laser beam at 100, 200, and 300 kW/cm^2.

2.1.3 Optical Forces

As described above, the incident light is absorbed and transformed into heat by the irradiated gold nanoparticle, and it exerts pressures due to scattering. The wavelength of light and particle size play important roles during light-particle interaction. Based on this, models of light scattering, as shown in **Figure 2.6**, can be divided into three regimes. The first is the Rayleigh scattering regime, when the size of a nanosphere (r) is much smaller than the wavelength (λ) of the laser beam ($r \ll \lambda$). In this regime, a nanosphere can be approximated as a dipole and the optical forces can be calculated by the Rayleigh scattering theory[103]. The second regime is the ray optics regime. This regime is characterized by the size of the particle, which is much larger than the wavelength of the laser beam ($r \gg \lambda$). Optical forces, in this case, can be calculated by a ray optics approximation[104]. A qualitative view of the forces that were analyzed is shown in **Figure 2.6**. As a laser irradiates the particle, the photons are reflected when they hit the particle, and they change their momentum, resulting in a force that acts on the particle and points in the direction of light propagation. This force is known as the scattering force. Meanwhile, the laser beam will also be refracted as it passes through the particle due to the difference in refractive indices between the particle and the surrounding medium. As

a result, the beam changes its direction as it exits the particle, which again leads to a change in momentum and results in a force that pushes the particle towards the center of the laser beam where the laser intensity is the highest. This force is called the gradient force. In this thesis, the sizes of gold nanoparticles are comparable to the wavelength of the laser beam ($r \approx \lambda$), which is also known as the Mie regime. In this case, ray optics and the Rayleigh scattering theory cannot be applied. Instead, the electromagnetic theory of light must be used. Although one can use the generalized Lorenz-Mie theory to calculate the optical forces, the mathematical process is complex[105]. Here, the method is simplified particularly toward the gold nanoparticle (80 nm) that is used in this thesis, using modified dipole approximation to calculate the optical force, which is derived from the nonrelativistic Lorentz force[106].

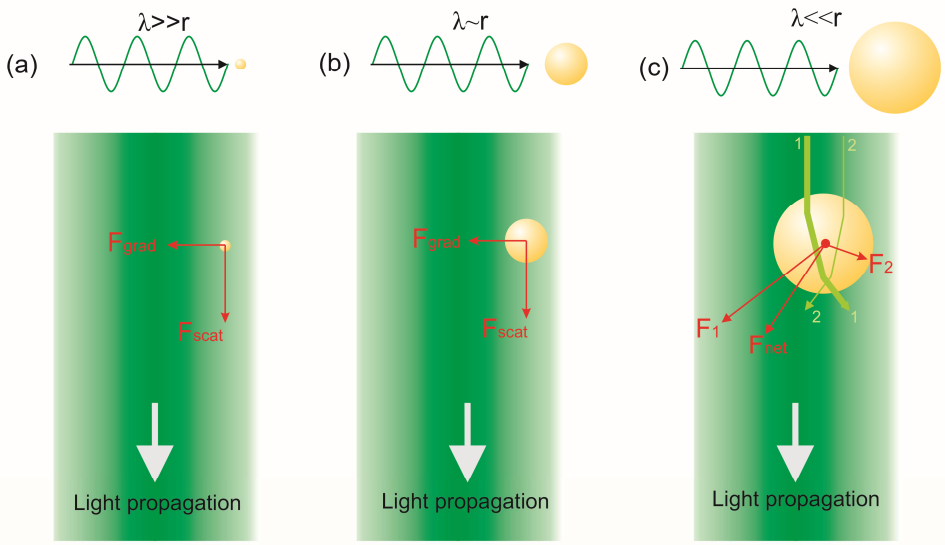

Figure 2.6 | The three optical regimes of the optical forces on a particle. (a) Rayleigh regime with a small particle in the laser beam. (b) Mie regime with particle size in the order of the wavelength of a laser beam. (c) The ray optics regime with a particle size that is larger than the wavelength of a laser beam.

The gold nanoparticle is considered as a dipole. Thus, the Lorentz force acting on this particle with charge q and speed v in an electromagnetic field is expressed as:

$$\mathbf{F}_{Lorentz} = q[\mathbf{E}(\mathbf{r},t) + v(\mathbf{r},t) \times \mu_0 \mathbf{B}(\mathbf{r},t)] \qquad (2.15).$$

$\mathbf{E}(\mathbf{r},t)$ and $\mathbf{B}(\mathbf{r},t)$ represent the position-dependent and time-dependent electric field and magnetic field, respectively. In the case of a dipole with a dipole moment $\mathbf{p} = \varepsilon_0\varepsilon_m\alpha\mathbf{E}$, equation (2.15) can be written in the form of Lorentz force density[106]:

$$\mathbf{F}_{Lorentz}^{density} = (\varepsilon_0\varepsilon_m\alpha\mathbf{E}\nabla)\mathbf{E}(\mathbf{r},t) + \varepsilon_0\varepsilon_m\alpha\frac{\partial\mathbf{E}}{\partial t}\times\mathbf{B}(\mathbf{r},t) \qquad (2.16).$$

By applying the vector calculus identity $(\mathbf{E}\nabla)\mathbf{E} = \nabla(\mathbf{E}^2/2) - \mathbf{E}\times(\nabla\times\mathbf{E})$ and Maxwell equation $\nabla\times\mathbf{E} = -\partial\mathbf{B}/\partial t$, equation (2.16) is rewritten as:

$$\mathbf{F} = \varepsilon_0\varepsilon_m\alpha\frac{\nabla\mathbf{E}(\mathbf{r},t)^2}{2} + \varepsilon_0\varepsilon_m\alpha\frac{\partial}{\partial t}(\mathbf{E},\mathbf{B}) \qquad (2.17)$$

Averaging the equation (2.17) over the period $2\pi/\omega$, and inserting the real part α' and the imaginary part α'' of polarizability from equation (2.3) results in the expression of total optical forces[22]:

$$\mathbf{F}_{\boldsymbol{Total}} = \frac{1}{4}\varepsilon_0\varepsilon_m\alpha'\nabla(\mathbf{E}^*\mathbf{E}) + \frac{1}{2}\varepsilon_0\varepsilon_m\alpha''Im\left\{\sum_{i=x,y,z}\mathbf{E}_i^*\nabla\mathbf{E}\right\} \qquad (2.18)$$

where * represents the complex conjugate and Im represents the imaginary part. This equation can be decomposed into two parts, representing the gradient force and the scattering force:

$$\mathbf{F}_{grad} = \frac{1}{4}\varepsilon_0\varepsilon_m\alpha'\nabla(\mathbf{E}^*\mathbf{E}) \qquad (2.19)$$

$$\mathbf{F}_{scat} = \frac{1}{2}\varepsilon_0\varepsilon_m\alpha''Im\left\{\sum_{i=x,y,z}\mathbf{E}_i^*\nabla\mathbf{E}\right\} \qquad (2.20)$$

As equation (2.19) and equation (2.20) demonstrate, the magnitude of the gradient force and the scattering force highly depends on the real part and imaginary part of

polarizability, respectively. This enables the manipulation of the nanoparticles optically, such as printing particles or trapping particles, by tuning the ratio of the real and imaginary parts of polarizability. **Figure 2.7** shows an example of the complex polarizability of an 80 nm gold nanoparticle as a function of the wavelength of the manipulating laser beam. In the wavelength regions that are close to plasmon resonance of the particle, α'' is much larger than α', which leads to a strong scattering force and a weak gradient force. The net result is the total force pushing the particle toward the direction of laser propagation, which is also the principle of laser printing of gold nanoparticles. In the near-infrared wavelength region, the dominance of α', which corresponds to the strong gradient force, makes it possible to trap the particle in three-dimensions using a strongly focused laser beam.

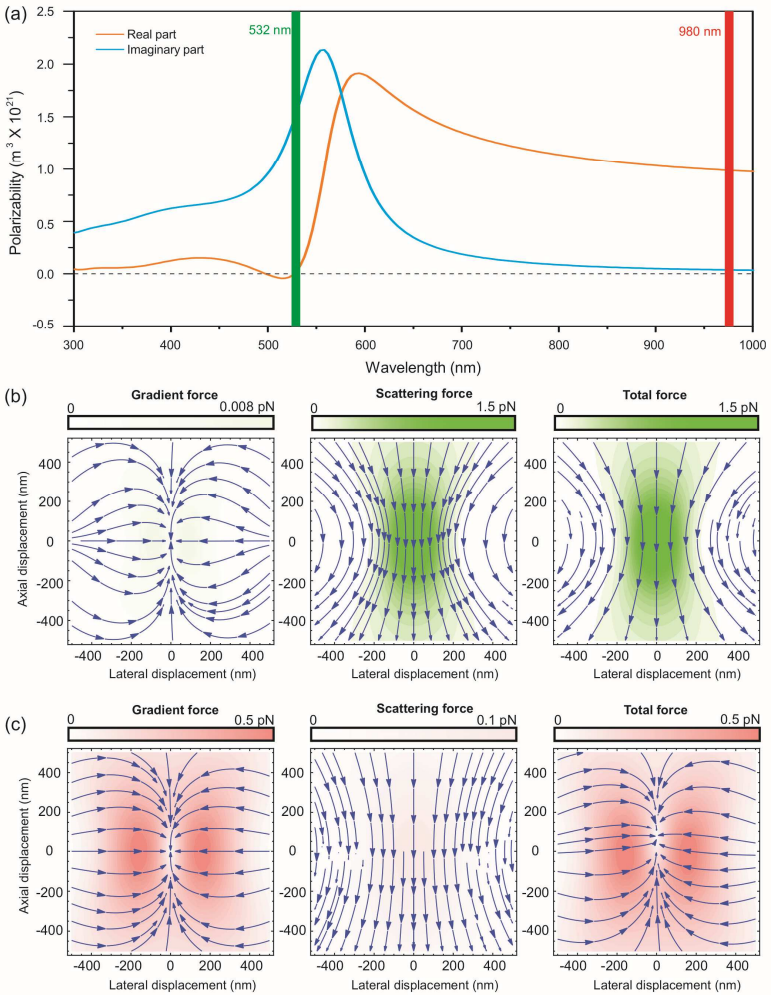

Figure 2.7 | Controlling optical forces by tuning the wavelength of laser beams. (a) Complex polarizability of a gold nanoparticle with a diameter of 80 nm in a medium with refractive index n = 1.33. (b) The mapping of optical forces applied to a gold nanoparticle upon irradiation with a 532 nm laser beam at a laser output power of 1 mW. (c) Optical force map applied on a gold nanoparticle upon irradiation with a 980 nm laser beam at laser output power of 20 mW.

2.2 Interactions between Gold Nanoparticles and Living Cells

The previous sections introduced the fundamentals of light-AuNP interactions. This is important as in recent years, the optical and thermal properties of gold nanoparticles have been utilized for many biological applications[107, 108]. Physicists and biologists can optically manipulate AuNPs on biological membranes and inside of cells[109-111]. This is of great significance because the cell membrane is the first barrier that separates the interior of the whole cell from the outside environment, and one can control the cell functions in a more precise way by optically altering the membrane properties[112] for biomedical reasons, including drug/gene delivery or intracellular sensing. In this thesis, the plasmonic properties of gold nanoparticles were used to develop a new route of cellular delivery and achieve intracellular biosensing applications. To understand this, the fundamentals of biological membranes and the current strategies for cellular delivery must be understood.

2.2.1 Cellular Membranes and Permeability

The cell membrane, also known as the plasma membrane or cytoplasmic membrane, is a thin (5 to 10 nm wide), impenetrable biological barrier that protects the cell's delicate internal contents from a nonliving and often inhospitable environment by separating the cells from the external world. Membranes consist of lipid–protein assemblies where the components are held together in a thin sheet by noncovalent bonds. As illustrated in **Figure 2.8**, the core of the membrane consists of a lipid bilayer that serves primarily as a structural backbone of the membrane and provides a barrier that prevents the diffusion of water-soluble materials into and out of the cell. The proteins of the membrane implement most of the specific functions.

The plasma membrane has a dual function. On one hand, it retains the substances inside of the cell to ensure that they do not leak into the environment. On the other hand, it allows for the necessary exchange of information in and out of the cell. The plasma membrane plays a critical role in a variety of cellular processes[113], such as signal transduction, intercellular interaction, energy conversion, and cell-matter interactions.

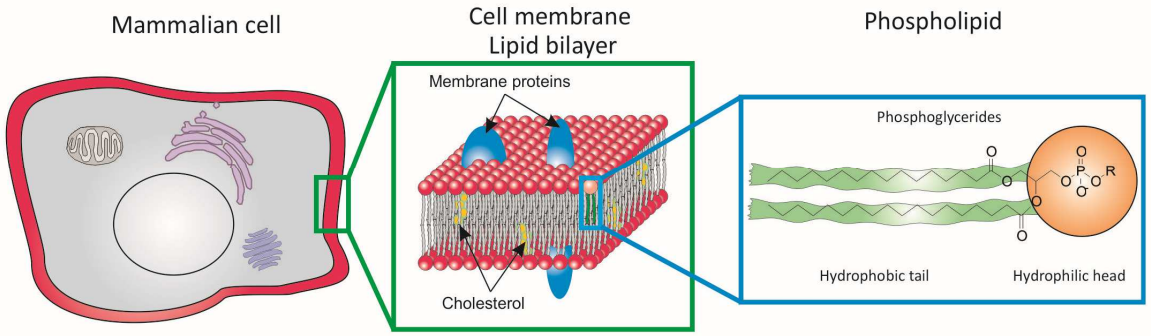

Figure 2.8 | Illustration of the basic structure of a eukaryotic cell membrane. The cell membrane consists of the lipid bilayer, which is an assembly of lipid molecules. Phospholipids with hydrophobic tails and hydrophilic heads are the main components of the lipid bilayer. Membrane proteins and cholesterols are implanted within the bilayer.

Small solute molecules move through the membrane via two methods: passive diffusion or active energy-dependent transport, a diagram of which is shown in **Figure 2.9**. Water molecules, oxygen, carbon dioxide, and certain small nonpolar molecules can freely diffuse through the plasma membrane, driven by the concentration gradient. Other small molecules such as ions and amino acids cross the membrane through the active transport pathway of integral membrane protein pumps or ion channels[114].

However, most therapeutic drugs and inorganic nanoparticles are hydrophobic and impermeable to the cell membrane. Therefore, they are usually formulated or functionalized as nanoscale hydrophilic biomacromolecules and are conventionally transported into the cell by means of endocytosis, which is a pathway that internalizes cargo in transport vesicles that are derived from the plasma membrane. The following discussion focuses on this type of internalization and specifically on how gold nanoparticles penetrate the cell membrane[115].

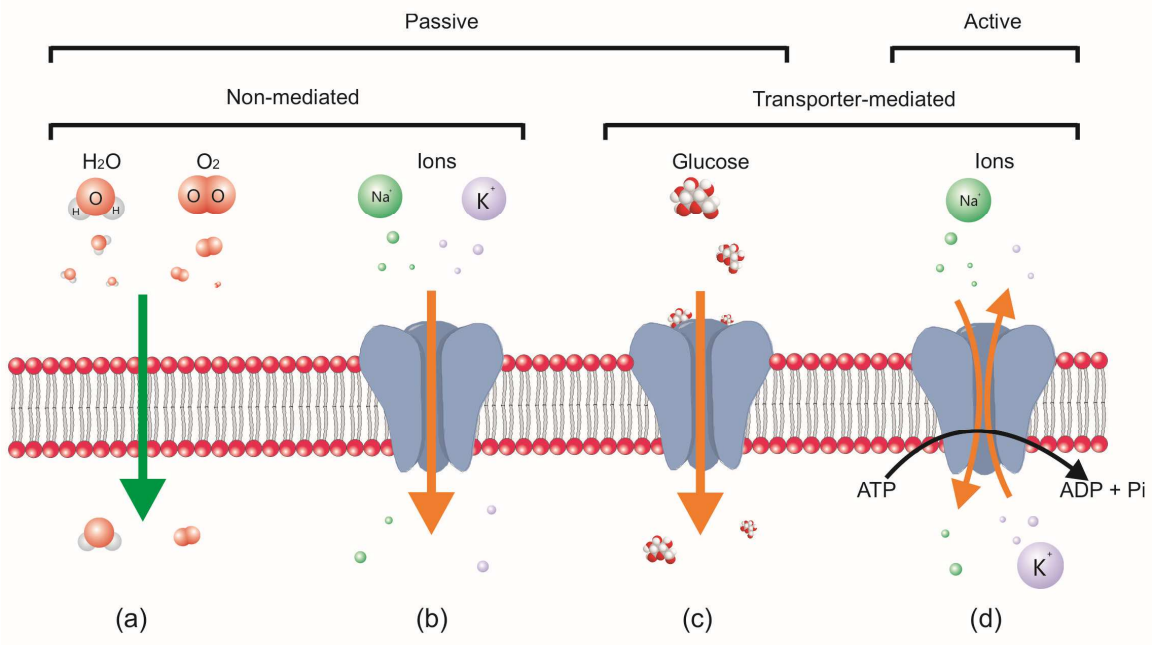

Figure 2.9 | Four basic mechanisms of solute molecules moving across membranes. The arrows indicate the direction of substance movement. (a) Simple diffusion through the bilayer, which always proceeds from high to low concentration. (b) Simple diffusion through a membrane channel formed with the integral proteins. (c) Facilitated diffusion in which solute molecules bind specifically to a membrane protein transporter. (d) Energy-dependent active transport using a protein transporter. Movement occurs against a concentration gradient.

2.2.2 Cellular Uptake of Nanoscale Matters

Endocytosis is a cellular active transport process in which a cell takes up exogenous materials in an energy-dependent manner by enclosing them in vesicles that are pinched off from their cytoplasmic membrane. Currently, the endocytotic process is categorized into three types: phagocytosis, pinocytosis, and receptor-mediated endocytosis (RME). Phagocytosis, which is also called 'cell eating,' is a process where a cell internalizes large particles with diameters that are greater than 750 nm (such as dust particles, cell debris, microorganisms, bacteria, and apoptotic cells) by folding around the molecules or substances with the plasma membrane to form an internal phagosome[116]. This process is conducted by specialized mammalian cells, such as monocytes, macrophages, and neutrophils[115]. Pinocytosis, which is also known as 'cell drinking,' is a process in which

extracellular particles are brought into the cell, forming an invagination, and are then suspended within small vesicles. This process occurs in most cell types, and small particles that range from a few to several hundred nanometres are internalized by pinocytosis or micropinocytosis. Receptor-mediated endocytosis, which is also called clathrin-dependent endocytosis, is similar to pinocytosis except that the cell uses receptor proteins embedded within the cell membrane to recognize the materials to internalize. Once a ligand binds to a plasma membrane receptor, a signal is sent through the membrane; this leads to the coating of the membrane from the interior of the cell by a type of protein called clathrin, which assists in the formation of a membrane invagination. The cargos are deposited in small endocytic vesicles (usual diameters are smaller than 100 nm) that fuse with early endosomes[117]. This process is the primary characterized mechanism for the cellular uptake of nanoparticles. A diagram of the endocytotic pathway is shown in **Figure 2.10**.

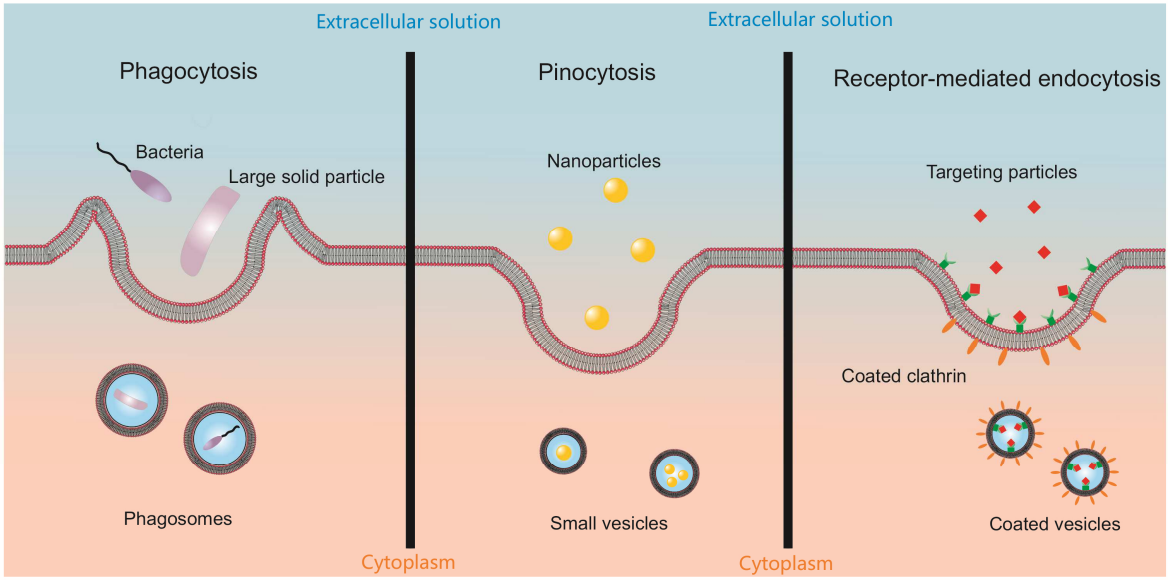

Figure 2.10 | Schematic of the known pathways for the intracellular uptake of nanoparticles.

For the cellular uptake of gold nanoparticles, the pathway for cellular internalization varies depending on the size, shape, and surface properties of each particle. Typically, the incubation of gold nanoparticles with cell culture medium leads to the formation of an

AuNP-protein corona on the gold nanoparticle surface. The corona is a complex mixture of proteins that is absorbed on the surface of gold nanoparticles and plays a significant role in tuning the surface physicochemical properties of gold nanoparticles. The RME is the most possible internalization pathway of gold nanoparticles in this case[118]. However, if the surface of the gold nanoparticle is covered by organic molecules, the cellular uptake pathway is mostly changed. It is reported that positively charged gold nanoparticles were taken up mainly by the macropinocytosis pathway, while negatively charged gold nanoparticles entered the cell mainly by clathrin-dependent endocytosis[119, 120]. Recently, a more comprehensive study reported the effect of gold nanoparticle surface charge on their cellular uptake[121]. The study found that positively charged gold nanoparticles are favored by the cell membrane over negatively charged or hydrophobic particles. The uptake is promoted by increasing the surface charge density of the gold nanoparticles. Exceeding a certain threshold of charge density, the gold nanoparticles can escape an endocytotic pathway and directly diffuse into the cell.

However, these results were obtained by computer simulations, and the situation, in reality, would be more complicated. As mentioned above, many factors affect the cellular uptake of gold nanoparticles, and more complex situations of cellular uptake regarding the size, shape, and surface modifications of gold nanoparticles are discussed in recent publications[115, 122]. A successful cell delivery of gold nanoparticles requires the precise delivery of the particles to a target site. This indicates that the internalization pathway should be clear and definable, and the whole process is ideally controllable. To accomplish this, chemists and biologist have developed many ways to modify the surface of gold nanoparticles with functional groups, including polymers, nucleic acids, and proteins, to improve the targeting and membrane permeability[123, 124]. These engineered gold nanoparticles showed improved and more specific cellular internalization. These methods normally require multi-step chemical synthesis, and experiments are conducted on an entire sample of the cell. In this thesis, a novel method is introduced to deliver a single gold nanoparticle into a single cell using a completely optical method. This approach will provide a new concept for the development of modern nanoparticle cellular delivery strategies and pave the way for many possible future applications.

2.3 Motion of Particles in Living Cells

The previous sections discuss how nanoparticles interact with cells and how they are delivered into the cytoplasm. Once the particles are inside of the cells, analyzing the motions of these nano-sized objects can provide an evaluation of the local and non-bulk properties of the heterogeneous intracellular environment[125]. The behavior of particles inside living cells is complex. Thus, this section begins with the introduction of the most common and simplest movement of small particles, the Brownian motion, focusing on the mathematical description of this motion, the Langevin equation. Based on the equation, more complicated cases of analyzing the inside of living cells can be achieved by modifying each term of the equation with appropriate models.

2.3.1 Langevin Equation

Brownian motion refers to the random motion of particles that are suspended in fluid. This motion is a result of their collisions with the atoms or molecules in the fluid. The time evolution of the position of a particle in Brownian motion can be described by the Langevin equation; this equation involves a random force that represents the effect of the thermal fluctuations of the solvent on the particle. Considering a case of a small particle immersed in a fluid, this particle is not acted upon by any external forces other than the force that results from the collisions with molecules in the fluid. According to Newton's second law of motion

$$m\ddot{x} = F, \tag{2.21}$$

where m is the mass of the particle and x is the displacement of the particle within time t (thus, $\ddot{x} = d^2x \,/\, dt$), and *F* is the total force that is applied to the particle, which can be split up into two different forces. The first force is called the frictional force (drag force):

$$F_{drag} = -\gamma\dot{x}, \tag{2.22}$$

which represents the dynamical friction that is experienced by the particle and is proportional to and acts on the opposite direction of the particle's velocity $\dot{x} = dx/dt$. Here, γ is the friction coefficient and it is related to the viscosity of the fluid. The second part of the total force is regarded as random thermal force $F_{thermal}(t)$, which is a fluctuating force that is due to the collision of fluid molecules on the particle. This force is stochastic and is independent of the particle's displacement. It fulfils:

$$\langle F_{thermal}(t) \rangle = 0, \tag{2.23}$$

$$\langle F_{thermal}(t) F_{thermal}(t') \rangle = \sqrt{2k_B T\gamma}\,\delta(t - t'). \tag{2.24}$$

Here, t and t' are different time steps and $\delta(t)$ denotes the Dirac delta function. The Fourier transform of equation (2.24) gives the power spectral density, which is discussed in later sections. The power spectral density is constant over all frequencies; in this case, it is regarded as white noise. We can write equation (2.21) as:

$$m\ddot{x} = -\gamma\dot{x} + F_{thermal}(t). \tag{2.25}$$

Equation (2.25) is known as the Langevin equation for Brownian particles. In the case of an external force $(F_{ext.})$ acting on the particle, equation (2.25) can be written as:

$$m\ddot{x} = -\gamma\dot{x} + F_{thermal}(t) + F_{ext.}\,. \tag{2.26}$$

Equation (2.26) is used in this thesis to describe the motion of gold nanoparticles inside of living cells applied to a time-dependent driving force. The detailed solutions are discussed in subsequent chapters.

2.3.2 Single Particle Tracking and Mean Square Displacement

The previous section introduced a mathematical approach to describing the motion of a Brownian particle. In the practical cases, one must extract the information of a particle's motion in order to apply and solve the motion equations. Thus, a measurement technique that can precisely give the time-position data is required. Single particle tracking (SPT) has been widely used as a powerful tool to study the complex and highly dynamic organization of the heterogeneous systems[126-128]. As illustrated in **Figure 2.11**, SPT is based on observation of an individual particle's motion within a medium, and coordinates (x, y) are recorded over a series of time steps, yielding the trajectory for the tracked particle. The trajectory represents the positions of the particle and can be further analyzed to identify modes of motion. As this technique provides the time-displacement information of a single particle at the micro-scale or nano-scale, it enables the possibility of detecting the microscale behavior of a dynamic system, which cannot be directly accessed by other optical microscopy types.

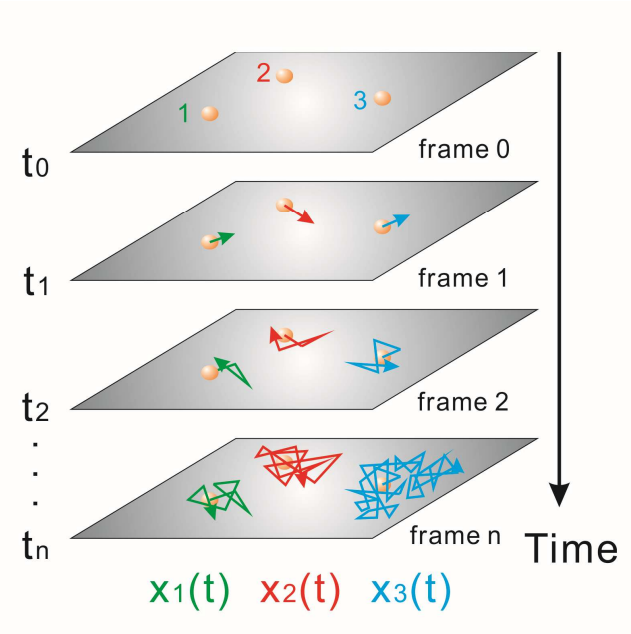

Figure 2.11 | Principle of single particle tracking. The positions of each tracked particle are recorded at each time steps $t_0, t_1, t_2, \ldots, t_n$. In the last frame, the trajectories are represented as time-displacement x(t).

To understand the dynamics of particle motion, several theoretical interpretations are introduced. Usually the physics of particle motion is described by time averaged mean

square displacement (MSD), which is defined as the square of the displacement of a particle at a certain time, relative to the position of the particle at zero time, averaged over many time points[129], and has the following expression:

$$MSD(\Delta t) = \langle \boldsymbol{r}^2(\Delta t) \rangle = \frac{1}{n - \Delta t} \sum_{i=0}^{n-\Delta t-1} |\boldsymbol{r}(t_{i+\Delta t}) - \boldsymbol{r}(t_i)|^2 \qquad (2.27),$$

where $\boldsymbol{r}(t_i)$ is the position of a particle at a certain time step t_i; n is the total recorded time of steps, $\Delta t = 1, 2, 3, \ldots, \mathrm{n} - 1$ is the time delay, which is interpreted in **Figure 2.12**. This method of calculating MSD averages over all pairs of trajectory points for a time delay, Δt.

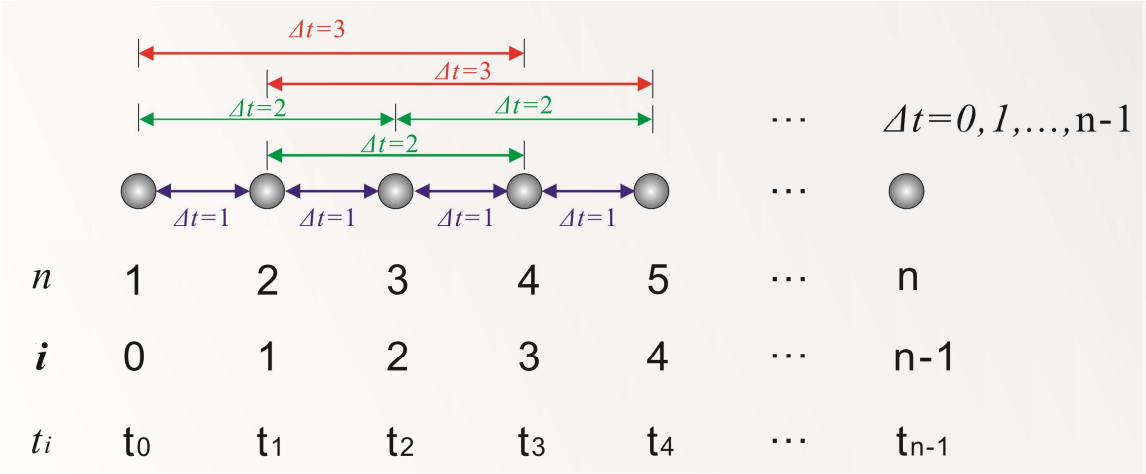

Figure 2.12 | Schematic illustration of the calculation of mean square displacement (MSD).

If a particle diffuses in a viscous liquid at thermal equilibrium when the motion of driving force is only exerted by the molecules in the surrounding medium, this particle exhibits random, diffusive motion[130]. The motion in d-dimensional systems is normally described as a linear time dependence of the MSD:

$$MSD(\Delta t) = 2dD\Delta t \qquad (2.28),$$

where D is the diffusion coefficient that is involved in the Stokes-Einstein equation[131]:

$$k_B T = 6\pi\eta a D \quad (2.29),$$

where $k_B T$ is the thermal energy of the liquid with k_B Boltzmann's constant and T is the absolute temperature. Equation (2.28) is valid for thermal equilibrium liquid and particle motion and depends on the viscosity of liquid (η) and the particle's radius (a). However, the microenvironment inside of a cell is more complicated than a viscous liquid because it is a collection of macromolecules and compartments of different sizes with specific functionalities that are located in the viscous liquid containing ions and small molecule complexes. This heterogeneous combination makes cytoplasm a viscoelastic structure. The cytoskeleton contributes the most to this crowded environment, not only forming the networks that spatially organize the whole cell but also providing a toehold for molecular motors that carry particles actively in specific directions[132]. Therefore, one must take into account the influence of the intracellular environment when dealing with the motion of a particle inside of a cell.

According to Michael J. Saxton's research[133], the diffusion of a particle through a viscoelastic medium is defined as anomalous diffusion, the MSD of which becomes nonlinear with time and can be described with a time-dependent power law:

$$MSD(\Delta t) = 2dD\Delta t^{\alpha} \quad (2.30).$$

Here, α is also referred to as the diffusive exponent, the value of which indicates the mode of motion that is induced by energy consuming force and thermally mediated force. **Figure 2.13** schematically shows the different types of particle motions that are characterized by the MSD exponent law. $\alpha = 0$ indicates that the particle is stuck and exhibits confined diffusion. When the diffusive exponent is in the range of $0 < \alpha < 1$, the motion is typically called anomalous subdiffusion, which indicates the hindrance to free diffusion. Particles inside of the cytoplasm that are confined by the cytoskeleton normally exhibit subdiffusion with an α value between 0.6 and 0.8[26]. $\alpha = 1$ represents normal diffusion. Although the MSD becomes linear with time in this case as well, the motion of a particle is not driven solely by the thermal force of the surrounding medium but also by

other random intracellular motion; biological activity can also give rise to random fluctuation motion that dominates the thermally induced fluctuations. Evidence of this conclusion was reported by M. Guo and D. A. Weitz who found that the normal diffusion behavior in the cytoplasm is caused by random forces because of aggregate motor activity in the cell, rather than the result of thermally induced Brownian forces[134, 135]. The random movement of molecular motors contributes to the random motion of particles inside of the cell and results in the active transport of particles, which is called super diffusion and has the diffusive exponent $1 < \alpha < 2$, where $\alpha = 2$ is the ballistic limit of pure convection.

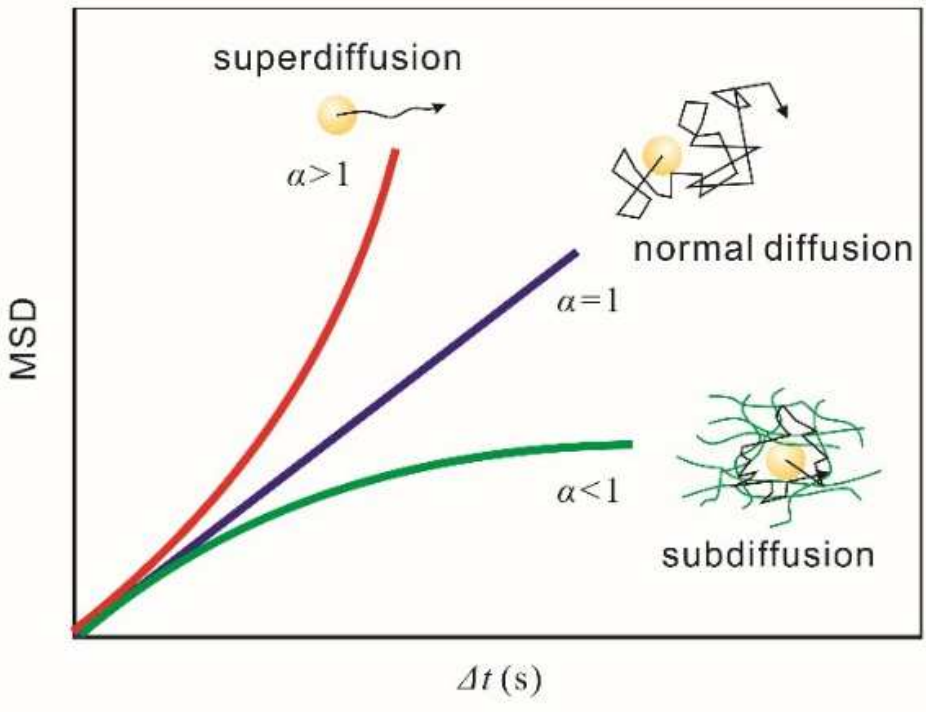

Figure 2.13 | Schematic showing of three types of particle motions characterized by MSD power law $MSD \sim \Delta t^{\alpha}$.

2.3.3 Fourier Transform and Power Spectral Density

Fourier analysis

Any physical signal that can be represented as an amplitude that varies in time, such as an electrical, optical, or mechanical signal, has a corresponding frequency spectrum. When these signals are viewed in the form of a frequency spectrum, certain aspects of the underlying or hidden information can be revealed, such as distinct peaks that correspond to certain wave components. Fourier analysis is a technique by which a signal variation in time is decomposed into its constituent temporal frequency components. This technique has found wide applications in various areas of everyday life[136]. A typical example is the function of the human ear, which works as an analogue Fourier analyzer: sounds in different frequencies are split into mechanical vibrations at different spatial locations along the cochlea. In this thesis, Fourier analysis is applied to analyze the motion of the intracellular gold nanoparticles. This section provides a brief introduction of the underlying principles of the Fourier transform.

A signal $x(t)$ with a total duration T can be decomposed into an infinite sum or series of sine and cosine functions:

$$x(t) = a_0 + \sum_{n=1}^{\infty} [a_n cos\left(\frac{2\pi nt}{T}\right) + b_n sin(\frac{2\pi nt}{T})] \quad (2.31).$$

The right side of equation is called the Fourier series. The coefficients a_0, a_n, and b_n, represent the amplitudes of each component and are calculated from the following time averages[137]

$$a_0 = \frac{1}{T} \int_{-T/2}^{T/2} x(t)dt \quad (2.32)$$

$$a_n = 2\left\langle x(t)cos\frac{2\pi nt}{T}\right\rangle = \frac{2}{T}\int_{-T/2}^{T/2} x(t)cos\frac{2\pi nt}{T}dt, \quad \text{interger n} \geq 1 \tag{2.33}$$

$$b_n = 2\left\langle x(t)sin\frac{2\pi nt}{T}\right\rangle = \frac{2}{T}\int_{-T/2}^{T/2} x(t)sin\frac{2\pi n\tau}{T}dt, \quad \text{interger n} \geq 1 \tag{2.34}.$$

Using Euler's formula and trigonometric identities, equation (2.31) can be simplified to a complex form of the Fourier series:

$$x(t) = \sum_{n=-\infty}^{+\infty} c_n e^{i\frac{2\pi nt}{T}} \tag{2.35},$$

where the coefficient is

$$c_n \stackrel{\text{def}}{=} \frac{1}{T}\int_{-T/2}^{T/2} x(t)e^{-i\frac{2\pi nt}{T}}d\tau \tag{2.36}.$$

Then inserting equation (2.36) into equation (2.35) provides

$$x(t) = \sum_{n=-\infty}^{\infty}\left[\frac{1}{T}\int_{-T/2}^{T/2} x(t)e^{-i\frac{2\pi nt}{T}}dt\right]e^{i\frac{2\pi nt}{T}} \tag{2.37}$$

where harmonics of frequency $f = n/T$, and these frequencies are separated by

$$\frac{(n+1)}{T} - \frac{n}{T} = \frac{1}{T} = f_0 \tag{2.38}$$

where f_0 denotes the fundamental frequency. It is suggested that in the long time limit ($T \to \infty$), f_0 becomes smaller ($f_0 \to 0$) and can be conveniently written as Δf. Then we can replace the sum over the discrete frequencies f by an integral over all frequencies and equation (2.37) can be written to

$$x(t) = \int_{-\infty}^{+\infty} \left[\int_{-\infty}^{+\infty} x(t) e^{-i2\pi f t} dt \right] e^{i2\pi f t} df. \tag{2.39}$$

Thus, we define Fourier transform (FT) as:

$$\hat{x}(f) \stackrel{\text{def}}{=} \int_{-\infty}^{+\infty} x(t) e^{-i2\pi f t} dt \tag{2.40}$$

and the inverse Fourier transform (FT) as:

$$x(t) \stackrel{\text{def}}{=} \int_{-\infty}^{+\infty} \hat{x}(f) e^{i2\pi f t} df \tag{2.41}.$$

The function $\hat{x}(f)$ is the equivalent of the Fourier coefficients in the Fourier series in equation (2.35). It is the function in the continuous frequency domain where $f \in (-\infty, +\infty)$.

However, in real life problems, the finite-time data is typically taken at integer times $t_j = t_0,\ t_1, \ldots, t_{N-1}$, and one must consider the Fourier transform in a discrete time domain. Given a case of N equal time samples, such as

$$t_j = j\Delta t \ (j = 0, 1, 2, \ldots, N-1), \tag{2.42}$$

where Δt is the time between two neighboring time steps, $f_s = 1/\Delta t$ is the sampling frequency, which is the number of samples taken per second. In this thesis, the sampling

frequency is the video camera's resolution (50 frames per second). If the signal $x(t)$ is periodic with period $T = N\Delta t$ measured at N discretely sampled times, then the corresponding frequencies are also discretized that is given by

$$f_k = k\Delta f \ (k = 0, 1, 2, \dots, N-1) \qquad (2.43),$$

where $\Delta f = 1/T = 1/N\Delta t = fs/N$ is the space between adjacent frequencies. Here the frequency f_k is limited in the region [$-f_s/2,\ f_s/2$], because $f_s/2$ is the Nyquist frequency: the maximum frequency of the original signal $x(t)$ that can be resolved. In other words, the sampling frequency should be at least twice the highest frequency contained in the signal[138]. Then the **discrete Fourier transform (DFT)** for a finite discrete time data set $X(t_j)$ is given by

$$\hat{X}(f_k) = \sum_{j=0}^{N-1} X(t_j) e^{-i2\pi f_k t_j}, \qquad k = 0, 1, 2, \dots, N-1 \qquad (2.44).$$

The DFT can be efficiently performed using the **fast Fourier transform (FFT)**, which is a particular computational algorithm for computing a DFT with more efficiency. Known from equation (2.44), there are *N* outputs $\hat{X}(f_k)$ and each output requires a sum of *N* terms. As a result, evaluating DFT directly requires $O(N^2)$ operations. FFT can compute the same results in only $O(N \log_2 N)$ operations[139]. This is a large increase in speed for large data sets. In this thesis, FFT is used to perform all of the Fourier analyses.

Power spectral density (PSD)

Power spectral density function (PSD) is a measure of a signal's power intensity as a function of frequency. We have shown that the random signals in the time domain can be analyzed in the frequency domain by Fourier transforming the signals. PSD shows the strength of the signals per unit frequency in the frequency domain. Assuming we have a truncated stochastic process $X_T(t)$ over a total period of time T:

$$X_T(t) = \begin{cases} x(t), & |t| \le T/2 \\ 0, & |t| > T/2 \end{cases} \quad (2.45).$$

The average power *(P)* over all time of this signal is

$$P = \lim_{T\to\infty} \frac{1}{T} \int_{-T/2}^{T/2} |x(t)|^2 dt \quad (2.46).$$

According to Parseval's theorem[140], the total energy of a signal can be expressed in terms of its Fourier transform:

$$\int_{-\infty}^{+\infty} |x(t)|^2 dt = \int_{-\infty}^{+\infty} |\hat{x}(f)|^2 df \quad (2.47).$$

Then equation (2.46) is written as

$$P = \lim_{T\to\infty} \frac{1}{T} \int_{-T/2}^{T/2} |x(t)|^2 dt = \lim_{T\to\infty} \frac{1}{T} \int_{-\infty}^{+\infty} |\hat{x}(f)|^2 df = \int_{-\infty}^{\infty} \lim_{T\to\infty} \frac{|\hat{x}(f)|^2}{T} df. \quad (2.48)$$

The power per unit frequency (i.e., the integrand on the right side of equation (2.48)) is defined as **power spectral density (PSD).**

$$S_x(f) \stackrel{\text{def}}{=} \lim_{T\to\infty} \frac{|\hat{x}(f)|^2}{T} = \lim_{T\to\infty} \frac{\hat{x}(f) \cdot \hat{x}^*(f)}{T}. \quad (2.49)$$

PSD is a description of the variation of a signal's power versus frequency. It is often conceived as single-sided, in which all of the power is accounted for in positive frequency space. If the signal corresponds to displacement, then the units of $S_x(f)$ is m^2/Hz.

Figure 2.14 shows an example of the power spectral analysis of a time-displacement signal $x(t)$. The signal has a duration of 60 seconds and is sampled at the rate of 50 Hz,

resulting in a time-displacement spectrum (**Figure 2.14**a). Discrete Fourier transform of the time trace is applied in the frequency region [5, 25 Hz] (**Figure 2.14**b) and the power spectral density analysis gives rise to two distinct peaks at 13.3 Hz and 22.0 Hz, respectively (**Figure 2.14**c), which reveals the hidden characteristics contained in the signal.

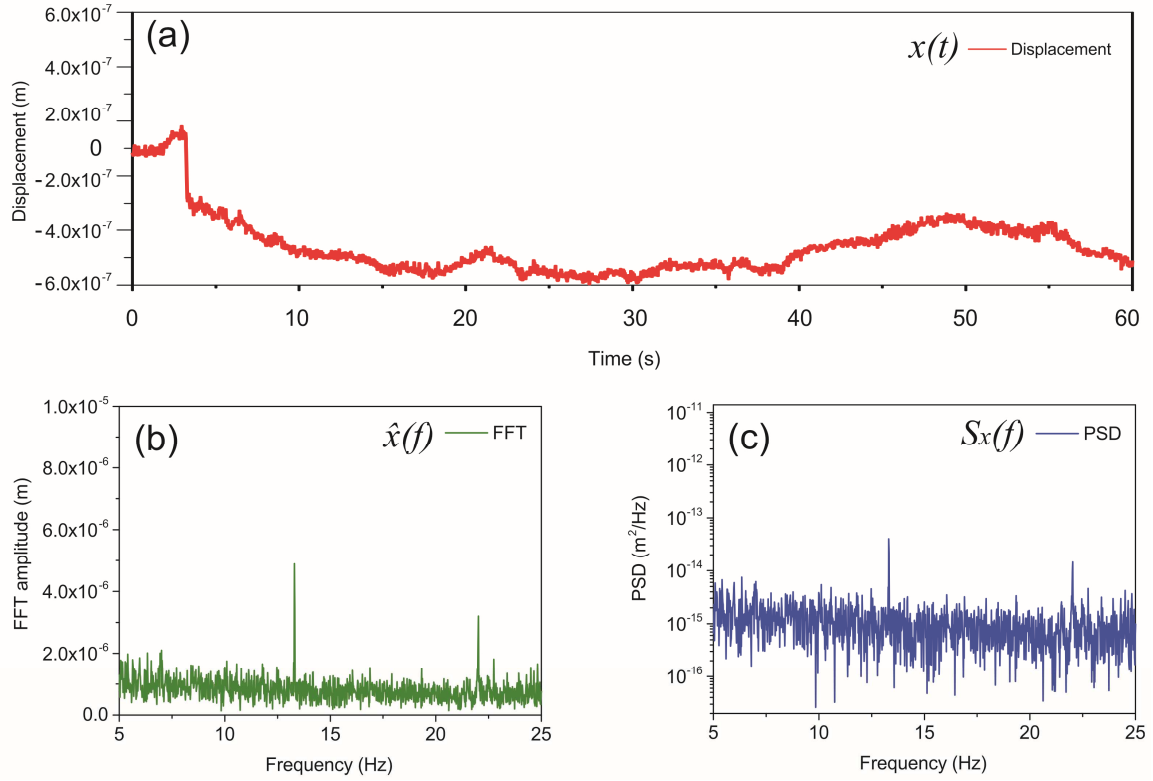

Figure 2.14 | (a) The time-displacement spectrum of a signal $x(t)$ sampled at 50 fps. (b) Fourier transform of the original signal. (c) Power spectral density analysis of the signal.

Chapter 3

Methods and Materials

In this chapter, the main experimental techniques that were used in this work, including the main materials that were used to perform the experiments, are described. The research of this dissertation is categorized into two parts, Chapter 4 and Chapter 5. The studies in both of these parts are based on the dark field microscope system, a detailed introduction of which is described in Section 3.1.1. The fluorescence microscope, which is used for characterizing cellular viability in this work, is also introduced in Section 3.1.2. The second part of this chapter (i.e., Section 3.2) contains all of the essential methods for preparing the samples and performing the measurements. Since living cells are the research targets of this work, a detailed description of cell culture techniques that are related to the measurement are listed in this section. Moreover, the optical manipulation of gold nanoparticles and single particle tracking in a living cell are the core techniques in this dissertation. However, only brief introductions are provided here since both of these methods are modified depending on the experiments and are discussed in detail in the following chapters.

3.1 Experimental Setups

3.1.1 Dark Field Microscope

Dark field microscopy (DFM) is the main imaging technique that is used in this thesis. Since it separates the scattered light from the illuminating light, samples can be visualized by DFM if they scatter light or possess luminescent properties. The fundamental principle of DFM is illustrated in **Figure 3.1**(a). In a DFM condenser, a specially sized opaque disc is placed under the condenser lens, such that the central part of the illuminating beam is blocked, forming a hollow cone of light. The light at the apex of the cone is focused at the plane of the specimen. Most of the light that enters the sample is directly transmitted, while some is scattered from the sample. Since the objective lens sits in the dark hollow of this cone, only the scattered light enters the objective lens and goes on to produce the image. The directly transmitted light travels around the objective lens and does not enter the cone shaped area. The achievement of this condition is determined by the coaxial conformation of the condenser, the objective and the numerical aperture (NA) of the lens system:

$$NA = n\,sin(\alpha) \tag{3.1},$$

where n is the refractive index of the surrounding medium and α is the half angle of the focused cone of light.

Successful dark field imaging requires that the NA of the condenser is higher than the NA of the objective, to ensure that no directly transmitted light enters the objective and disturbs the observation. As a result, the entire field of view appears dark when there is no sample on the microscope stage. Thus, it is named dark field microscopy. However, when a sample is placed on the stage it appears bright against a dark background. Due to the strong light scattering ability of metal nanoparticles, it is possible under dark field illumination, to observe gold nanoparticles down to a size of 20 nm in diameter, which are invisible in other microscope setups without additional labeling. Another unique advantage of DFM is that it enables the viewing of biological objects that are unstained,

transparent, and absorb little or no light. These specimens often have similar refractive indices to their surroundings, making them difficult to distinguish with other illumination techniques. For example, as illustrated in **Figure 3.1**(b), spherical gold nanoparticles of 80 nm in diameter and biological living cells can easily be observed simultaneously using DFM, making it possible to perform single particle manipulations on living cells.

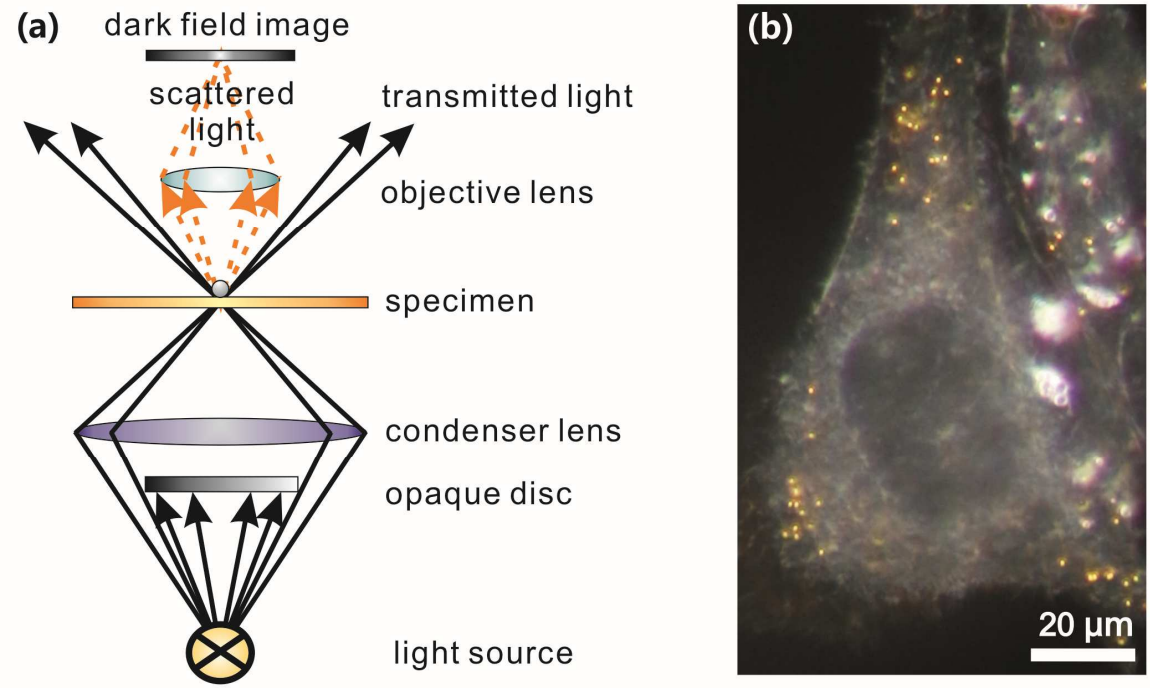

Figure 3.1 | Schematic illustrations of the DFM principle and the observed cell and gold nanoparticles. (a) Schematic view of the DFM optical path. The central part of the direct illumination light is blocked by a condenser system, to ensure that only scattered light from the specimen hits the objective. (b) CHO cell containing several 80 nm gold nanoparticles are imaged with the DFM. The contour of the cell is clearly observed and the golden dots represent the scattering from single gold nanoparticles. The clean glass substrate is illustrated as a black non-scattering background.

The DFM combined with the laser is the most important setup in this thesis, a diagram of which is shown in **Figure 3.2**. This setup is based on an upright microscope (Axiotech 100, Carl Zeiss MicroImaging GmbH). The illumination below the sample can be switched between a 100 W halogen lamp and a 50 W mercury lamp. The halogen lamp that covers

the entire visible spectrum of light is used in this work. Before entering the condenser, the light passes through an aperture to adjust the imaging area. An oil dark field condenser (Carl Zeiss MicroImaging GmbH) with an NA between 1.2 and 1.4 is used, which allows for observations with high magnification objectives. A special immersion oil with a refractive index that is matched to the glass (n = 1.518) is dropped on the top of a condenser lens and brought into contact with the bottom of the petri dish (ibidi GmbH). The petri dish is specifically used for cell culture and imaging. It has a glass bottom of 35 mm in diameter, 0.17 mm in thickness, and 2 ml in volume, and is sterilized before usage.

A self-made 3D-piezo stage is used to hold the petri dish. The stage is controlled by a gamepad and has an accuracy of 15 nm. Since the measurement is conducted in solution, a water immersion objective (Carl Zeiss MicroImaging GmbH) with a magnification of 100 x and an NA of 0.9 was used for imaging. The scattered light collected by the objective passes through a 50/50 beam splitter cube and enters the imaging systems which include: (1) an SLR digital camera (Canon EOS 6D) for taking optical pictures of the samples; (2) the ocular of the microscope for direct sample observation and positioning; (3) a grating spectrometer (Acton SpectraPro 300i by Princeton Instruments) coupled to a liquid-nitrogen cooled CCD (Princeton Instruments Spec-10) for obtaining spectral information of the detected light. All images and spectra are output to a computer for further analysis. The 50/50 beam splitter cube is used to couple laser into the microscope. The laser used here is a continuous wave (cw) diode-pumped Nd: YAG laser (Millennia V, Spectra Physics Lasers GmbH) with a wavelength of 532 nm and a maximum output power of 4 W. The laser focal plane and imaging focal plane are already aligned at the same level. A notch filter is placed behind the beam splitter cube to prevent any laser light from entering the imaging systems. To achieve a modulated laser beam, an optical chopper is placed on the laser path and its chopping frequency can be tuned using a controller system.

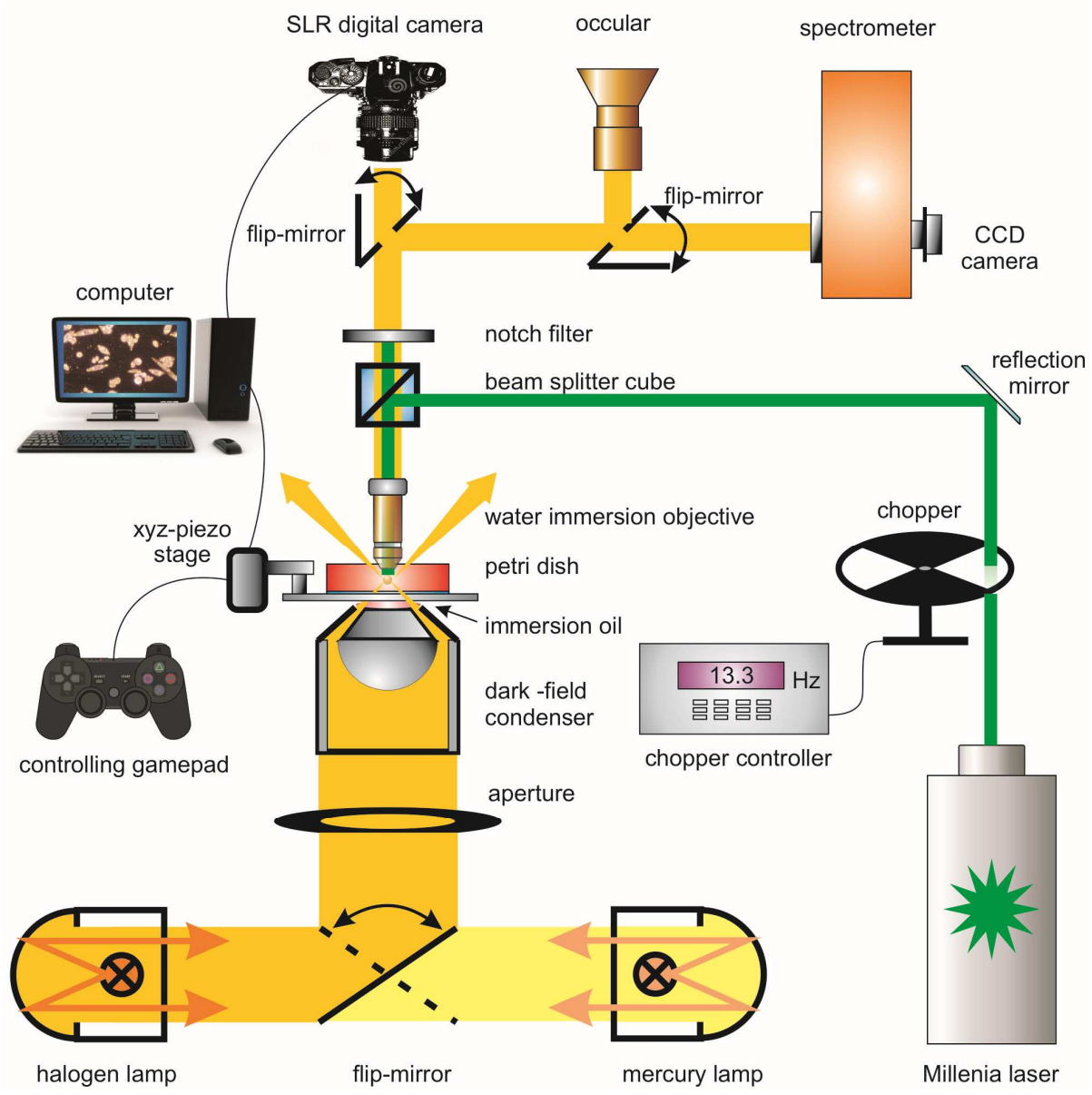

Figure 3.2 | Diagram of the dark field microscope imaging system equipped with a laser that was employed in the measurements.

3.1.2 Fluorescence Microscope

Fluorescence microscopy is a powerful analytical tool in biology and the biomedical sciences due to its combination of the magnifying properties of traditional optical microscopy with visualization of fluorescence. The application of wide selections of fluorochromes has made it possible to identify cells and subcellular structures with a high degree of specificity, which promotes studies on different cellular functions.

The principle behind fluorescence microscopy is illustrated in **Figure 3.3**. The main components of the fluorescent microscope overlap with the traditional inverted optical microscope, except for the light source and specialized filter elements. The halogen lamp is used as the illumination source of the sample as usual, while the mercury lamp is used as a light source for excitation due to the bright spectral bands that it generates within the visible wavelengths. As the light leaves the lamp, it is directed into a filter cube that consists of three components: an excitation filter, a dichroic mirror, and an emission filter. The excitation filter isolates one specific wavelength. Then, the dichroic mirror reflects the excitation light towards the sample, namely the excitation light will be reflected while the emission light can pass through. The reflected excitation light then passes through the objective and is focused onto the fluorescent specimen. The emitted fluorescent light passes back, first through the objective where magnification happens and then through the dichroic mirror. Before leaving the filter cube, the emissions are filter one more time by the emission filter, which helps to select the emission wavelength and suppress the backgrounds from lamp sources or other sources that are reflected off by the microscope components. Finally, the filter fluorescent light is sent to imaging systems. A 50/50 beam splitter cube is placed on the beam path to guide the fluorescent emissions to ocular for eye viewing and CCD camera for imaging, respectively. The filter cube is switchable, and the filter components of different wavelengths are commercially available for various fluorescent staining.

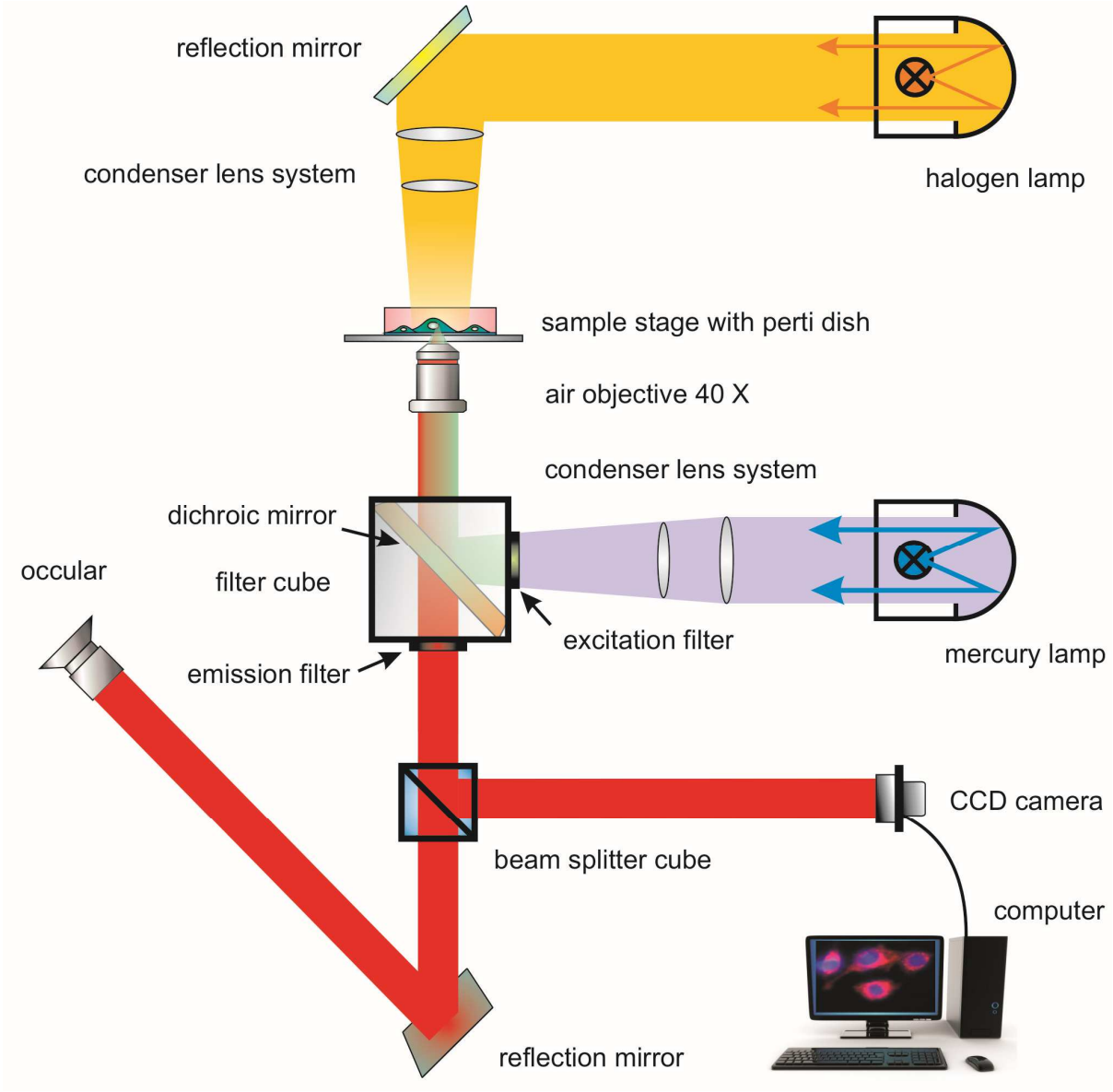

Figure 3.3 | Diagram of the principle of fluorescence microscopy.

3.2 Experimental Methods

3.2.1 Preparation of Glass Substrate

The petri dish with a hydrophobic glass bottom (Φ 35 mm, thickness 0.17 mm) was purchased from ibidi GmbH. To make it hydrophilic and more comfortable for cell attachment, the petri dish was first cleaned in the air-plasma for 15 min to remove any organic residue, and then disinfected in UV cleaner for 10 min before seeding the cells.

3.2.2 Cell Culture

Chinese hamster ovary (CHO) cells were used in this work. The cell line was derived from the ovaries of Chinese hamsters and is a commonly used mammalian cell model in biomedical and pharmaceutical research. They were first derived from a Chinese hamster by T. Puck from a lab at the Boston Cancer Research Foundation in 1957[141]. Since then CHO cells have been useful for many research purposes.

CHO-K1 (ATCC® CCL-61™), a common CHO derivative that contains a slightly lower amount of DNA than the original CHO, is used in this study. The purchased cell line was stored in the liquid nitrogen vapor phase before usage. To thaw the cryopreserved cells for subculture, the cryo-vial containing the frozen cells was removed from the liquid nitrogen storage and immediately placed into a 37 °C water bath. The cryo-vial was kept in the water bath with gently swirling until a small ice crystal was left in the cryo-vial. Then, the vial was transferred to a laminar flow hood and wiped with 70% ethanol for sterilization before opening. The content of the vial was then drop wised into a clean 75 cm^2 culture flask containing 14 mL of pre-warmed complete growth medium, namely the Ham's F-12 medium with 10% fetal calf sera (FCS). The newly thawed cells were kept in an incubator (with a humidified atmosphere of 5 % CO_2 and 95 % air at 37 °C) overnight; all of the cells attached to the bottom of the flask, and then the old medium that contained DMSO was replaced by fresh, warm complete growth medium. The flask was kept in the incubator for another 48 hours until the cell confluence reached 80% and subculturing could be conducted.

The maintenance of CHO cells follows the standard procedure that is provided by ATCC®. Specifically, when the cells 75 cm^2 culture flask reached the confluence of 60% to 80% (normally 48-72 hours after the last passage), the old medium was discarded and the cell layer was rinsed with PBS to remove all traces of serum that would inhibit the detaching reagent in subsequent steps. Three milliliters of a 0.25% (w/v) Trypsin / 0.53 mM EDTA solution was added to the flask to detach the cell. This process is also called trypsinization and is normally conducted in the incubator for 3-5 minutes. Since Trypsin is a proteolytic enzyme and it breaks down the proteins that enable the cells to adhere to the flask, the cell layers were dissociated from the container and each other. To stop the trypsinization, seven mL of complete growth medium was added to the flask. The cell suspensions were then dispersed by gently pipetting over the cell layer surface several times and transferring the supernatant into a 15 mL conical tube for centrifugation at approximately 1000 rpm for three minutes. The upper medium containing Trypsin/EDTA was discarded, and five milliliters of pre-warmed complete growth medium was added to re-suspend the cell pellet. For maintenance of the cells, three milliliters of cell suspensions were diluted with 12 mL warm complete growth medium, transferred into a 75 cm^2 culture flask, and cultivated in the incubator. To prepare the sample for experiments, 200 µL of cell suspensions were mixed with 1 mL of growth medium, seeded in a petri dish with a glass bottom (ibidi, Φ35mm, thickness 0.17 mm), and kept in the incubator.

3.2.3 Cell Quantification

In cell culture, keeping a consistent number of the cells is important for maintaining optimum growth during subculture routines, and it helps to standardize procedures, which in turn enhance the reproducibility of the results. Therefore, it is necessary to quantify the number of cells prior to use. In this work, the device that was used for counting cells is called a hemocytometer, which was originally designed to count blood cells and is now widely used for fast cell quantifications. As shown in **Figure 3.4**, the device consists of a thick glass microscope slide with a rectangular indentation that forms a counting chamber. When mounted with a cover glass on top of the slide, cell suspensions can be filled inside the chamber and observed with an optical microscope. Inside of the counting chamber, the slide surface is engraved with a gridded area consisting of nine 1 x

1 mm (1 mm^2) squares. Since the depth of the chamber is 0.1 mm, each square is given a defined volume. It is therefore possible to count the number of cells in a specific volume of fluid and calculate the concentration of cells in the fluid overall.

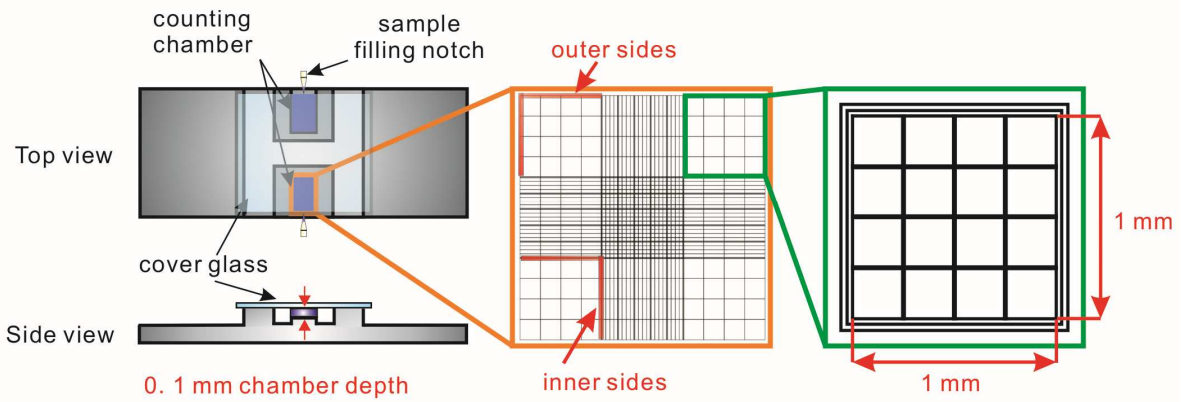

Figure 3.4 | Structure and working principle of the hemocytometer.

To perform the measurement, the adherent cells were brought into suspension by Trypsin/EDTA, as describe in Section 3.2.2. Under sterile conditions, 200 µl of cell suspension was removed and mixed gently with an equal volume of Trypan Blue solution (Sigma), which is a dye that selectively stains dead cells. Since dead cells do not have an intact membrane, the dye will penetrate into them and they will show a distinctive blue color under a microscope. The mixture (approximately 5-10 µl) was then filled into both sides of the chamber and viewed under an inverted microscope using 20 X magnification. Cells that were distributed in the four large corner squares were quantified (**Figure 3.4**). Specifically, the number of viable cells (seen as bright cells) and non-viable (stained blue) cells were counted; ideally, more than 100 cells should be counted in order to increase the accuracy. The cells that overlap the edge of the inner sides on the top and left should be included, and the cells that overlap the edge of the outer sides on the bottom and right should be excluded.

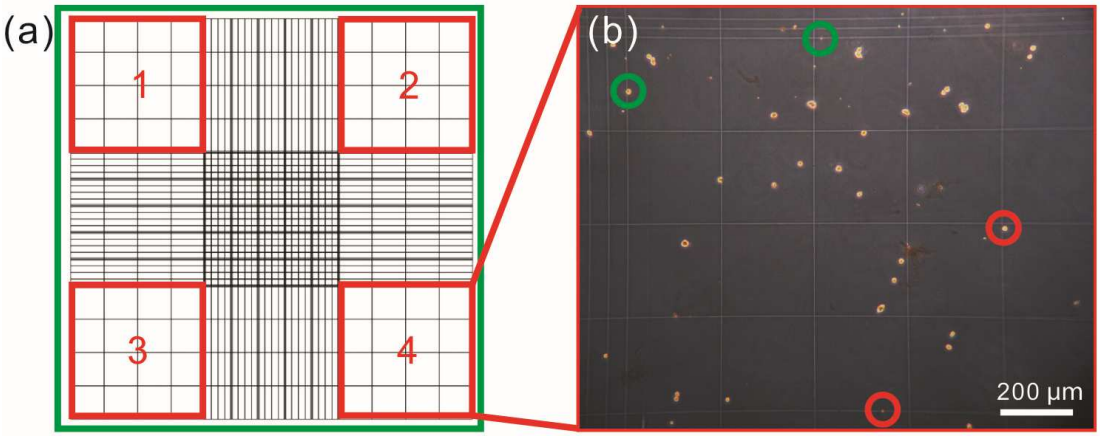

Figure 3.5 | Cell quantification in the gridded area of the hemocytometer. (a) The four large corner squares (red outlined) that are used for counting cells. (b) A microscope image of cells distributed in one of the large corner squares. Note that cells touching the left and top edges (green circled) should be included in the count, while cells touching the right and bottom edges (red circled) should be excluded.

As a result, the concentration of viable and non-viable cells and the percentage of live/dead cells could be calculated using the equations below:

$$N_{mL}^{live} = \frac{n_{live}}{n_{squares}} \times f \times 10^4 \tag{3.2}$$

$$N_{mL}^{dead} = \frac{n_{dead}}{n_{squares}} \times f \times 10^4 \tag{3.3}$$

$$Percentage\ of\ Viability = \frac{N_{mL}^{live}}{N_{mL}^{live} + N_{mL}^{dead}} \times 100\ \% \tag{3.4}$$

Here, N_{mL}^{live} represents the number of viable cells per milliliter; N_{mL}^{dead} is the number of non-viable cells per milliliter; n_{live} is the number of viable cells counted and n_{dead} is the number of non-viable cells counted; $n_{squares}$ is the number of large corners used for cell counting; f represents the dilution factor, which is two here since the mixture consists

of an equal volume of Trypan Blue solutions and cell suspensions. In addition, the volume of one large corner square = 1 mm^2 × 0.1 mm = 10^{-4} mL. Therefore, the number of cells per milliliter is multiplied by 10^4.

3.2.4 Cellular Uptake of Gold Nanoparticles

Gold nanoparticles are taken up by cells voluntarily, and the internalization pathway and intracellular distributions depend on various factors including the size, shape, charge, surface modifications, concentrations, and incubating time of the gold nanoparticles[54]. In this study, the cellular uptake of AuNPs was conducted by mixing nanoparticles with healthy cells for a certain period. The gold nanoparticles (obtained from Nanopartz™ Inc., USA) that were used here have a +30 mV surface potential, are 80 nm in diameters, and were supplied in deionized water with an initial concentration of 5.5×10^{11} nanoparticles/mL. CHO cells were seeded at a low density (1×10^5 cells/mL) in a petri dish, as described in Section 3.2.2, and cultured for 24 hours. Afterward, 5 µL of gold nanoparticle solution was added to the petri dish, yielding a final concentration of 2.3×10^9 nanoparticles/mL. Then, the mixture was incubated at 37 °C for another 24 hours. The uptake of gold nanoparticles can be directly observed under a dark field microscope or proven using the method described below in Section 3.2.5.

3.2.5 Gold Etching with KI/I_2 Reagent

A KI/I_2 mixture solution was used to oxidize AuNPs on the cell surface, leaving those that were internalized unreacted. A stock solution of KI/I_2 oxidation reagent was prepared by mixing 12.69 mg of I_2 and 49.8 mg of KI in 5 mL of deionized water, yielding final concentrations of 10 mM (I_2) and 60 mM (KI), respectively. The major role of KI is to increase the solubility of I_2 in water. The oxidation of AuNPs was directly observed under a dark-field microscope. Typically, after incubating the AuNPs with cells for a certain period of time or after laser injection of a single AuNP into the cell, 10 µL of KI/I_2 stock solution was added to 400 µL of a sample solution that contained cells. Oxidization was performed at room temperature for 1 min, and then the mixture was removed, the

culture dish was washed with 1 mL PBS, and 400 μL of fresh complete medium was added. Dark-field images were recorded using a digital camera (Canon EOS 6D).

3.2.6 Optical Manipulations of a Single Gold Nanoparticle

Nanoparticle manipulation with light is a powerful tool for the study of nanofabrication, sensing, analytics, biology, and medicine since it provides a non-invasive way to manipulate nano-sized objects[22]. The methods used here include laser printing and plasmonic heating of a single gold nanoparticle. The laser printing technique is based on A. S. Urban's report on printing individual gold nanoparticles directly from the colloidal suspension onto precise positions of a substrate[24]. The entire process was conducted in the dark field microscope described in Section 3.1.1. Before the experiments, the microscope table, sample holder, and objective lens were cleaned and disinfected using 75% ethanol. Cell culture dishes were sealed with Parafilm and only opened immediately before the experiment. The laser beam at 532 nm was focused on the substrate by a 100 X water objective. Spherical gold nanoparticles (diameter of 80 nm) in colloidal suspension would be captured once they diffused into the laser beam and then pushed towards the center of the beam. Printing occurs once the total optical force overcomes the electrostatic repulsive force between the nanoparticle and substrate, and the nanoparticles are immobilized firmly on the substrate. By moving the positions of the stage and the laser focal plane, the nanoparticles could be printed three-dimensionally at specific locations. The printing efficiency mainly depends on the laser power and the concentration of gold nanoparticles, such that printing a single particle or multiple particles at one site could be achieved by tuning the laser powers. The plasmonic heating of gold nanoparticles was done by focusing the laser beam at one gold nanoparticle using the dark field microscope. The increase in temperature on the gold nanoparticles is linearly proportional to the laser powers that are used for heating, which can be estimated using finite element simulations. In addition, modulated laser heating can be achieved by chopping the laser beam at a certain frequency (5-25 Hz) with an optical chopper placed on the beam path.

3.2.7 Single Particle Tracking in Living Cells

Once the gold nanoparticles were taken up by cells, the motion of the intracellular nanoparticles could be analyzed from the captured videos. The dark-field video of the cells that contained gold nanoparticles was recorded for a certain period of time at the speed of 50 frames per second, and the video file was analyzed by the particle-tracking software 'video spot tracker' (freeware provided by CISMM: Computer Integrated Systems for Microscopy and Manipulation). The manual for users is available freely online (http://cismm.cs.unc.edu/resources/software-manuals/video-spot-tracker-manual/).
This program enables the tracking of multiple particles at the same time and as a result, it reads out the spatiotemporal displacements of each particle in two dimensions in the form of x (t_n) and y (t_n) with $n=0, 1, 2, 3, \dots, N$. N is the total amount of frames in the recorded video.

3.2.8 Cell Viability Test

The cell viability was tested using the LIVE/DEAD® Viability/Cytotoxicity Kit for mammalian cells (Molecular Probes™, Invitrogen detection technologies), a commonly used method for examining cell viability and membrane damage, which is more sensitive than Trypan blue exclusion. The principle is based on the enzymatic conversion of non-fluorescent cell-permeant calcein AM to the intensely green fluorescent calcein by ubiquitous intracellular esterase inside of living cells. Dead cells, on the other hand, are identified by the bright red fluorescence of Ethidium Homodimer-1 (EthD-1), which can only enter cells if the plasma membrane is damaged and becomes fluorescent upon binding to nucleic acids. The stock solution of LIVE/DEAD assay reagents was prepared by adding 20 µL of supplied 2 mM EthD-1 stock solution and 5 µL of supplied 4 mM calcein AM stock solution to 10 mL of sterile tissue culture-grade PBS, and vortexing for thorough mixing; this resulted in approximately 2 µM of calcein AM and 4 µM of EthD-1 working solution. CHO cells were cultured on a grid petri dish with a glass bottom (ibidi, grid size 500 µm). A grid petri dish was used to relocate the cell when transferring the samples from the dark-field microscope to the fluorescence microscope. Immediately after laser printing or injection experiments, the cells were gently washed with 1 mL PBS, and 200

µL of combined LIVE/DEAD assay reagent was added to the culture dish and incubated with a covered lid at room temperature for 30 min before transferring it to the fluorescence microscope for imaging. The percentage of live cells and dead cells can be calculated by counting the number of red and green stained cells:

$$Live\ Cells\ (\%) = \frac{N_{green}}{N_{green} + N_{red}} \times 100\ \% \tag{3.5}$$

$$Dead\ Cells\ (\%) = \frac{N_{red}}{N_{green} + N_{red}} \times 100\ \% \tag{3.6}$$

where N_{green} indicates the number of green stained cells and N_{red} is the number of red stained cells.

Chapter 4

Delivering Gold Nanoparticles to Living Cells with a Laser Beam

Nanoparticles promote the development of contemporary personalized medicine that aspire the diagnostics and treatment of a disease in a single system[142, 143]. Among a variety of nanoparticles, gold nanoparticles (AuNPs) have a long history of utilization in the human body for biomedical reasons[3]. They are increasingly used in more precise manners for cellular imaging, diagnosis, and biosensing[144] because of their superior chemical, biological, and optical properties, which include easy surface modification for functional molecular attachment[145, 146], excellent biocompatibility[146, 147] and the conversion of light into heat upon irradiation at their plasmon resonances[22]. While there have been many reports on the nanotheranostic applications of nanoparticles inside of living cells[148, 149], the major challenge is to find proper means of delivering particles one-by-one to the cell surface or into the interior with full spatiotemporal control and high precision. This chapter demonstrates a novel delivery approach to optically printing a single gold nanoparticle with a diameter of 80 nm on the cell surface and then injecting it into the cells. Section 4.1 shows that individual gold nanoparticles from a solution can be patterned on the surface of living cells in a controllable way with a continuous wave laser beam. Section 4.2 demonstrates how the same particles can, in a second step, be injected into the cells through a combination of plasmonic heating and optical force. Moreover, the injection mechanism is discussed in detail in this section. The last section describes the test of the cell survival rate following the optical printing and injection and looks forward at this highly reproducible and controllable injection method offering promising prospects for follow-up applications in biomedicine and biosensing areas.

4.1 Optical Printing of Gold Nanoparticles on Cell Membranes

The mammalian cell membrane is the main barrier that separates the intracellular environment from the outside. Any exogenous objects to transport inside of the cell must be in contact with the cell membrane initially. Therefore, studying the interaction of a cell membrane with these objects and bringing them to the cell membrane is the key to successful cellular delivery. Since gold nanoparticles have long been used as the reagent for cellular imaging, diagnosis, and therapy, various strategies have been exploited to assist their affinity to cell membranes. The simplest method relies on electrostatic interactions. The surface of AuNPs are capped with positively charged molecules and can deposit on the cell membranes[150]. This method usually has low controllability and is likely to result in nanoparticle aggregation. A more efficient and popular approach is based on the ligand-receptor interactions. An AuNP's surface is easy to modify with various ligands that target specific receptors on cell membranes and facilitate their targeted delivery. Many reviews and research articles have reported these methods[123, 151]. In addition, one can use AuNPs tagged liposome to deliver AuNPs to the cell membranes, which shows more stability since the AuNPs are covalently bound to the lipid surface[152]. However, these methods are still performed in bulk cell solutions and single-cell and single-particle resolutions are difficult to reach.

In this section, an entirely optical strategy, which is more precise and controllable to deliver the AuNPs on the cell membrane, is presented. This approach is based on A. S. Urban's report[24] about laser printing AuNPs on a glass substrate, and is further developed and applied to living cells in this study. As explained in Chapter 3, the CHO cells were cultured in a petri dish and imaged on dark field microscope. Before printing, the old medium of cell culture was discarded and the cell sample was washed with PBS three times to remove the protein residues, which could bind to AuNPs unspecificly. Then 400 µL of Leibovitz's L-15 Medium that contained 5×10^9/mL 80 nm of AuNPs was added to the culture dish (culture medium: AuNPs solution = 40:1). The surface of the AuNPs were negatively charged (the same as cell membranes), such that the probability of the interactions between cells and AuNPs without any active manipulations was extremely low during the two hours. The Millennia V laser at 532 nm (cw mode) was coupled into

the microscope and focused by a 100 X water immersion objective, resulting in a spot size of 604 nm (FWHM) on the glass substrate underneath a cell. Therefore, a large illumination area was on the cell membrane. AuNPs in the solution that was entering the laser beam were exerted by a forward directed scattering force, pushed toward the substrate at a high speed, and then positioned on the cell membrane. A diagram of these steps is shown in **Figure 4.1**.

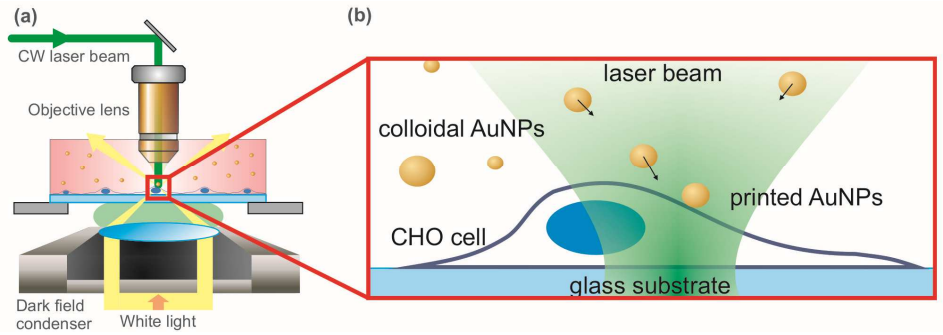

Figure 4.1 Diagram of laser printing gold nanoparticles on the cell membrane.

At low laser powers, the gold nanoparticles were accelerated by the laser towards the cells, but were not bound to the membrane and diffused through the solution. **Figure 4.2**(a-c) shows the situation when the laser power was set at 1 mW. Although the laser was kept on for 30 seconds, the gold nanoparticles were not printed on the cell membrane. After increasing the laser power to a value of 5 mW during the same exposure time, one gold nanoparticle began to attach to the cell surface (**Figure 4.2**d-f). Increasing the laser power further (10 mW: **Figure 4.2**g-i; 25 mW: **Figure 4.2**j-l), more gold nanoparticles were printed on the cell membrane during the same illumination period. The printing efficiency depends on the laser power, gold nanoparticle concentration in the solution, and laser illumination time. Thus, one must balance these three main factors to achieve a proper printing event. These values of laser powers are far above the values that are necessary for gold nanoparticles with the same properties to be printed onto the glass substrate. In this study, however, the gold nanoparticles concentration in the solution was kept low to prevent them from spontaneously binding to cell membranes. In addition, the laser beam was focused on the substrate underneath the cell; therefore, the power density at higher positions (*i.e.,* on the cell the membrane) was reduced to

ensure that the optical forces on the nanoparticles were weaker than the optical forces on the laser focal point. In addition, the surface properties of cell membranes are more complicated than the properties of a clean glass substrate. As such, their interactions with gold nanoparticles are difficult to predict. Thus, one must use relatively high laser powers to capture the gold nanoparticles and print them on cell membranes.

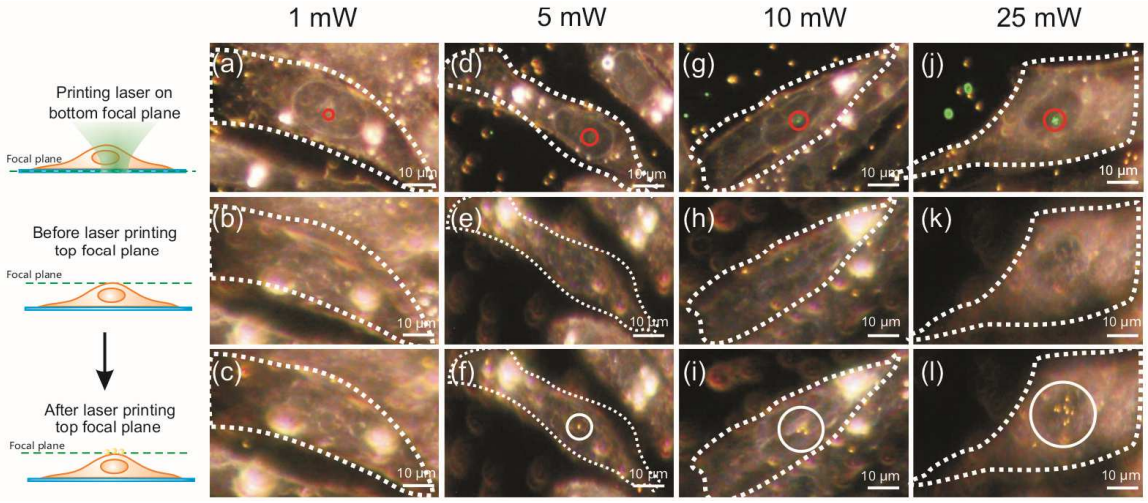

Figure 4.2 | Printing gold nanoparticles on cell membranes at different laser powers. The top row shows the images where the focal plane is on the glass substrate and the laser is on. Clear cell outlines (white line) and laser illuminating sites (green spots highlighted with red circles) can be identified. The middle and bottom panels show the images before and after laser printing, respectively. The focal planes are both set at the top of the cells, such that gold nanoparticles can be easily observed once they are printed (white circle). During 30 seconds of laser illumination, no particle was printed at a laser power of 1 mW (a-c); only one particle was printed on the membrane at 5 mW (d-f); and multiple particles can be printed at 10 mW (g-i) and 25 mW (j-l).

The printing method presented here is an alternative method for delivering gold nanoparticles to the cell membranes since it has high spatiotemporal controllability. By moving the laser beam to different areas, it is possible to print gold nanoparticles one-by-one specifically onto targeted sites on the cell surface. **Figure 4.3** illustrates the experiments of targeted printing. In order to achieve high printing efficiency, the laser power was set to 25 mW. Three positions on the cell surface were illuminated with the printing laser beam for 60 seconds. After printing, gold nanoparticles patterns were visible on the cell membrane, distributed over a large area around the three points of

laser treatment. In order to achieve higher precision at the single particle level, the laser power was decreased to 5 mW. During the same exposure time (60 seconds) at each printing position, up to two gold nanoparticles were delivered to the membrane. However, as mentioned above, the printing efficiency depends on laser power, exposure time, and gold nanoparticle concentration. Decreasing exposure time while keeping high laser power, for example, could also achieve single particle printing. Thus, one must take all factors into account when conducting optical printing to obtain the desired results.

In general, the results that are presented here indicate that gold nanoparticles can be optically delivered to cell membranes. An advantage over similar delivery strategies is that this method can be used in more general cases since the gold nanoparticle surface does not need specific modifications that target a certain cell type because the delivery relies on optical forces rather than chemical bonds between nanoparticles and the cell surface. Moreover, molecular delivery at the single particle and single cell level was achieved using this method. By tuning the experimental parameters, it is possible to position a single gold nanoparticle at one time to the desired position on a single cell's membrane. This controllable precision will facilitate further studies on nanoparticle-cell interactions.

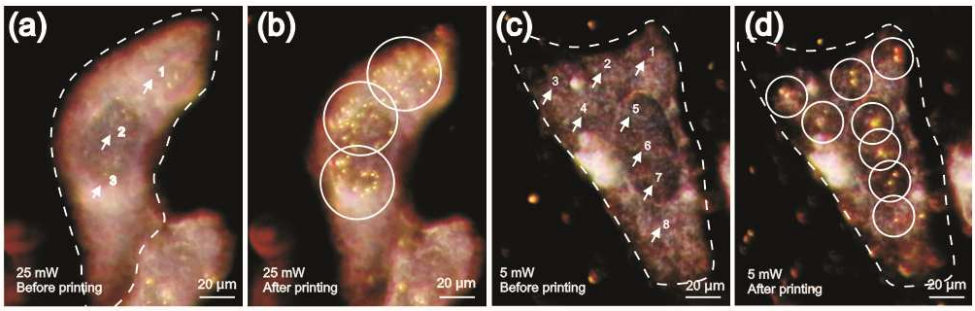

Figure 4.3 | Printing gold nanoparticles on cell membranes at targeted sites. Different spots on the cell surface were irradiated with a green laser. Gold particles that are diffusing in the cell media are pushed towards the cell surface by a forward directed scattering force as soon as they enter the laser beam. In the dark field images above, the white arrows indicate the laser illumination points and the numbers show the printing orders. The illumination time at each numbered point is 60 seconds. Printed gold nanoparticles at each printing position are circled. (a-b) Before and after printing using a laser power of 25 mW. (c-d) Before and after printing using a laser power of 5 mW.

4.2 Laser Injection of Gold Nanoparticles into Living Cells

A novel strategy for delivering gold nanoparticles to cell membranes using a completely optical method has been discussed. This section takes a step further to demonstrate how individual gold nanoparticles, which were already patterned with high control and precision on the surface of a living cell, can be injected one-by-one into the cell using a combination of optical forces and plasmonic heating.

The injection of individual particles inside of the cells is accomplished in a two-step process. First, gold nanoparticles are printed on the cell membrane by optical force, which is discussed in Section 4.1. After the printing, the medium is rinsed to remove excessive gold particles (**Figure 4.4**a). Finally, injection occurs when the laser beam is focused directly on a single particle that is attached to the cell membrane to achieve the strongest increase in optical force and temperature (**Figure 4.4**b).

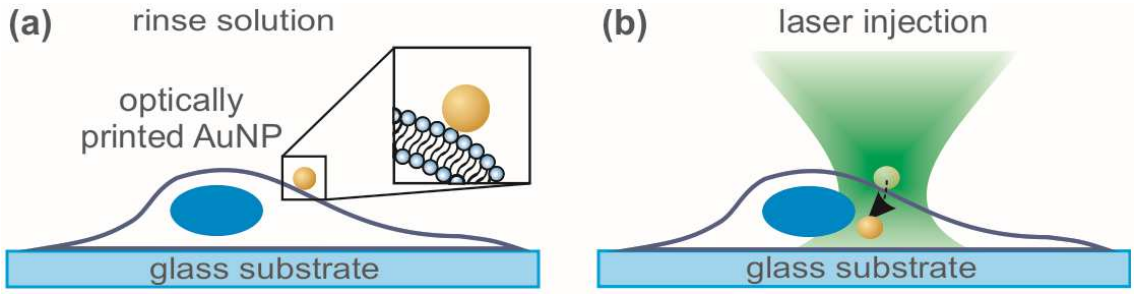

Figure 4.4 | Laser injection of gold nanoparticle into living cell. (a) After printing, particles in the solution are washed away. (b) For nanoparticle injection, the laser beam is focused directly on individual gold particles to induce the highest amount of heat and force to push the particles directly into the cell.

4.2.1 Targeted Injection of Gold Nanoparticles into a Single Cell

The result of the complete injection process for a single cell is shown in **Figure 4.5**. CHO cells were grown in a glass bottom culture dish at a confluence of 60% to 80%, as described in Chapter 3. Gold nanoparticles with a diameter of 80 nm were added to the culture dish with fresh Leibovitz's L-15 Medium (culture medium: AuNPs solution = 40: 1). The particles were stabilized with a citrate coating to avoid unspecific attachment to the cells (**Figure 4.5**a). First, four gold nanoparticles were printed next to each other onto the surface of a single cell (**Figure 4.5**b) using the method described in Section 4.1. The power of the printing laser was 5 mW and the exposure time was 60 seconds. Then, two of the nanoparticles (**Figure 4.5**c, Nr. 1 and Nr. 4) were injected into the cell by focusing the same laser beam directly onto them. The laser exposure time for each particle is estimated less than one second. The successful injection was immediately visible under the microscope since the irradiated particles were pushed out of focus to a lower focal plane in the cell center (**Figure 4.5**c lower panel).

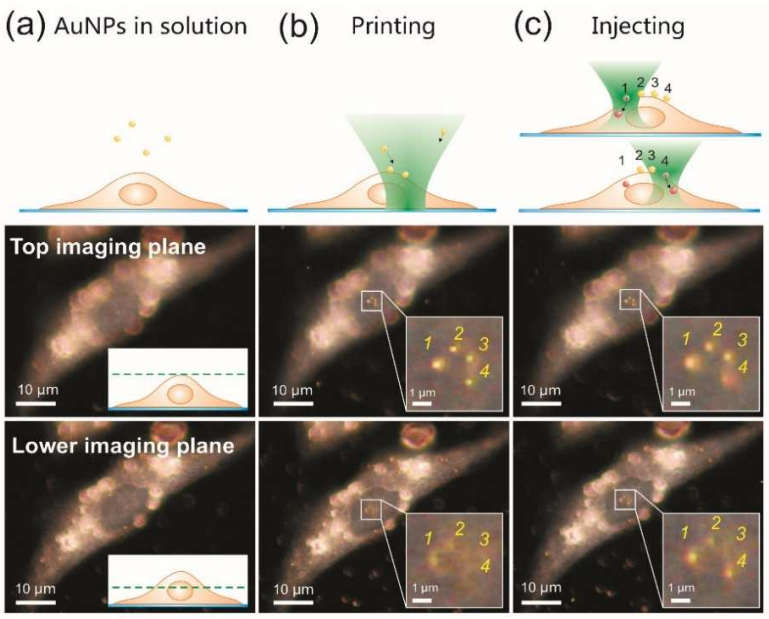

Figure 4.5 | Dark field images for laser printing and injection of gold nanoparticles into a cell. (a) CHO cells growing on the glass bottom petri dish were mixed with 80 nm particles and the cells were imaged at two different focal planes (top and lower panel). (b) A laser beam (λ=532 nm) was focused on the glass substrate underneath the cell to print four particles (Nr. 1 to 4) to the cell surface. (c) Nanoparticle injection was achieved by focusing the laser directly onto single selected particles (Nr.1 and Nr.4) for 1 second at a laser power density of 1185 kW/cm^2 of each gold nanoparticle.

To prove that the gold nanoparticles were inside of the cell, a method that was reported by Xia *et al.*[153] was used. As illustrated in **Figure 4.6**, the combination of KI/I_2 is used as an etching reagent to selectively dissolve any gold nanoparticles on the cell surface, while those that are inside of the cell are protected and are not exposed to the chemical reagent since KI/I_2 in solution is impermeable to the cell membrane. Here, iodine acts as a strong oxidant to oxidize gold while potassium iodide is used to increase the solubility of iodine in water. In this study, The KI/I_2 stock solution was prepared following the procedure that is presented in Section 3.2.5. It is important to note that although I_2 has a strong oxidability, it is of low toxicity to cells when used below 0.34 mM. A cell viability of over 90% was confirmed after an etchant exposure for over 5 min, which was in agreement with the previous reports[153].

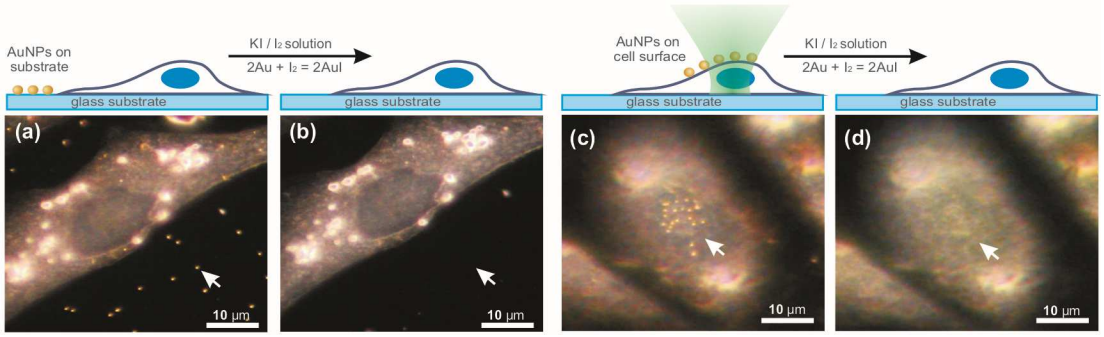

Figure 4.6 | Evidence that the gold nanoparticles are dissolved by the KI/I_2 solution. (a) Gold nanoparticles are either deposited on the glass substrate or (c) optically printed on the cell membrane. The arrows indicate the presence of the gold nanoparticles. (b, d) After adding KI/I_2 solution, the gold nanoparticles exposed in the solution are dissolved and invisible in dark field images.

The progress of etching that was directly observed under the dark-field microscope was recorded as a video, the captured images of which were shown in **Figure 4.7**. Four gold nanoparticles, two of which (**Figure 4.7**a, lower panel Nr. 1 and Nr. 4) were optically injected as described above, while the other two particles (**Figure 4.7**a, top panel Nr. 2 and Nr. 3) were still sitting on the cell membrane. After 10 seconds of adding the KI/I_2 etchant (**Figure 4.7**b), the scattering intensity of particles Nr. 2 and Nr. 3 could directly be seen decreasing compared to the time that etching began, which indicates that the gold

nanoparticles were dissolving gradually. Twenty seconds after the addition of the reagent, particles Nr. 2 and Nr. 3 completely disappeared while particles Nr. 1 and Nr. 4, which were injected into the cell, were unharmed (**Figure 4.7**c). This result implies that the gold nanoparticle is injected through the membrane while the permeability of the membrane is not affected after injection, as we did not observe the etchant entering the leaking cell membrane and dissolving gold nanoparticles inside of the cell. However, it is believed that the membrane will not be intact where the gold nanoparticle entered since the heat that is generated in this situation is sufficient to melt the lipid molecules. One explanation for this is that the cell membrane was damaged during injection to let the particle penetrate, but recovered within minutes after the particle was inside of the cell. This hypothesis will be further proven by the cell Live/Dead experiment that is described in later sections.

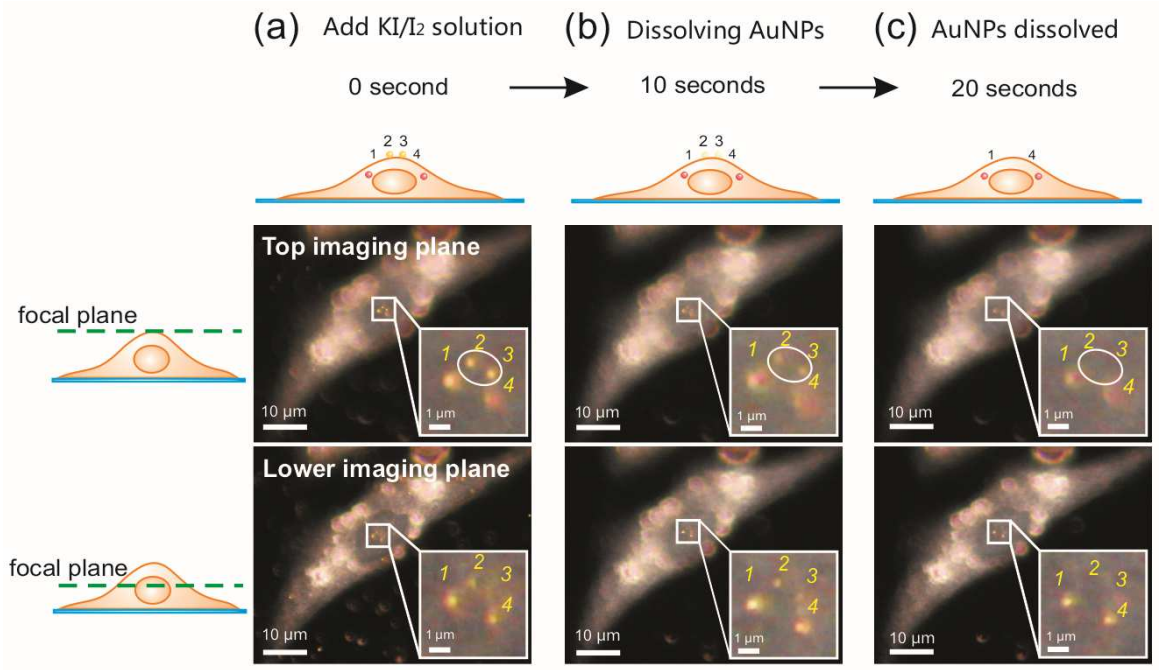

Figure 4.7 | The progress of the etching gold nanoparticles on the cell surface. (a) After optical injection, the KI/I_2 solution was added to the cell culture medium. (b) 10 seconds later gold nanoparticles that are attached to the cell membrane (Nr.2 and Nr.3) are dissolved partially. (c) After 20 seconds, the gold nanoparticles on the cell surface were completely dissolved while the particles that were injected into the cell (Nr.1 and Nr.4) are preserved.

4.2.2 Spectroscopy Characterization of Injected Gold Nanoparticles

As discussed in Section 2.1, the resonance frequency of a gold nanoparticle shows a strong dependence on the dielectric constant of the surrounding medium according to the Clausius–Mossotti relation. This indicates that a gold nanoparticle can be used to sense local changes of the refractive index. Differences in the intracellular and extracellular environments result in changes in the refractive index. Therefore, the gold nanoparticle inside of the cell can be distinguished from the one outside of the cell by comparing their plasmon resonance.

Here, the successful injection of the gold nanoparticles was also confirmed by Rayleigh scattering spectroscopy as shown in **Figure 4.8**. A single gold nanoparticle was laser printed on the cell, and a scattering spectrum was recorded (**Figure 4.8**a). The same particle was then injected into the cell, and the scattering spectrum of the particle was recorded again (**Figure 4.8**b). The comparison of both spectra showed that the resonance peak was shifted from 555 nm to 565 nm after injection (**Figure 4.8**c), which agrees well with the simulation result that is expected due to the refractive index change from the outside (n~1.33) to the inside (n~1.38) of the cell[154, 155] (**Figure 4.8**d).

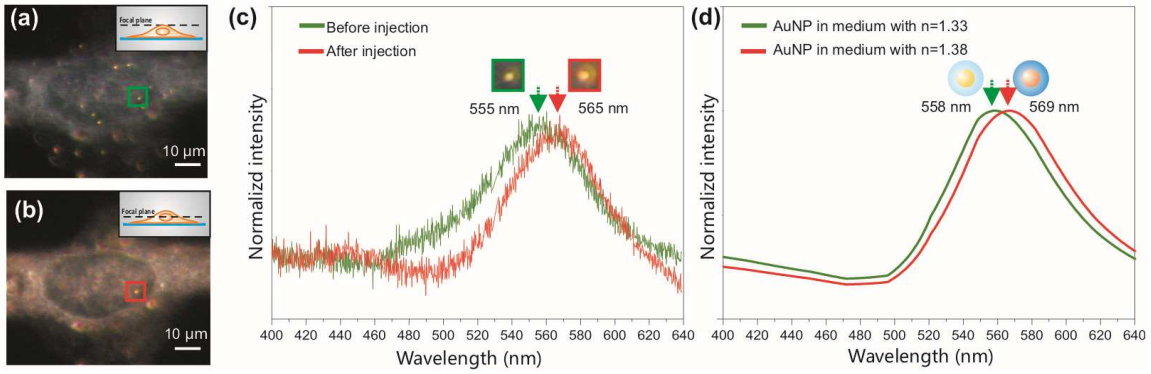

Figure 4.8 | Rayleigh scattering spectroscopy of a gold nanoparticle before and after laser injection. Dark-field images of gold nanoparticle before (a) and after (b) injection into the cell. (c) The spectra showed a red shift of approximately 10 nm following laser injection which corresponds to the simulated spectra (d) with a change in the refractive index from 1.33 to 1.38 from the outside to the inside of the cell.

4.2.3 The Mechanism of Laser Injection

4.2.3.1 Laser Power-Dependent Manner

As the laser printing experiment highly depends on laser power, it is important to consider the laser power for laser injection. To study the impact of laser power upon injection, gold nanoparticles were printed on a cell membrane using the method described above, and then gold nanoparticles were irradiated by a focused laser beam at the total laser powers of 1, 5, 10, and 25 mW. On each single cell membrane, only one single gold nanoparticle was irradiated at one chosen laser power, which led to the laser power density that reached the surface of individual gold nanoparticles varying at 237, 1185, 2370, and 5925 kW/cm^2 (for calculations see **Appendix A**). The experimental result was shown in **Figure 4.9**. In all cases, multiple gold nanoparticles were printed on a cell membrane, but only one particle was chosen for injection. When a particle was irradiated at 237 kW/cm^2 (1 mW in total), the injection did not occur (**Figure 4.9**a-d). When the laser power increased to 1185 kW/cm^2 (5 mW in total), the irradiated particle was successfully injected while the particles around it were not affected and remained on the membrane, which is illustrated in **Figure 4.9**(e)-(h). However, as the laser power density at the gold nanoparticle continued to increase to 2370 kW/cm^2 (10 mW), the irradiated particle and some surrounding particles were injected together (**Figure 4.9** i-l). The high laser power density at 5925 kW/cm^2 (25 mW) was also tested, the particle in the laser focal center, together with most of the surrounding particles on the membrane were injected simultaneously into the lower part of the cell immediately upon laser irradiation. This can be seen by comparing the images at different objective focal planes in **Figure 4.9**(m)-(p).

4.2.3.2 Optical Forces during Laser Injection

The laser power dependence of optical injection can be further explained by studying the optical force and temperature increases at the gold nanoparticle. As discussed in Chapter 2, when a gold nanoparticle enters the laser beam, it is subjected to an optical force that points in the direction of laser propagation. Meanwhile, the particle's absorption of light leads to a temperature increase on its surface. Together, the optical force and the heating effect contribute to the successful optical injection.

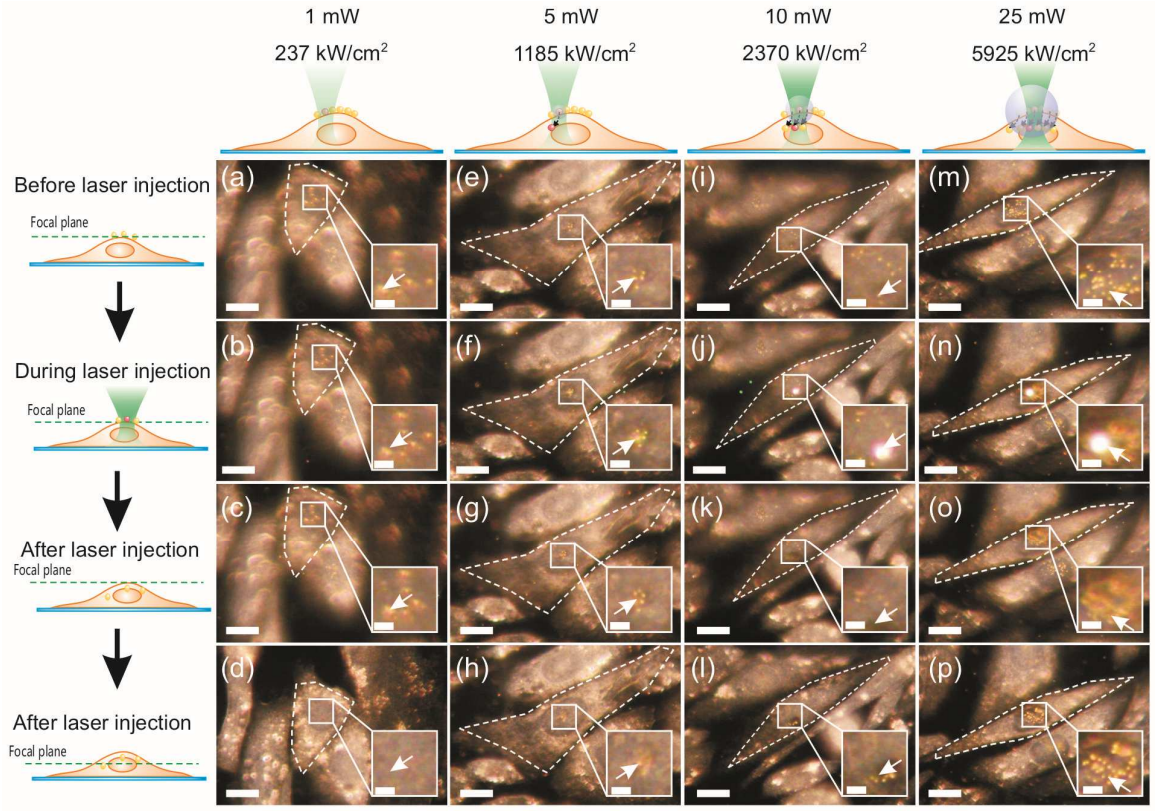

Figure 4.9 | Laser power dependence of optical injection. Only single gold nanoparticles on individual cell membranes were irradiated with one specific laser power. The images in the vertical column show the injection conducted at a laser power of 1, 5, 10 and 25 mW, while the images in horizontal rows indicate the process of injection and the visions at different focal planes. (Scale bar: 10 µm, insets: 2 µm)

To reveal the nature of the injection mechanism, numerical calculations (see **Appendix A** and **B**) were performed to estimate the amount of heat and force that is induced by the laser beam during the printing and injection experiments. The force maps of the calculated total optical forces that were exerted on the gold nanoparticles for different laser powers are shown in **Figure 4.10**(a)-(c). Experimentally, it was found that a laser power of at least 5 mW was necessary to inject particles successfully and reproducibly into the cell, which corresponds to a total force in the pN range. In the case of high laser power (*i.e.,* using 10 mW) the total optical force was 15~20 pN, which is still too weak[156] to push a particle through the membrane without other assisting effects.

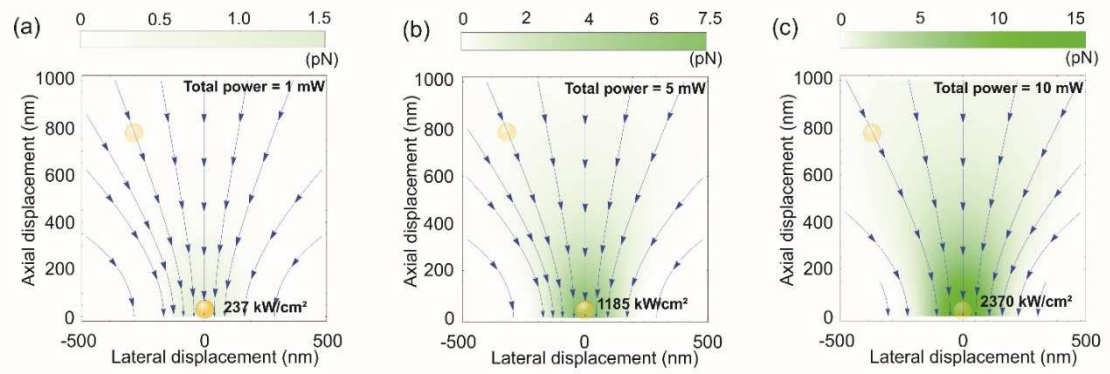

Figure 4.10 | Maps of optical forces on gold nanoparticle during laser injection. The optical forces that were exerted on 80 nm gold nanoparticles upon exposure with a Gaussian laser beam (λ=532 nm) at the power of (a) 1 mW, (b) 5 mW and (c) 10 mW were calculated using Mathematica 9.0. The color indicates the magnitude of the total force. The arrows illustrate the direction of the force that guides the particle along the optical axis and towards the cell membrane.

4.2.3.3 Temperature Simulation during Laser Injection

In general, high laser power leads to strong optical forces, but it also results in stronger heating. During printing, the heating of the particle was not significant since the beam is focused on the surface of the underlying substrate, and the nanoparticle is within the defocused region of the laser beam. For the injection, however, the laser is directly focused on the particles where the light intensity is maximal, which leads to a strong and instantaneous increase in the nanoparticle's temperature. We simulated the steady state temperature increase at the surface of the gold nanoparticle that was irradiated with a resonant cw laser beam. The result indicates that the temperature is linearly related to the value of laser powers (**Figure 4.11**a). Irradiation with a laser power density of 237 kW/cm^2 (which corresponds to the total power of 1 mW) resulted in 112 °C at the surface of the gold particle. At a moderate laser power density of 1185 kW/cm^2 (total power 5 mW), the surface temperature of the gold nanoparticle reached 480 °C. Increasing the laser power further, the temperature of the gold nanoparticle can reach approximately a thousand degree Celsius or above.

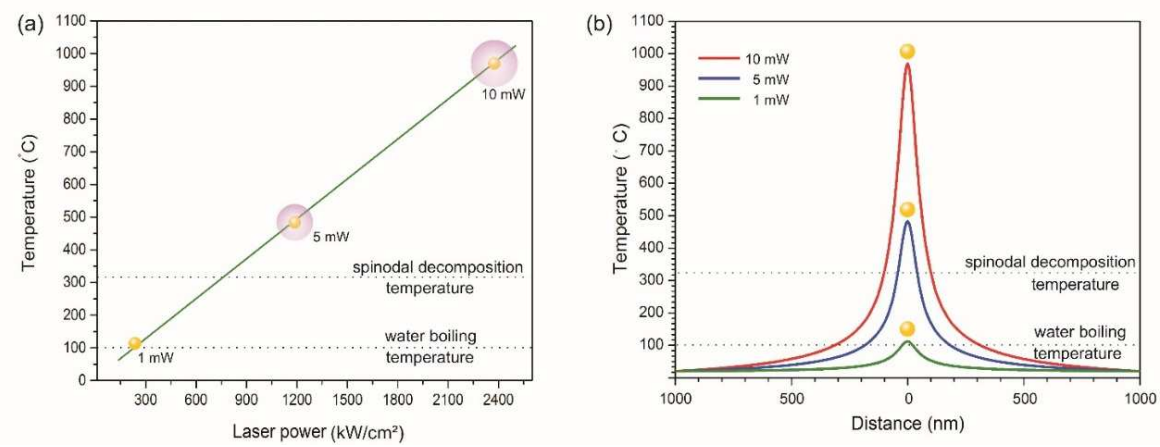

Figure 4.11 | Simulation of gold nanoparticle temperature. (a) Calculated AuNP temperature as a function of laser power. Nanobubble formation was experimentally observed for a particle temperature above 320°C. (b) Temperature distributions of AuNP irradiated with 532 nm cw laser beam.

4.2.3.4 Bubble Formation

Although the temperature at the center, where the gold nanoparticle sits, is high, it decays dramatically and significantly with increasing distance to the gold nanoparticle. This is demonstrated in the temperature distribution curves in **Figure 4.11**(b). The heat is confined in a nanoscopic volume, and the surrounding temperature decreases sharply below 100 °C within a few hundred nanometers. However, with a laser power of 5 mW or higher, heating can lead to nanobubble formation (see **Figure 4.9**), namely if the water temperature increases above the spinodal decomposition temperature of 320 °C[157]. The bubbles are shown as white flashing lights in dark field microscopy, and the size is estimated at a few hundred nanometers or larger at the higher laser power. This finding is critical to the explanation and understanding of the optical injection mechanism since

the optothermally excited bubbles play an important role in the injection process. At low laser power (1 mW) where the injection did not happen, the bubbles were also not observed, while nanobubbles were always seen for laser powers of 5, 10, and 25 mW, where the surface temperature of the gold particles was well above 320 °C. This is true and was proved by the control experiment where individual gold nanoparticles sitting on a cell membrane and a glass substrate were irradiated by the injection laser beams at the powers that were used for the injection experiment (**Figure 4.12**). We assume that the expansion and collapse of these bubbles are accompanied by a shock wave that caused the rupture of the cell membrane, which is also reported in the literature[158]. At this point, the scattering forces that are exerted on the nanoparticle lead to its injection into the cell through a membrane 'hole'. This can explain the reason that multiple gold nanoparticles were injected at the same time using a high laser power, though only a single particle was irradiated. The bubble formed and expanded to a larger size with high laser energy at the targeted gold nanoparticle, and therefore, the membrane underneath the surrounding particles was ruptured, causing the penetration of multiple particles simultaneously.

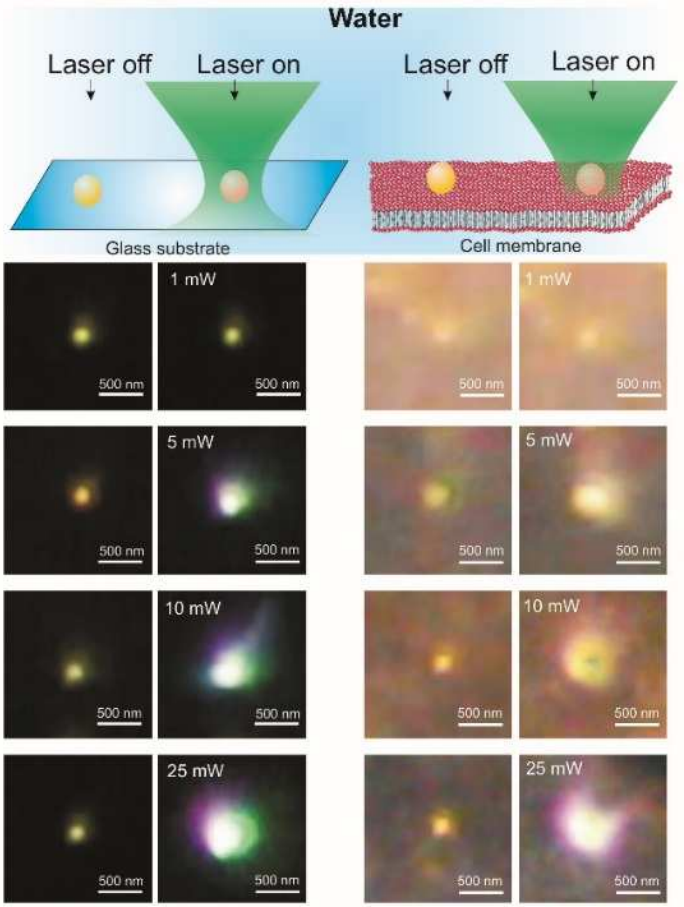

Figure 4.12 | Observation of bubble formation. 80 nm gold nanoparticles were attached to a glass substrate (left panel) or a cell membrane (right panel). The formation of nanobubbles was observed on both, the glass substrate and the cell surface, upon irradiation with a green laser beam for laser powers ranging from 5 to 25 mw.

From the discussion above, nanobubbles were always formed in this study, and the injection was highly reproducible for a laser power of 5 mW (which corresponds to a laser power density of ~1185 kW/cm^2), where the surface temperature of the gold nanoparticle is well above the water spinodal decomposition temperature (**Figure 4.11**a). For comparison, no bubble formation or nanoparticle injection was observed for a laser power of 1 mW (laser power density ~237 kW/cm^2) where the temperature of the gold nanoparticle is near water-boiling temperature. Therefore, it will be interesting to study the situation of injection between 1 and 5 mW, in order to find the possible minimum injection requirement. Since the laser power is linearly proportional to the temperature of a gold nanoparticle, it is easy to control the gold surface temperature by tuning the laser irradiation power.

Here, we tested the injection experiment at laser powers of 2 mW, 3 mW, and 4 mW where the temperature of the gold nanoparticle was around 224, 336 and 420 °C (**Figure 4.13**a). The results demonstrate that for the laser power of 2 mW, where the temperature of the particle lies between spinodal decomposition temperature and water boiling temperature, the particle was overheated and diffused slightly on the membrane, but no bubble was observed and no injection occurred (**Figure 4.13** b-c). This matches the reported effect that only the thermal expansion happens at a single AuNP and surrounding thin liquid layer, which is accompanied by the generation of the linear acoustic wave if the temperature of gold is < 150~350 °C.[159] When the laser power increased to 3 mW, where the temperature of gold is around the spinodal decomposition temperature, bubble formation was observed but no injection occurred (**Figure 4.13** d-e). As the gold nanoparticle surface temperature increased well above the spinodal decomposition temperature, the bubble formation, and particle injection into cell happened at the same time (**Figure 4.13** f-g). This set of results suggested that bubble formation is a necessary condition, but is not sufficient for successful laser injection of a gold nanoparticle into the cell. There are two possible explanations for this: 1) the bubble that is generated at a temperature around spinodal decomposition temperatures is relatively small and the mechanical disruption of the membrane is too weak to create a 'hole'. This is shown in **Figure 4.13**(d); the scattering intensity of the bubble is weaker than that of the bubble in **Figure 4.13**(f), 2) the membrane might already be ruptured by the formation of bubbles. However, a sufficient magnitude of optical force might still be

needed to push the particle inside. This might be another condition for optical injection. As a conclusion, the possible minimum injection laser power needed here is between 3 and 4 mW.

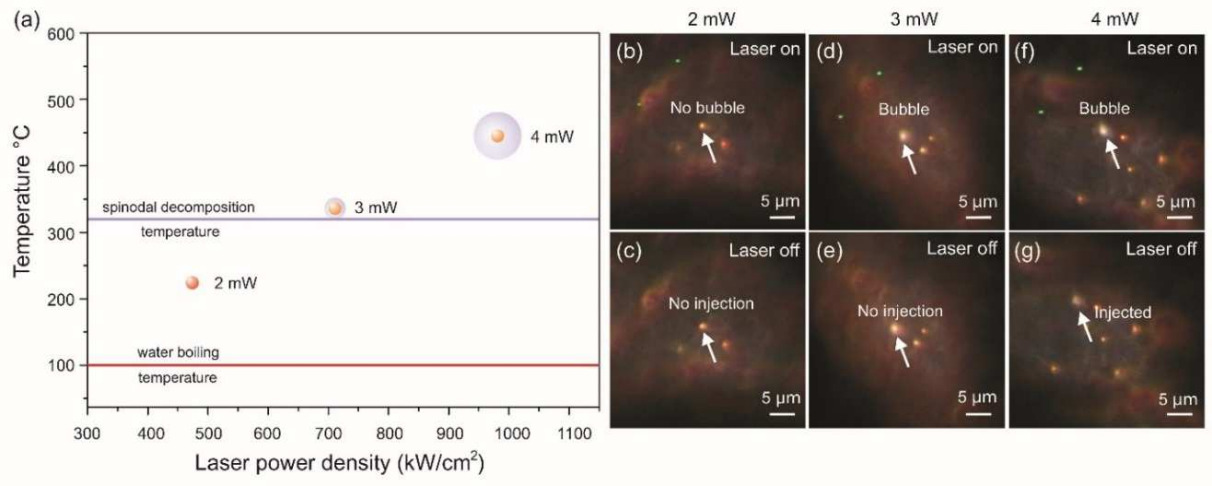

Figure 4.13 | Finding the minimum laser injection condition. (a) Calculated gold nanoparticle temperature at laser powers of 2, 3, and 4 mW. The corresponding dark field images of injection and bubble formation situations at laser powers of (b-c) 2 mW, (d-e) 3 mW, and (f-g) 4 mW.

Single particle spectroscopy was also used to prove the bubble formation by monitoring the intensity changes of the scattering light during the laser injection. For this measurement, the optical injection of a single gold nanoparticle was performed, and the scattering spectra of this particle were recorded throughout the entire process. Each single spectrum was taken for the exposure time of 100 ms (i.e., the running speed of 10 spectra/sec.). The time-resolved intensity spectrum is shown in **Figure 4.14**(a). As a notch filter (532 nm) was placed on the laser beam path before it entered the spectrometer to prevent damage of the CCD camera, there is a low intensity gap between 518 and 535 nm in the spectrum. The on and off state of the laser beam could also be monitored within

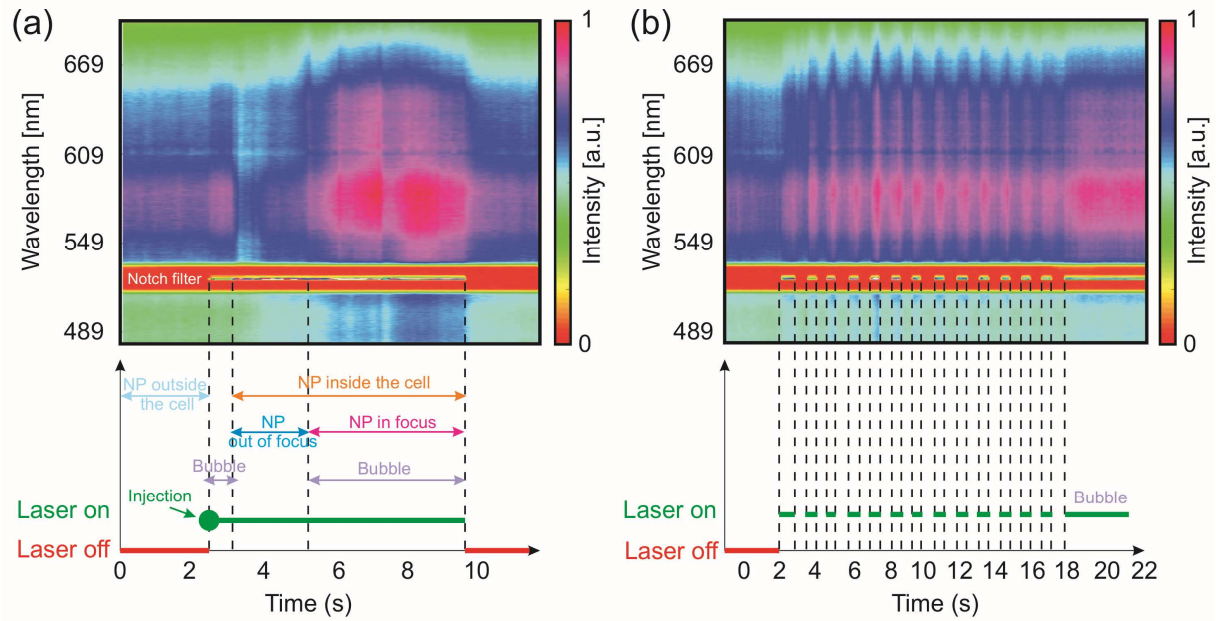

Figure 4.14 | Time-resolved scattering spectroscopy of the bubble around gold nanoparticle under cw laser illumination. (a) A gold nanoparticle on the cell membrane was laser injected into the cell. The injection process was monitored by recording the scattering spectra of the gold nanoparticle. The strong scattering was detected at the time of particle injection, as well as the period during laser heating of the particle, which indicates the bubble formation upon illumination. (b) The gold nanoparticle inside of the cell was illuminated by the laser beam to induce bubble generation. The strong scattering from the bubble was always found once the laser was on, and it disappeared immediately when the laser went off.

this gap. When the laser was switched off, only the gold nanoparticle on the cell membrane showed the strong scattering light between 549 to 609 nm. At around 2.5 seconds, the laser was switched on (5 mW) and focused on the particle. The injection could be seen immediately. Meanwhile, a dramatic light scattering intensity increase was detected on the spectrum, which indicates the formation of bubbles. This strong scattering lasted for approximately half of a second until it began to decrease. Afterward, the particle went out of the focal plane on the cell membrane. This situation was shown as low scattering intensity (as low as the background without particles) periods in the spectra until a clear in-focus image of a particle was found at the lower focal plane. As the particle was in focus again, the bubble was created by the intensive heating, which provided a dramatic increase in light scattering intensity in the spectrum. Once the laser

was switched off again at around 9.6 seconds, the scattering intensity dropped immediately, which means the bubble also collapsed. In the following measurement, the same gold nanoparticle that was injected inside of the cell was irradiated using the focused laser beam with slightly higher laser power (above the bubble generation threshold). As shown in **Figure 4.14**(b), a sudden increase in scattering intensity always occurred when the laser was on, and the scattering intensity dropped immediately when the laser was off. These results, from the spectroscopy view, provide evidence of bubble generation during the laser injection.

The previous discussion illustrates that bubble formation plays a significant role during laser injection. However, one might note that the surface temperature of the individual gold nanoparticles that were irradiated by the injection laser beam, even at the minimum injection condition, is above three hundred degrees, which is likely hazardous to the cells. In this study, it is important to note that the formation of nanobubbles is not only instrumental to the perforation of the membrane, it also aids cell survival. When heating under cw illumination, the heat profile around the gold nanoparticle decays into the surroundings as a function of 1/r. [13] The steam temperature of the nanobubble, however, stays moderate in comparison and the vapor shell provides a shield against further heat transfer into the medium (**Figure 4.15**a). To study the steam temperature in detail, we followed the model by *Fang et al.*.[100] to estimate the steam temperature as a function of the nanobubble size (**Figure 4.15**b). The system is assumed to reach a steady state once the bubble is formed around the gold nanoparticle. The relationship between the nanobubble size and the steam temperature can be estimated using the Clausius-Clapeyron Relation (CCR):

$$C \cdot e^{-\frac{H}{k_B T_s}} = p_0 + 2\gamma \frac{1}{R_B} \tag{4.1}$$

where T_s *(K)* is the temperature of the saturated steam; R_B is the bubble size; $p_0 = 1\ atm$, the atmospheric pressure; γ is the surface tension coefficient, which is a function of the steam temperature $\gamma(T_s) = -0.2222\ T_s + 142.2\ mN/m$; $C = 95\ GPa$, a constant; $k_B = 1.3806488 \times 10^{-23}\ J \cdot K^{-1}$, the Boltzmann constant; and $H = 7.082 \times 10^{-20}\ J$, the enthalpy of water evaporation per water molecule[100]. As shown in **Figure 4.15**(b), a large

bubble has a lower steam temperature than a small bubble, but the total temperature of the steam does not reach temperatures that are higher than 200 °C.

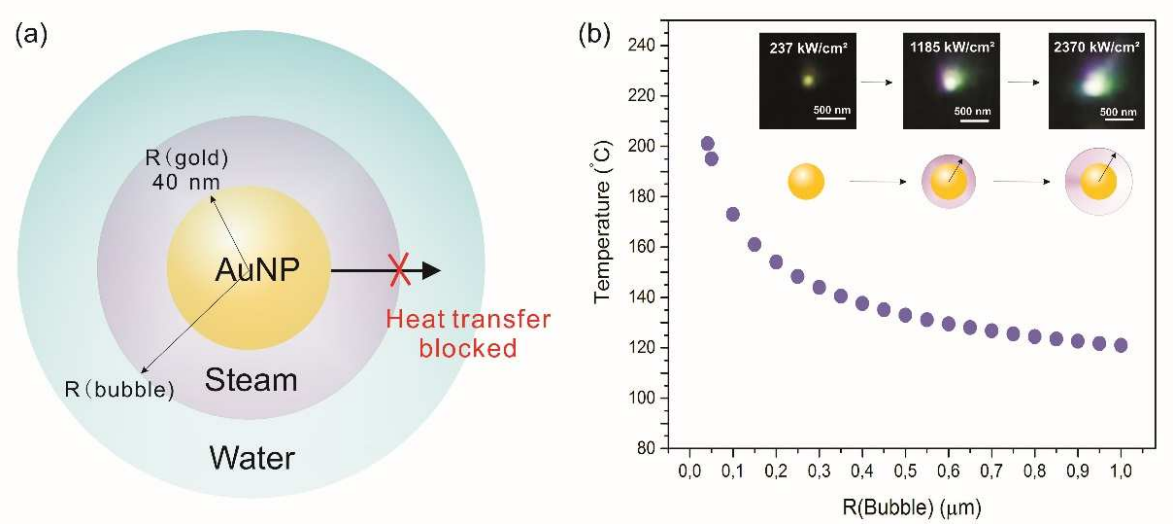

Figure 4.15 | Estimation of the steam temperature inside a nanobubble. (a) The steam shell surrounding the particles works as an insulating barrier that shields the cell from the hyperthermal damage. (b) Calculated steam temperature as a function of the nanobubble size. Figure inset: Examples of nanobubbles formed after exposure of single gold nanoparticle with a focused green laser beam. The bubble size was found to increase with higher laser powers.

In summary, the bubble formation that was caused by plasmonic heating and the optical forces that were exerted on the gold nanoparticle are the two main factors that contribute to the laser injection of a gold nanoparticle into the cell. A schematic illustration of the suggested nanoparticle injection mechanism is shown in **Figure 4.16**. A gold nanoparticle is printed on the cell membrane by a cw laser beam. Then, the particle is heated at the focal point of the same laser beam, which induces an extreme temperature increase on the gold nanoparticle within approximately 1 ps [91, 160]. Once the thermal energy that was delivered to the surrounding medium exceeds the liquid vaporization threshold, an explosive vaporization of a thin layer of fluid that is in contact with the particle occurs. As the initial high vapor pressure overcomes the surface tension of the liquid, a vapor bubble is created that expands rapidly to its maximum size on the nanosecond timescale. It is assumed here that the bubbles do not collapse until the laser

is off as the cw laser illumination can create a steady state after the first bubble is formed. The expansion and collapse of the bubble are accompanied by the production of an acoustic and shock wave that travels outward and interacts with the cell, thereby disrupting the cellular membrane. At this point, the scattering forces that are exerted on the gold nanoparticle push it into the cell through the disrupted 'hole' in the membrane.

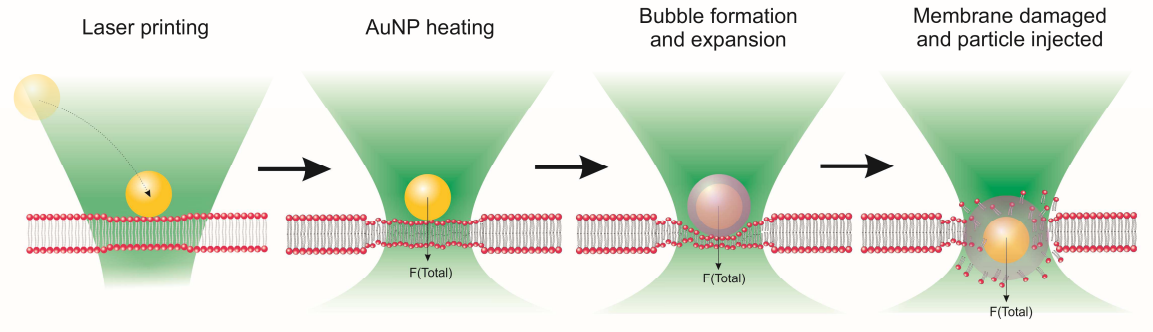

Figure 4.16 | Schematic representation of the laser injection mechanism. Exposure to a gold particle with a focused laser beam leads to a rapid temperature increase and nanobubble formation around the particle. The expansion and collapse of the bubble lead to membrane rupture and the formation of a transient hole. The nanoparticle is then immediately pushed into the cell by the optical force.

4.3 Cell Viability

A successful cellular delivery strategy should show high efficiency and account for the cell viabilities, especially for the purpose of therapy or intracellular sensing in the future. Here we investigated the effect of nanoparticle printing and injection on cell survival, and the experimental method is described in Section 3.2.8. In this work, the cell viability was confirmed by "the enzymatic conversion of non-fluorescent cell-permeant calcein AM to the intensely green fluorescent calcein by ubiquitous intracellular esterase inside of living cells. Dead cells, on the other hand, are identified by the bright, red fluorescence of Ethidium Homodimer-1 (EthD-1), which can enter cells only if the plasma membrane is damaged and becomes fluorescent upon binding to nucleic acids"[161]. As shown in **Figure 4.17**(a) and (c), after the printing step, a cell viability of ~64% was observed when using a

laser power of 5 mW. The viability significantly dropped for higher laser intensities and was only 30% for a laser power of 25 mW. For the injection step (**Figure 4.17**b, d), the application of a 25 mW led to a cell death rate of over 50%, while 10 mW and 5 mW resulted in relatively high viability rates of 73%. Since no printing and injection occurred at 1 mW, all of the tested cells survived at this stage.

Although the surface temperature of the gold nanoparticle that was being injected was beyond the normal biological tolerance, most of the cells were protected from being killed. This can be explained by the 'no-heating' phenomenon which has been reported by other researchers[19]. First, the expanding bubble will scatter part of the incident laser beam, reducing its power density, such that the actual thermal energy accumulated by the nanoparticle is lower than the calculated value. Second, the vapor inside of the bubble creates an insulating effect, preventing most of the heat from transferring from the heated nanoparticle into the environment outside of the bubble. Third, the formation of the bubbles may utilize almost the entire energy released by the AuNP, thus preventing any significant heating of the microenvironment outside bubbles[19]. Therefore, the irradiated gold nanoparticle caused only local damage to the cell membrane, rather than thermal degradation of the whole cell.

The results of the cell viability tests also suggest, in accordance with previous reports by other groups[162], that the hole that was generated in the cell membrane was quickly closed within a few minutes, and that the cell-impermeant EthD-1 dye could therefore not enter the cell shortly after laser injection. The evidence of this conclusion is shown in **Figure 4.17**; no cells showed a green and red fluorescence light simultaneously.

However, the relatively high cell viability that is shown here is the result of injecting only one gold nanoparticle into a cell. Tests performed that injected more than two particles into the same cell led to a dramatic decrease in the overall cell viability. This is the limitation of this laser injection technique. Only one gold nanoparticle can be injected into a cell in order to ensure high cell viability.

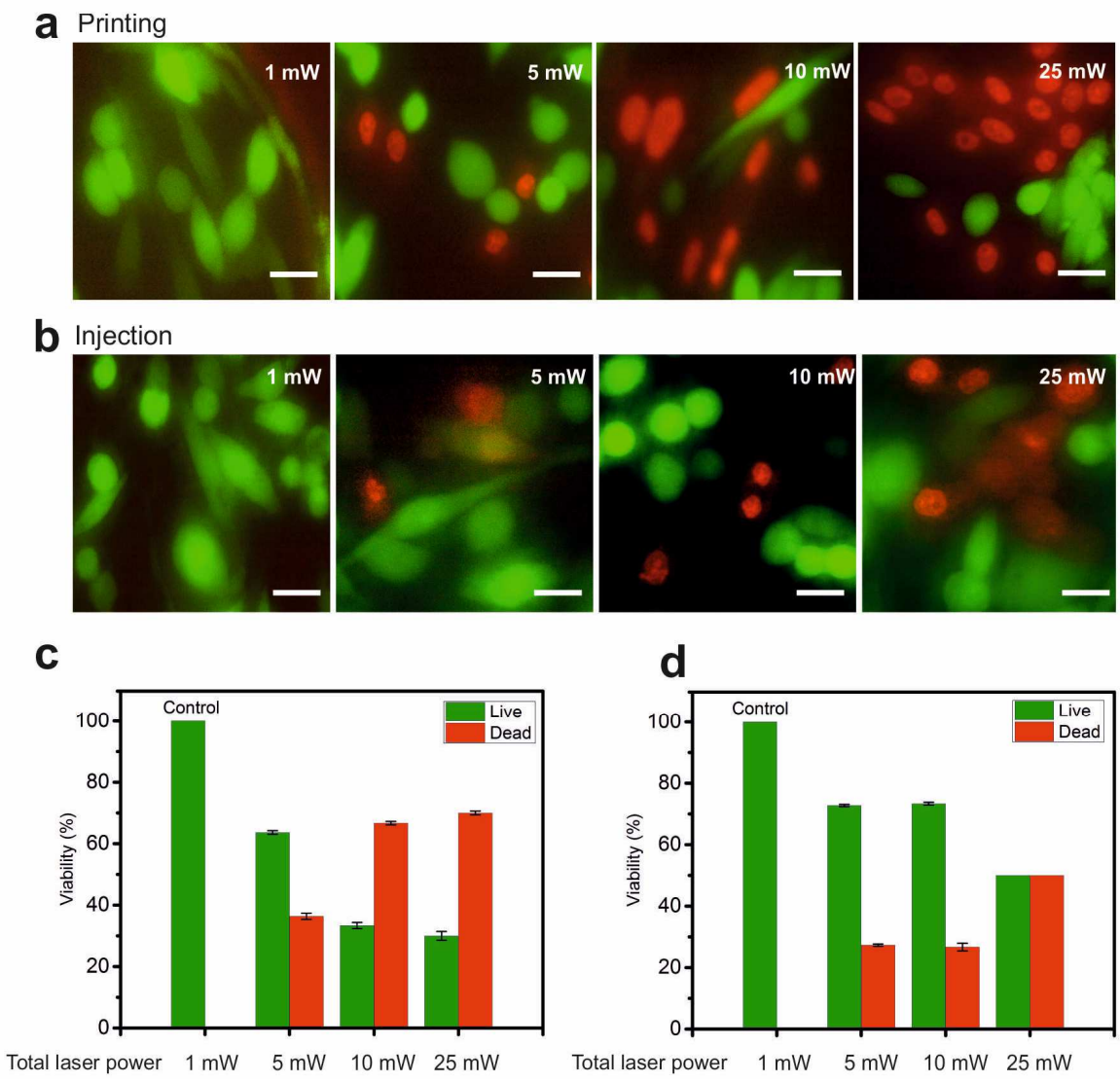

Figure 4.17 | Fluorescence images of stained living and dead cells and cell viability tests. Cell viability was measured after laser printing (a) and injection (b) of gold nanoparticles with different laser powers. Living cells appear green while dead cells appear red in epifluorescence (Scale bar 40 µm). The survival rate of cells after printing (c) and injection (d) were measured independently for both processes. In all cases, the percentages of living cells decreased for higher laser powers.

4.4 Summary and Outlook

In this chapter, several experiments are presented to show a novel optical cellular delivery strategy. First, an all-optical approach to delivering 80 nm gold nanoparticles to the cell surface is demonstrated. In this method, a laser was utilized to print gold nanoparticles onto the cell membrane. This method, compared with many other current cellular delivery approaches being done on bulk cell samples, can be conducted at the single particle and single cell levels. A single gold nanoparticle could be positioned at targeted sites on cell membranes with high precision. One of the main problems is that one must balance between the concentrations of gold nanoparticles in the external solution and the laser power used for printing. If the concentrations were too low, a long waiting time for a printing event occurred, while too high of a laser power would cause thermal damage to the target cell. Therefore, the printing efficiency and cell viability must be taken into account for the purpose of different applications.

Second, we demonstrated that the printed gold nanoparticles on the cell membrane could be injected into the cell using the same laser beam. This method relies on a combination of optical forces and plasmonic heating of single gold nanoparticles with a focused laser beam. The injection process was visualized using dark field illumination, and the injected gold nanoparticle was confirmed by Rayleigh scattering spectroscopy. The surface temperature of the gold nanoparticle and optical forces during injection were also simulated. Importantly, the formation of nanobubbles during injection was instrumental for overcoming the membrane barrier and pushing the particles into the cells, as well as aiding cell survival because of the insulating effect. We showed that the cell survival rate could reach greater than 70% when printing and injecting at a modest laser power.

Overall, the results in this chapter illustrate how nanoscopic objects can be actively delivered one-by-one into a single living cell using light, which offers promising prospects for the development of novel molecule delivery strategies and paves the way for future biomedical applications in nanotheranostics, drug delivery, and intracellular biosensing in more precise manners.

Chapter 5

Gold Nanoparticles Enable Probing fN Forces in Living Cells

With nanotechnology rapidly developing, precise measurement and analysis at the nanoscale level are increasingly required. Gold nanoparticles, because of their unique optical and thermal properties when interacting with light, have been widely used as detectors for sensing nanoscale processes in biological systems[163, 164]. Mechanical forces, as important determinants of cellular forms and functions, are integral to regulating the growth and behavior of living cells[59, 61, 65]. Applying an external force to the cells, and detecting the force and cellular responses to the force, enable a better understanding of cellular mechanics. However, achieving single molecule force spectroscopy is challenging in living cells, particularly under physiological conditions where small deflections of nanoscale objects are overwhelmed by thermal fluctuations. This chapter explains a new concept for locally applying and detecting forces in living cells. First, the basic experimental principle is introduced: how to generate the forces locally outside the cell and how to detect and analyze the force-induced vibrations using the intracellular gold nanoparticles. Then, the principle's capability and reliability are tested through a series of experiments. Afterwards, an analytical way to derive the forces that are applied to the particles is described. The study presented here provides a novel and precise approach to applying and detecting an fN force in living cells at the scale of a single nanoparticle. These findings are expected to enable access to the internal mechanics of living cells in a more elegant and precise way and to pave the way for future studies in cell biology and biophysics.

5.1 Basic Principle

The experiment in this study consists of two parts: a living cell containing the detector gold nanoparticles and a force source in the vicinity of the cell. The detector particles were either optically injected into a cell or endocytosed by the cells before the measurements, while the force source was mimicked by a gold nanoparticle on the glass substrate near the cell. The particle was plasmonically heated by a modulated focused laser beam during the experiment.

As illustrated in **Figure 5.1**(a), the measurement was performed on an upright dark field microscope with a water-immersion objective (100x/NA=0.9) to focus the laser beam (532 nm). An optical chopper with a duty cycle of 50% was placed in the laser beam path to modulate the laser beam in the frequency range of 5-20 Hz. To introduce the signal source at a particular position, a single gold nanoparticle in the solution was printed by an unmodulated cw laser beam on a glass substrate in close vicinity to a cell that contained detector gold nanoparticles. The detector particles can be introduced into the cell by optical injection or through endocytosis pathway. The size of the particle (80 nm) that was used here is larger than the mesh pore size (50 nm) of the cytoskeletons[135]. Thus, the motions of the detector gold nanoparticles were confined by the complex intracellular structures in the cytoplasm. In this case, the magnetic or optical tweezer was not required to trap the gold nanoparticles. In the second step (**Figure 5.1**b), the source particle was irradiated by a chopped focused laser beam, resulting in the instantaneous formation and collapse of bubbles. The periodic expansion and collapse of the bubbles induced the liquid flow, oscillating in time around the heated nanoparticle, and then resulted in the generation of the pressure wave in the surrounding medium[165], sending out a series of force pulses into the liquid. These force pulses apply to the cell and cause non-equilibrium fluctuations of the particle's environment, leading to the vibration of the detector particles inside of the cell. Diffusion analysis and power spectral analysis of the particle traces inside of the cell reveal characteristics about the heterogeneous environment for each detector's location and magnitude of the applied force pulses.

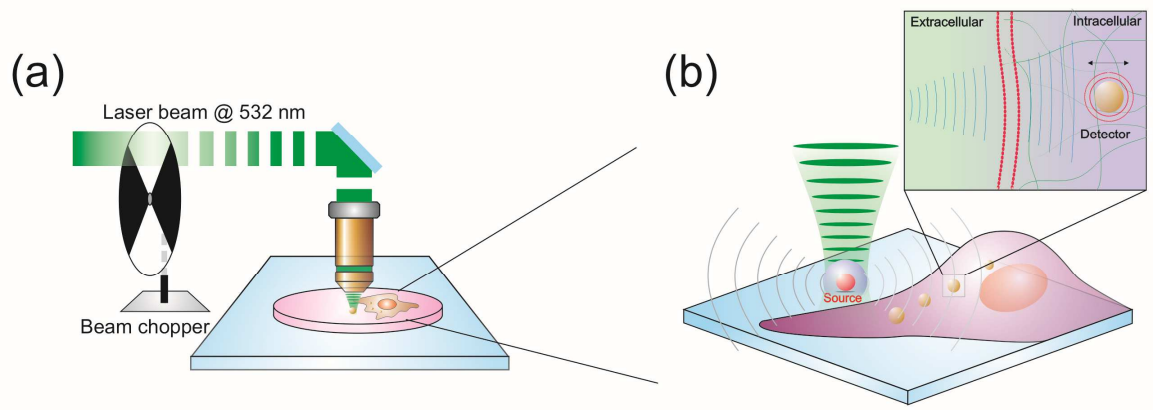

Figure 5.1 | Schematic illustration of the basic principle. (a) A laser is focused on the sample by a water-immersion objective (100 ×). A chopper placed on the beam path is used for modulating the laser beam. (b) The periodic heating of the source particle led to the formation of a cavity bubble and then sent out a series of force pulses into the liquid environment. These force pulses induced the vibration of the detector particle inside the cell. Diffusion analysis and power spectral analysis of particle motion reveals the physical characteristics of the nanodetector environment and the quantity of the applied force.

5.2 Sensing Force-Induced Vibrations inside a Living Cell

To prove the capability of the above-described principle, a series of experiments were performed to probe the force-induced vibrations of detector particles in living cells. In the first part of this section, the laser injection technique that is presented in Chapter 4 was applied to deliver a gold nanoparticle into a cell as an intracellular sensor. Then, Fourier analysis was used to probe the signal of the force-induced vibration with this implanted particle. In addition, the detector particles can be introduced into the cells through the endocytosis pathway. In this case, the influences of source laser powers and the source-detector distances on the detected vibrations over an entire cell were investigated. In the last part of this section, the principle's reliability is confirmed by testing the accuracy and precision of these measurements.

5.2.1 Optically Injecting the AuNP for Intracellular Sensing

Laser injecting the sensor into the cell

To achieve targeted intracellular sensing, the gold nanoparticle sensor was optically injected into a specific position of a living cell using the method that is described in Chapter 4. CHO cells were used as the cell models for measurements. As illustrated in **Figure 5.2**, the gold nanoparticles (80 nm) were added to the cell culture medium and then printed by a 532 nm laser beam at a specific position on the cell membrane. Using the same approach, a single source gold nanoparticle was also laser printed on the glass substrate in the cell's vicinity. After washing away the free diffusing particles in the solution, one of the particles (No. 1) that was printed on the cell membrane was optically injected into the cell by focusing the same laser beam on it. The laser power that was used for injection was set at 5 mW at the laser focal plane, ensuring that the particle was injected through the membrane. As shown in the dark field images in **Figure 5.2**, the gold nanoparticle No.1, compared with particle No.2 and No.3, went out of focus after laser injection and came into focus again when imaging at a lower focal plane. The injection was also approved using the KI/I_2 etching method that is described in Section 3.2.5.

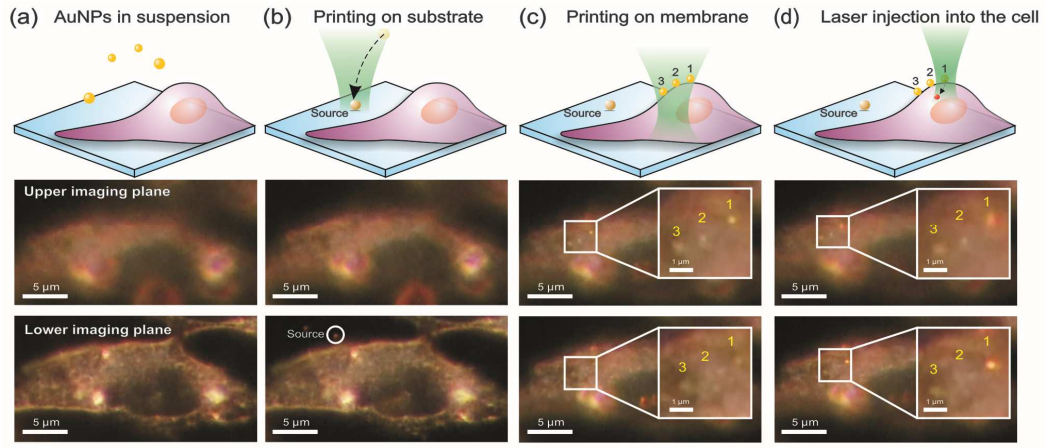

Figure 5.2 | Laser injecting the sensor gold nanoparticle into the living cell. (a) The gold nanoparticles were mixed with the cell culture medium. (b) A single gold nanoparticle was optically printed on the glass substrate as the signal source. (c) The gold nanoparticles (No. 1 to No. 3) were also optically printed on the cell membrane. (d) Nanoparticle No. 1 was injected into the cell by focusing the laser beam on it.

Intracellular sensing with optically injected AuNP

To generate the force pulses outside the cell, the printed source gold nanoparticle was irradiated by the same laser beam with the chopper switched on at the frequency of 13.3 Hz (randomly chosen frequency). As the injected particle was not on the same focal plane as the source particle, which was on the glass substrate, the modulated heating laser beam was defocused on the source particle so the imaging plane could be aligned with the injected particle. Therefore, the laser power that reached the gold nanoparticle is unknown. Here, the total laser power was set at 14 mW to ensure bubble generation around the heated gold nanoparticle. The periodic heating was recorded using a video camera at 50 fps for 15 seconds. The movements of the gold nanoparticles inside the cell were tracked with the particle-tracking software 'Video spot tracker' (freeware provided CISMM: Computer Integrated Systems for Microscopy and Manipulation), yielding the positions (x, y displacement) of each nanoparticle of 750 video frames. The time-displacement $r = \sqrt{x^2 + y^2}$ is the sum of the displacement of x and y directions. To read out the detectors' vibration induced by the force pulses, discrete fast Fourier transformation (FFT) was applied to transform the time-dependent displacement $X(t_j)$ (in either *x* or *y* direction) of each gold nanoparticle into the frequency domain $\mathcal{F}\big(X(t_j)\big)$:

$$\mathcal{F}\big(X(t_j)\big) = \hat{X}\big(f_{k,i}\big) = \sum_{j=0}^{N-1} X(t_j) e^{-i2\pi f_k t_j} \quad (k = 0, \dots N-1) \tag{5.1}$$

where i represents the x or y direction and N is the amount of discrete sample values (*i.e.,* the total amount of frames in the video). In the frequency spectra, the Fourier amplitudes $A\left(\hat{X}(f_k)\right)$ were calculated as:

$$A\left(\hat{X}(f_k)\right) = \sqrt{A(\hat{X}\big(f_{k,x}\big))^2 + A(\hat{X}\big(f_{k,y}\big))^2}\,, \tag{5.2}$$

$$\mathrm{A}(\hat{X}(f_{k,i})) = \frac{2\sqrt{Re(\hat{X}(f_{k,i}))^2 + Im(\hat{X}(f_{k,i}))^2}}{N} \tag{5.3}$$

where $Re(\hat{X}(f_{k,i}))$ and $Im(\hat{X}(f_{k,i}))$ are the real and imaginary parts of the FFT $\hat{X}(f_{k,i})$.

To eliminate the heating laser's direct influence on intracellular nanoparticles, the control experiments were performed to record the same nanoparticles' motions by focusing the laser on a bare substrate area outside the cell.

The result is shown in **Figure 5.3**, the time-displacement spectra were Fourier transformed into a frequency domain using equation (5.1). To increase the signal-to-noise ratio, the Fourier amplitudes were expressed as the sum of both amplitudes in the x and y directions using equations (5.2) and (5.3). When the periodic heating laser focused on the external gold nanoparticle, a clear single peak at the chopper's frequency (13.3 Hz) appeared (**Figure 5.3**a), while in control experiments, the recorded trajectories of the nanoparticles were transformed into flat frequency spectra (**Figure 5.3**b). This result indicates that a gold nanoparticle inside of the cell was able to serve as a nano-detector to pick up the perturbations. The perturbations are generated by the periodic heating of a gold nanoparticle that is located several micrometers away from the cell body.

The experiment that is presented here is meaningful as it combines laser injection and intracellular vibration sensing techniques. The former provides a controllable way of precisely implanting a sensor particle inside a living cell, while the latter allows for the single-particle intracellular sensing of the vibrations. However, the intracellular environment varies at different subcellular locations. Therefore, it is necessary to probe multiple positions in a single cell simultaneously to acquire more comprehensive information of the characteristics of the intracellular environment. However, the laser injection technique that is presented here is limited by low cell viability when injecting multiple particles into one cell. Thus, a more efficient and less harmful approach is needed to introduce multiple gold nanoparticles into a cell in the following studies.

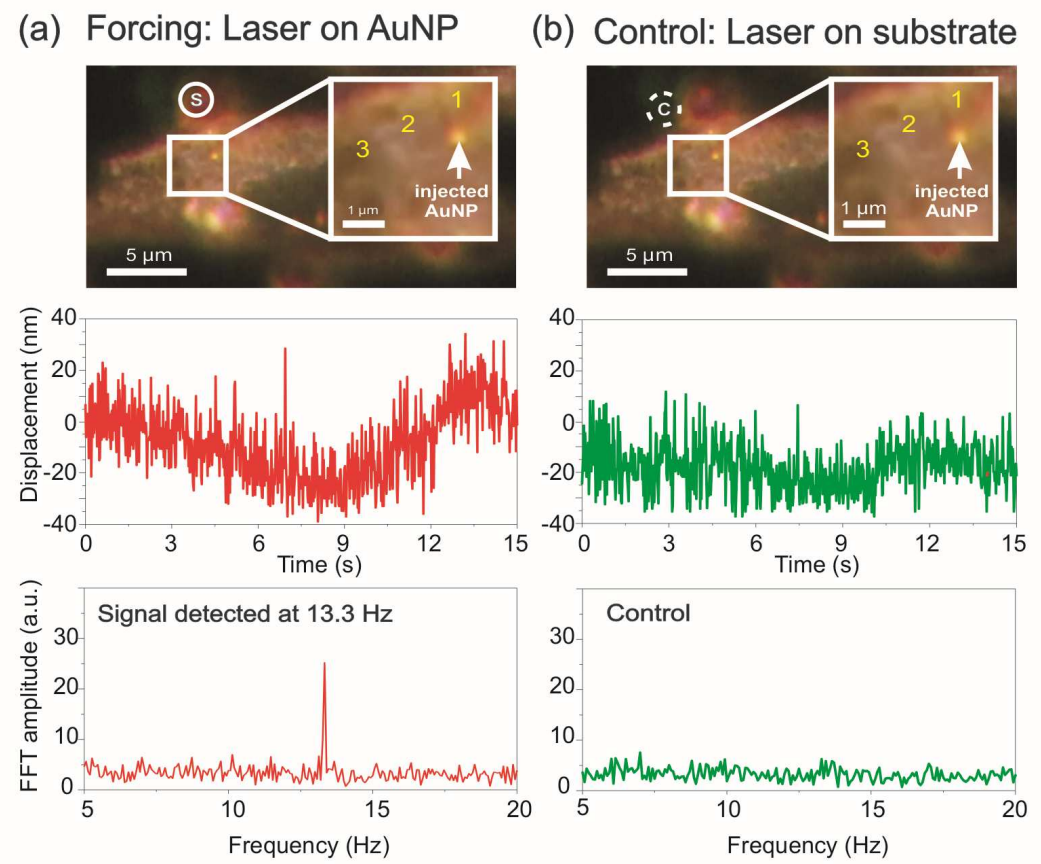

Figure 5.3 | Sensing the vibrations using the optically-injected gold nanoparticle. The dark field image shows the relative positions of the injected detector (white arrows) and the external source particle (white circle). The dashed circle indicates the position of the laser's focus in the control experiment. The time-displacement spectrum of the particle inside of the cell is Fourier transformed into a frequency spectrum. (a) The modulated laser beam is focused on the source gold nanoparticle. The frequency spectrum of the injected detector particle (No. 1) shows a single peak at the frequency of the chopper (13.3 Hz). (b) The control experiment with a laser focused on the bare glass substrate. The detector shows a flat frequency spectrum.

5.2.2 Sensing the Vibrations with Endocytosed AuNPs

As discussed above, laser injecting multiple gold nanoparticles into one cell is limited by decreasing cell viability. Moreover, the injected particle's local environment is not yet clear and the injection process may damage the local intracellular structures where the particle locates. To achieve less harmful multi-position probing in a single cell with intact

structure, the detector gold nanoparticles can be endocytosed by the cells and randomly distributed through the cell body. This is the simplest way of sending extracellular particles into the cells, and it is efficient regarding the multiple-point detection or batch processing of the cells. To do this, positively-charged gold nanoparticles (80 nm) were immersed in the cell medium before measurement. After 24 hours, the particles were endocytosed by the cells (**Figure 5.4**). As introduced in Section 2.2.2, the particles are likely wrapped inside the lipid vesicles after penetrating the membranes. The culture dishes were transferred to the dark-field microscope for measurement. The old medium was discarded, and the cell sample was washed with PBS three times to remove the free nanoparticles.

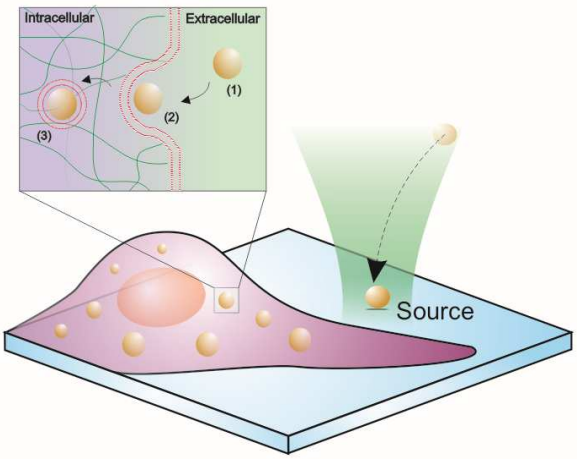

Figure 5.4 | Optically printing a source particle on the glass substrate and introducing the detector particles into the cell by endocytosis. Inset: (1) As detectors, the gold nanoparticles are directly incubated with the cell. (2) The endocytosis path way is the most likely pathway for the cellular uptake of the detectors. (3) The gold nanoparticles that are taken up are contained in the lipid vesicles and trapped in the mesh structures of the cytoskeletons.

Eighty nanometers of fresh gold nanoparticles were then added to the sample. The nanoparticles' surfaces were negatively charged in this case; accordingly, spontaneous binding to the cell membrane was largely reduced. A laser beam (532 nm) was focused on a glass substrate near the cell to print a single gold nanoparticle as the signal source. Afterward, the free gold nanoparticles in the solution were washed away again, and the same laser beam was focused on the printed gold nanoparticle with the chopper switched on at a frequency of 10 Hz. The measured laser power in the objective focal plane was 7 mW, which was enough to generate bubbles around the heated gold nanoparticle. **Figure 5.5**(a) shows the dark field image of the relative position of the source particle and the intracellular detectors. The process of periodic heating was performed as described in Section 5.2.1. As a result, the time-displacement spectra (**Figure 5.5**b) were Fourier transformed into a frequency domain. As **Figure 5.5**(c) displays, the endocytosed gold nanoparticles detected a single peak at the chopper frequency (10 Hz) when the laser

focused on the source gold particle, while the control experiments showed the flat frequency spectra.

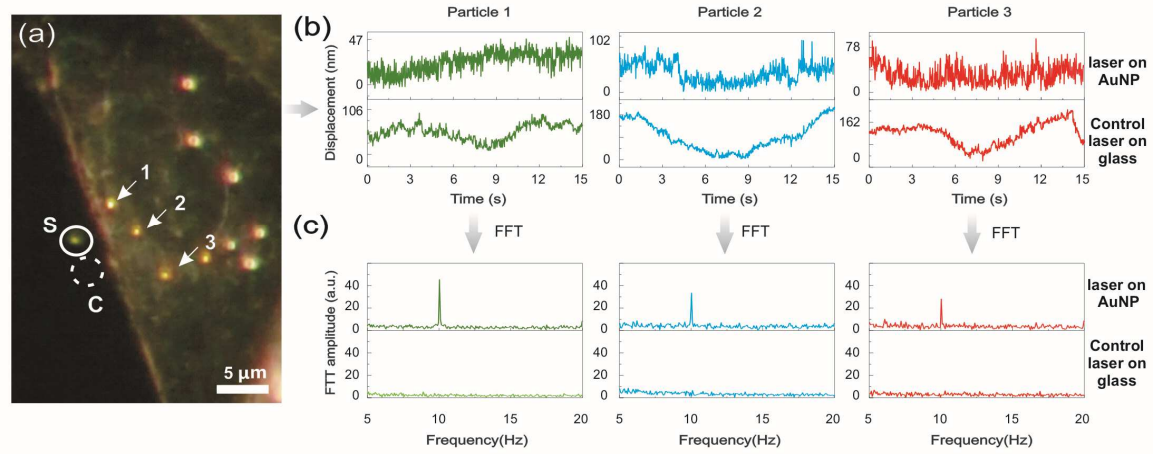

Figure 5.5 | Sensing the Vibrations with endocytosed gold nanoparticles. (a) The dark field image shows the relative positions of the intracellular detectors (white arrows with numbers) and the external source particle (white circle). The dashed circle indicates the laser focus position in the control experiment. (b) The time-displacement spectra of each particle inside of the cell. (c) The frequency spectra of each detector shows a single peak at the frequency of the source, while the control experiments show the flat frequency spectra.

5.2.3 Mapping the Vibrations inside a Single Cell

The section above demonstrates the capability of using the endocytosed gold nanoparticle as the intracellular detector to sense the vibration that was induced by a series of force pulses that were optothermally generated outside of the cell. This facilitates the following studies that map the force-associated vibration signals in a cell. This section explores the effects of laser powers on detector particle vibration by mapping the signal strength that is detected inside of a single cell. To do this, the detector gold nanoparticles were

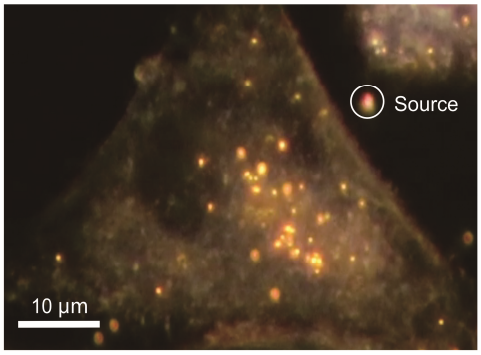

Figure 5.6 | The dark field image showing the relative positions of the detector particles and source particle.

endocytosed by the cells as described above. A single source gold nanoparticle was optically printed beside a cell containing the detector particles (**Figure 5.6**). The shortest distance between the source particle and the cell membrane is about 5 µm. A modulated laser beam was focused on the source particle. The modulation frequency was set at 13.3 Hz. The process of applying force was recorded by a digital camera for 120 seconds. Afterward, the Fourier analysis of the time-displacement of the detector particles resulted in the frequency spectra of each particle.

To identify whether the peaks at the frequency of the chopper (13.3 Hz) in the frequency spectra were signals or noises, the values of FFT amplitude $A(F_{j,i})$ for each individual detector were extracted. Here, $j \in (11.3\ \mathrm{Hz},\ 15.3\ \mathrm{Hz})$ is the frequency and i represents the x or y direction. The sum of the amplitude is represented as $(F_j) = \sqrt{A(F_{j,x})^2 + A(F_{j,y})^2}$. The noise level $A(N) \pm \sigma$ is obtained by averaging all of the $A(F_{j,i})$, except for the value at $j = 13.3$ Hz where σ is the standard deviation. If $A(F_{j,i}) - 3\sigma \leq 0, (j = 13.3\ \mathrm{Hz})$, the detected peak at the frequency of the chopper, is defined as a noise and the value of the effective signal is defined as $A(ES) \stackrel{\text{def}}{=} 0$; if $A(F_{j,i}) - 3\sigma > 0, (j = 13.3\ \mathrm{Hz})$, the detected peak at the frequency of source is defined as a signal. Accordingly, we have the value of the effective signal $A(ES) = A(F_{j,i}) - A(N), (j = 13.3\ \mathrm{Hz})$. To map the strength of the signal detected on all of the particles in a single cell, the mean noise level $A(MN)$ is calculated by averaging all of the values of $A(N)$ that were obtained on every tracked particle. $A(MN)$ is also defined as the threshold of the signal and the noise. Any value of the peak at 13.3 Hz, which is larger than $A(MN)$, is defined as a real signal. Therefore, the value of the real signal is expressed as $A(RS) = A(ES) + A(MN)$.

We extracted the two-dimensional positions of each particle and their values of the real signals $A(RS)$ at the chopper frequency (13.3 Hz), and plotted them as color maps (**Figure 5.7**). The circle's size is proportional to the real signal strength of the detector vibrations. The signal strengths' values are represented using the color scale bar. These values were normalized using the maximum values of the detected real signal. **Figure 5.7**(a) shows the situation when the power of the modulating laser was set at 7.3 mW. The detector particles showing the flat frequency spectra are marked as black spots on the color maps.

Notably, not all of the detector particles were equally affected by the input pulse. Particles that were sitting closer to the source showed a stronger response, while particles that were located further away from the source displayed a smaller signal. This may be because of the attenuation of the oscillation during the propagation inside of the cell. **Figure 5.7**(b) shows the color map when the chopped laser power was elevated to 12.7 mW. The overall signal strength for all of the detector particles increased accordingly. Most of the detectors are driven to vibrate, although their values still vary depending on the distances between the detector particles and the source. This result also proves that the pressure pulse does not shake or move the complete cell as the signal strength would be equal for all of the particles in this case.

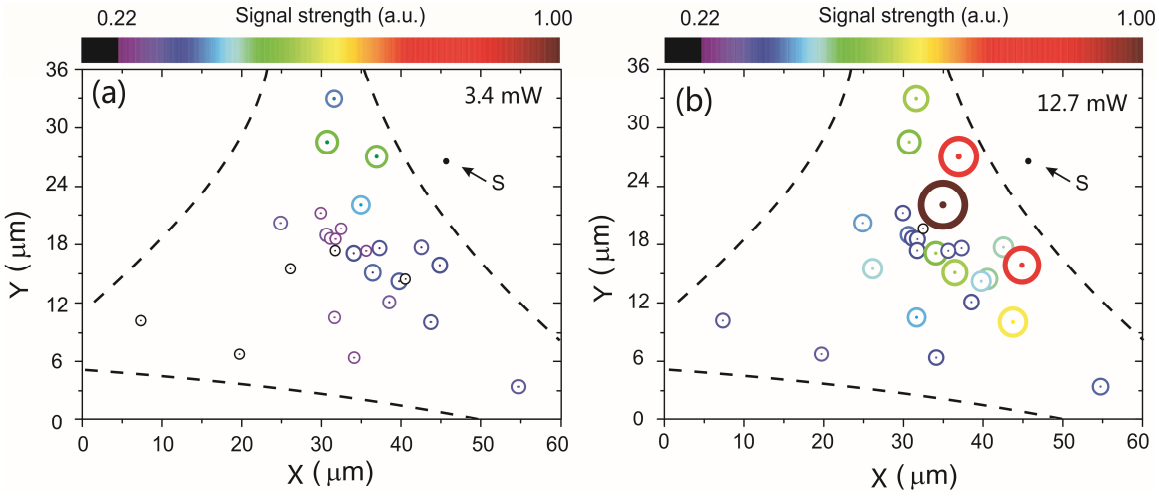

Figure 5.7 | Maps of the signal strength of the detector particles inside a single cell. The centers of each colored circle overlay the dark field images of the detector particles. The scale of the colored circles is proportional to the signal strength that is detected at the frequency of the chopper. The normalized values of the signal strength are indicated using the color scale bar. The signal strength of 0.22 is the calculated threshold of the signal and noise. The detector particles with this signal strength are regarded as 'no signal detected' and are marked in black. (a) Modulating at the laser power of 12.7 mW; (b) Modulating at the laser power of 7.3 mW.

5.2.4 Distance Dependency

The previous section shows that the vibration strength of the detectors presented a laser power-dependent manner. Overall, detectors that are closer to the source have stronger responses to the oscillation. However, the source-detector distance depends on the detectors' positions, as the source particle is fixed at one site, while the detector particles are randomly distributed inside of the cell. To precisely control the source-detector distance, this section describes the positioning of the source particle away from the cell at different distances and the testing of how far the generated force pulses can travel through the medium and drive the intracellular detectors' vibration.

First, the detector particles (80 nm) were endocytosed as described above. Source particles were then added to the medium. At a chosen position that was far enough from the cell but still within the vision of the microscope image, a source gold nanoparticle was optically printed on the substrate. Afterward, the free gold nanoparticles in the solution were washed away. A modulated laser beam (chopping frequency = 13.3 Hz) was focused on the source particle with a power of 7 mW at the focal plane. The video camera recorded the periodical heating for 15 seconds. The fresh detector particles were added again and optically printed on the next position that was closer to the cell. The same measurement was repeated. As shown in **Figure 5.8**(a), S1, S2, S3, and S4 indicate positions where the source particles were printed. The motion of three detector particles (1, 2, and 3 as indicated in the dark field image) was analyzed as described in previous sections. The effective signal values $A(ES)$ at 13.3 Hz for each particle at each source-detector distance were plotted in a bar chart in **Figure 5.8** (b). The three detector particles show a clear distance-dependent trend. At 41.6 - 44.7 µm of source-detector distance, the intracellular particles could not sense the vibration. As the distance decreased to 35.2 µm, the detected vibration became clear. The results presented in this experiment show that the signal strength is controllable by varying the source-detector distances. The results also indicate important information that the force pulses can be generated from 10 µm to at least 35 µm away from a cell and a signal can still be observed, even if the source nanoparticle is located more than 33 µm away from the cell itself. As the temperature at the center of the source particle can reach hundreds of degrees Celsius

during laser heating but will dissipate within a few hundred nanometers, measuring within this distance range also protects the cell from possible thermal damage, supporting future applications of this approach in living cells.

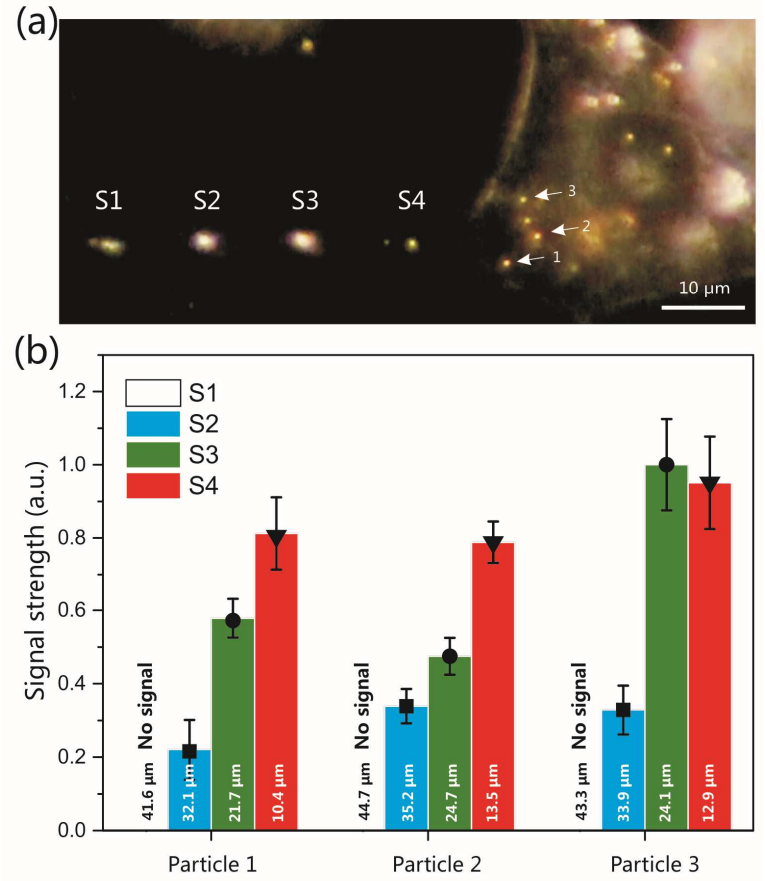

Figure 5.8 | The distance dependency measurement. (a) The dark field image showing the relative positions of the source particles and the intracellular detectors. S1-S4 indicate the positions where the source particles were optically printed. The arrows with 1, 2, and 3 indicate three of the detector particles inside the cell. (b) The signal strength of each detector particle measured at four source-detector distances. At position S1, no signals were detected inside of the cell. Therefore, the signal strength is zero in the bar chart. The source-detector distances were obtained from the first frame of the video. The error bars represent the three times standard deviation of the noise level for each measurement. This value indicates the fluctuation range of the noise level in each measurement and is the criteria for determining the signal and noise as described in Section 5.2.3

5.2.5 Accuracy and Precision of the Detectors

To ensure the explored intracellular sensing method is not specific to the chosen frequency of the source, namely 13.3 Hz or 10 Hz as described in the above measurements, we performed a set of intracellular sensing tests. In these experiments, the chopper frequency for the heating laser was varied at 4.2, 7.3, 13.3, 17.7, and 23.3 Hz. The values of these frequencies were randomly chosen under the requirements of the Nyquist-Shannon sampling theorem[166] (*i.e.,* the heating laser modulation frequencies are kept below the sampling rate/2 = 25 Hz). The motions of four gold nanoparticles inside of a cell (**Figure 5.9**a) were recorded at each heating frequency. As a result, the Fourier analysis of the four gold nanoparticles' displacement revealed that the peak positions closely followed the heating frequency outside of cell (**Figure 5.9**b).

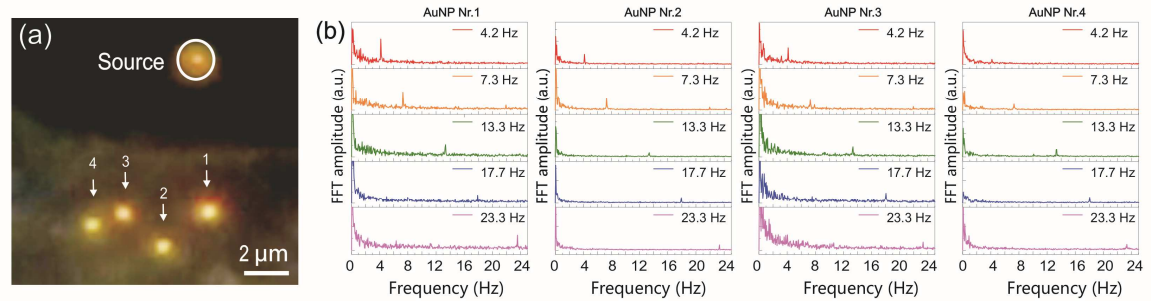

Figure 5.9 | The accuracy and precision measurements of the detectors towards the source. (a) The relative positions of the intracellular detectors and external source particle. (b) The frequency spectra of the detectors with heating laser focused on the source particle at frequencies of 4.2, 7.3, 13.3, 17.7, and 23.3 Hz.

To prove this measurement's reliability, estimations of the detectors' accuracy and precision towards the source were performed, respectively. The accuracy was obtained by calculating the relative error between the true values (i.e., the chopper frequency) and the measured frequency's mean values at four particles (**Figure 5.10**a). As a result, the accuracy of this measurement was kept above 99.50 %. The precision was obtained by calculating the frequencies' standard deviation (SD), which were measured at four particles. As presented in **Figure 5.10**(b), at each chopper frequency, the measurements showed narrow distributions, which means each measurement has a high precision.

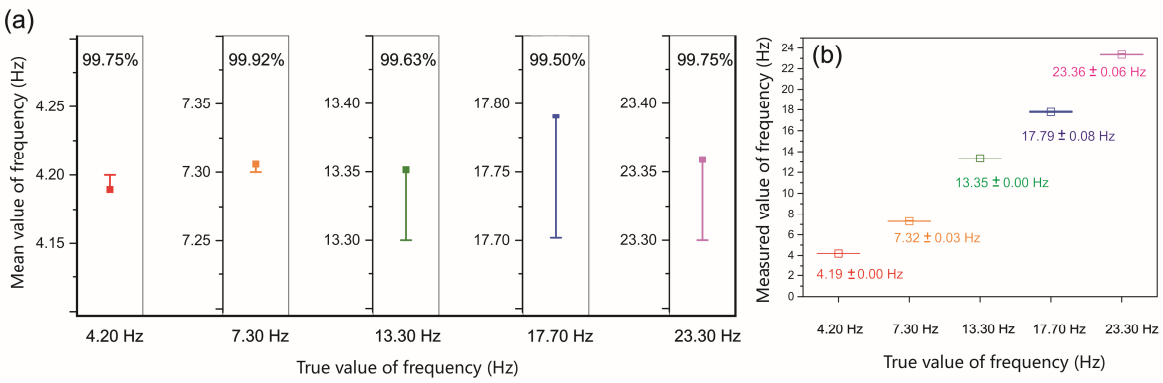

Figure 5.10 | The accuracy and precision measurements of the detectors towards the source. (a) The accuracy analysis of the detectors. The error bars indicate the absolute errors between the true values and the measured mean values. The percentage values indicate the detectors' accuracy at each frequency. (b) The detectors' precision, which was measured at each frequency, is written as mean ± SD.

5.3 Force Spectroscopy inside Living Cells

The previous sections demonstrate that gold nanoparticles inside living cells can serve as sensors to optically readout vibrations that are generated in the vicinity of the cell. These vibrations result from force pulses applied to intracellular gold nanoparticles. In the next step, an approach is investigated to derive the force values that are applied to the detectors from the signal strength.

Diffusion analysis

As the detector particles are surrounded by the complex intracellular environment, it is important to characterize their diffusion properties during the force application. The analysis was performed on the cell as described in **Figure 5.10** and the laser power for heating was 12.7 mW. In this measurement, the two dimensional trajectories of twenty-seven single gold nanoparticles during the experiment of force application were tracked for two minutes. Detector particles in three subcellular areas were selected as examples for further analysis (**Figure 5.11**a). The resulting trajectories are described by the mean

square displacement (MSD) $< \Delta r^2(\tau) >$ of a particle within a given time delay (τ), where $\Delta r(\tau) = r(t+\tau) - r(t)$. **Figure 5.11**(b) shows the log-log plot of $< \Delta r^2(\tau) > \sim \tau$ for the twenty-seven particles inside one cell for 120 seconds. By averaging the $< \Delta r^2(\tau) >$ values of the single traces at each time delay, the average MSD for this period was obtained. The cytoplasm is not a simple viscous liquid but a viscoelastic environment[134]. Thus, according to the introduction in Section 2.3, a particle's diffusion in an inhomogeneous complex liquid is characterized by the time-dependent power law[127, 134]:

$$< \Delta r^2(\tau) > = C\tau^{\alpha} \quad (5.4),$$

where *C* is a constant that is related to the diffusion of the particle, and α is the parameter that determines the types of particle diffusion. Taking the logarithm of equation (5.4) yields:

$$log < \Delta r^2(\tau) > = \alpha log(\tau) + log\, C \quad (5.5),$$

where the power term and constant term correspond to the slop and intercept of a straight lines in a log-log graph. **Figure 5.11**(c) shows the log-log fit of the *MSD-*τ plot according to the time-dependent power law in shorter time delays ($\tau \leq 0.2\ s$). The reason to plot within 0.2 s is that the molecular motor-induced random fluctuation might happen in longer timescales, in which the MSD increased approximately linearly with time[135]. The upper limit of the short timescale 0.2 s also corresponds to the lower limit of the frequency range 5 Hz that was used in this measurement. The average MSD of twenty-seven particles and the MSD of the three example particles were investigated. The obtained α values, which are all between 0 and 1, illustrate that the motion of the intracellular particles show subdiffusion[134], indeed.

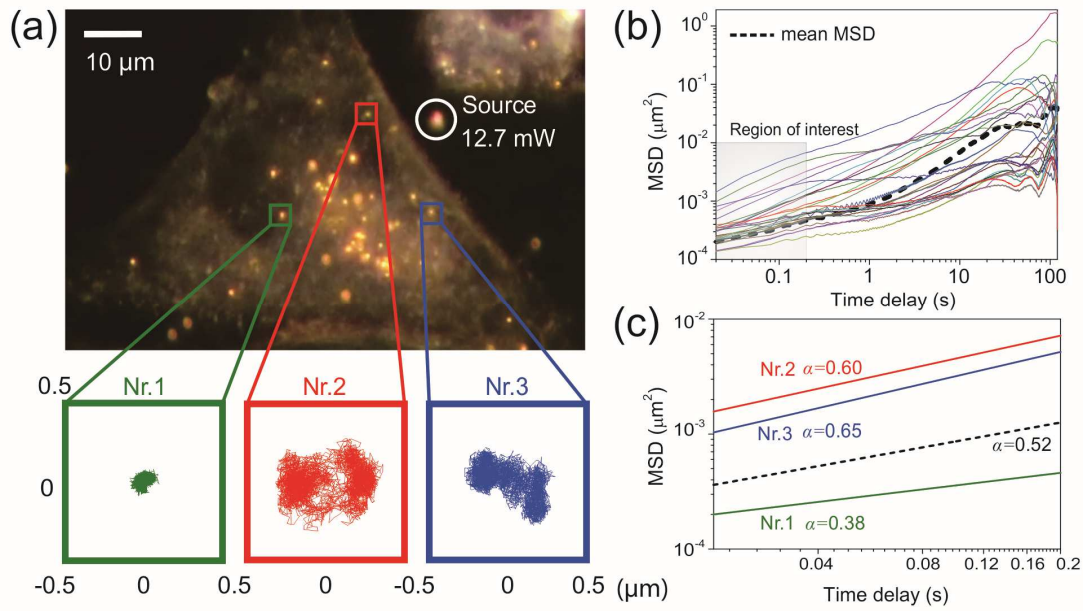

Figure 5.11 | Analysis of particles diffusion inside of the cell. (a) Dark field image shows the gold nanoparticles inside of a cell during an experiment. The 2D trace of three example gold nanoparticles in different subcellular areas is shown. The side length of the colored boxes is 1 µm. (b) Mean square displacement (MSD) analysis of all 27 particles tracked during this experiment. The dashed black line is the average MSD of all 27 particles. (c) A fit in the low time delay regime ($\tau \leq 0.2s$) reveals subdiffusive behavior. The corresponding trends indicating the power law by the exponent α are given in the plot.

Converting Fourier peaks to forces *

In the second step, I will discuss the possibility of deriving the forces that are applied to the detector from the force-associated signal strength. A particle's motion inside the cell can be described by the generalized Langevin equation[167, 168]

$$m\ddot{x} = F_{v-el}(t) + F_R(t) \qquad (5.6),$$

where m denotes the mass of a gold nanoparticle; x is the displacement of a particle; and $F_{v-el}(t)$ represents the viscoelastic forces acting on the particle. $F_R(t)$ represents the random forces that act on the particle; it includes the contribution from both direct forces between the particles and the stochastic Brownian forces[168]. To start with a simple

* The theoretical derivations are contributed by Carla Zensen, my colleague PhD student.

model in this study, we made an assumption that only the viscous part of the cytoplasm was taken into account in our model. In this case, equation (5.6) can be specified as the classical Langevin equation[169, 170]:

$$m\ddot{x} = -\gamma\dot{x} + \xi(t) + F_s(t) \tag{5.7},$$

where γ is the viscous friction coefficient; $\xi(t)$ is the thermal random force, and $F_s(t)$ is the external force applied to the detectors, which is assumed to be proportional to the laser power and is a repeated step function

$$F_s(t) = F_s \sum_{k=0}^{N-1} h(t - kt_{osc}),$$
$$h(t) = H(t) - H(t - t_{osc}/2) \tag{5.8}$$

where $H(t)$ is the Heaviside step function and $t_{osc} = 1/f_0$ is the chopper period with f_0 being the chopper frequency. According to the derivation that is presented in **Appendix C,** the solution for equation (5.6) in Fourier space is given by:

$$\hat{x}(f) = \frac{\hat{\xi}(f) + \hat{F}_s(f)}{i2\pi\gamma f - (2\pi)^2 f^2 m}. \tag{5.9}$$

Equation (5.9) can be further solved using the definition of the power spectral density (for details see **Appendix C**), which finally leads to

$$\langle S_x(f)\rangle = \frac{\langle\hat{\xi}(f)^2\rangle}{t_{msr}(2\pi\gamma f)^2} + \frac{{F_s}^2}{2\gamma^2 t_{msr}(2\pi f)^4} \cdot \left[\frac{\sin(\pi f t_{msr})}{\cos(\frac{\pi}{2} f t_{osc})}\right]^2 \tag{5.10}$$

where $\langle S_x(f)\rangle$ is an expression for the signal strength that is detected in the power spectrum and t_{msr} is the total measurement period. Equation (5.10) builds a connection between the power spectral density and force; it enables the conversion from the

detected vibration signals to the force that is applied to the detector particles. While the first term in equation (5.10) refers to the characteristic spectrum of Brownian noise, the second term results from the external periodic force with frequency f_0. The measured spectra (i.e. refer to an example spectrum below) show that at the chopper frequency f_0, the measured peak is significantly higher than the noise level. Thus, to estimate an order of magnitude of the forces measured in this approach, the contribution of the first term in equation (5.10) is neglected. With this, the force acting on a gold nanoparticle can be approximated as

$$F_s(f_0) \approx (2\pi f_0)^2 \gamma \sqrt{2 S_x(f_0) t_{msr}} \cdot \lim_{f \to f_0} \frac{\cos(\frac{\pi}{2} f t_{osc})}{\sin(\pi f t_{msr})}. \tag{5.11}$$

Provided only the viscous drag is considered in the cytoplasm, $\gamma = 6\pi a\eta$ can be used[132, 171], where a is the radius of the spherical particle and η is the local viscosity around the particle. **Figure 5.12** shows the power spectra of the three example particles that were located in different subcellular areas. Their peak values $S_x(f_0)$ at the chopper frequency $f_0 = 13.3\,Hz$ were found. To estimate the force ranges that were applied to the intracellular particles, the local viscosity in the aqueous phase of the cytoplasm ranging from 1 to 140 centipoise (cP)[172, 173] is used. Thus, the forces acting on the detectors during the measurement period $t_{msr} = 120\,s$ can be calculated using equation (5.11). The estimated force ranges are shown in **Figure 5.12** and their values are within fN ranges in low viscous environment.

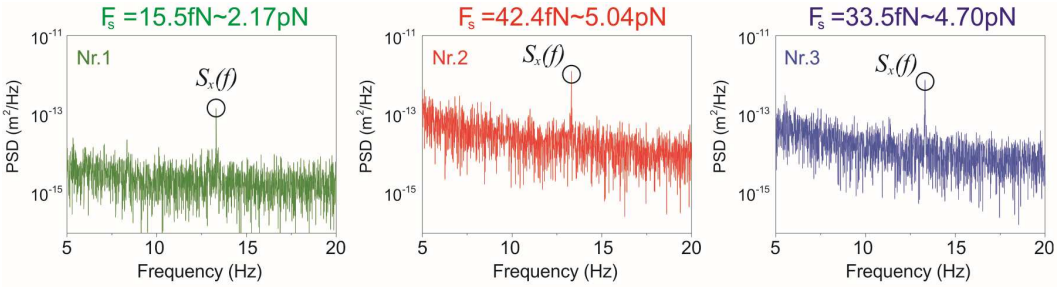

Figure 5.12 | Conversion of Fourier peaks to force. Power spectral density (PSD) plots for the three example particles located in different subcellular areas. The liquid-phase intracellular viscosity is estimated between 1 and 140 cP[172, 173]. The resulting force ranges are given.

This result illustrates how low-frequency vibration spectra in the Fourier space can be analytically converted into a force. The method presented here presents a new way of applying a gentle mechanical force to a living cell, and a simple analytical model for probing this force inside the cell with the sensitivity of fN ranges.

However, the introduced model only considers the effect of the fluid-phase cytoplasmic viscosity. This limitation neglects the influence of the cytoskeleton elasticity on the particles' motion. Indeed, if the size of the nanoparticles (80 nm) is larger than the mesh pore size of the cytoskeleton (typically 50 nm) [127], the particles' motion inside the cytoplasm is confined. In this case, the viscoelastic rheological behavior, in which the energy of particle diffusion is partially stored and dissipated within the complex cytoplasmic environment[174], must be considered. Further, the model that is presented here neglects the noise term in equation (5.10), as the aim of the present model is to give an estimation of the force range, rather than an exact force value.

Despite this, a more thoughtful model is needed in the future to derivate a more exact force value. The generalized Langevin equation provides a justified model to describe the motion of small particle that is dispersed in viscoelastic media[167, 168]. As already shown in equation (5.6), the viscoelastic forces $F_{v-el}(t)$ include viscous damping of the liquid phase, and incorporates a generalized time-dependent memory function $\eta(t)$ that takes elasticity into account as it determines how past movements contribute to the present dissipative force[168, 175]. As illustrated by the current result, building a connection between the force and the vibration signal is achievable by using the simple model; thus, it is reasonable and necessary to take a step further in the future by using a more precise model to derive the forces. Therefore, solving the generalized Langevin equation by considering both viscosity and elasticity is an option for building a more precise model to convert the vibration signals to forces in the near future, thereby acquiring a more precise measurement of the force spectroscopy inside the living cells.

5.4 Summary and Outlook

This chapter presents a new concept for applying and investigating forces in biological samples elegantly and non-invasively. We designed an experiment where small nanoparticles, which are either optically injected into a cell or endocytosed by the cell, serve as detectors by probing local perturbations within the cytoplasm. The perturbations are generated by periodically heating gold particles that are located several micrometers away from the cell body. Irradiating the particles with a chopped laser beam leads to cavity bubbles instantaneously forming and collapsing. The resulting force pulses cause non-equilibrium fluctuations to the detector particles' movement inside the cell. Diffusion analysis and power spectral analysis of the particle traces reveals not only characteristics about the heterogeneous environment for each detector location, but also the magnitude of the applied force pulse. The results suggested the possibility of precise and sensitive intracellular force sensing using gold nanoparticles either at desired positions or throughout the cell.

This new approach that is provided is more sensitive than standard tools of the trade and avoids several shortcomings of conventional methods, such as atomic force microscopy and optical tweezers. This is because it does not require mechanical contact or direct laser illumination of the analyzed sample, which could lead to photodamage or localized heating. The analysis can be done at one targeted position or at multiple positions simultaneously. However, the limitation of this approach still exists that the mathematical model for deriving the values of the forces does not consider the influence of the cytoskeleton's elasticity on the particles' motion. A more complex model that takes into account the cytoplasmic viscoelasticity is needed to achieve a more precise measurement of the force values in *vivo*.

Overall, this approach renders it possible to perform localized force mapping of living cells in the fN resolution, which offers a broad applicability for investigating the heterogeneous nature of intracellular processes.

Chapter 6

Conclusion and Outlook

This thesis presents the research that was conducted on AuNP-cell interactions under the manipulation of the laser beam. The main motivation was to use the plasmonic properties of the gold nanoparticles to explore their new biomedical and cell biological applications. First, we successfully used light to deliver the gold nanoparticles to the membrane of the mammalian cells and then injected the gold nanoparticles one-by-one through the membrane using a focused resonance laser beam. Afterward, we developed a way to use gold nanoparticles to locally apply and detect fN forces in living cells. The gold particles serving as sensors can either be optically injected for precise on-site detection or be endocytosed by the cell for multiple-location signals mapping.

In the first part of the experiments in this thesis, the gold nanoparticles with diameters of 80 nm could be printed on the cell membranes, only by shining a laser beam on the cell. The printing was fully controllable, and delivering one particle at one time to the targeted position on the single cell was possible by balancing the laser power and the concentrations of the gold nanoparticles in the solution. This is useful for the labeling of the cell membrane, particularly at the single particle and single cell levels. One can consider using this technique to study or control the membrane functions, for example, to investigate how a single nanoparticle interacts with membrane proteins, or how the particle affects the functions of these proteins. In the second step of this experiment, the gold nanoparticles on the cell membrane were injected into the cell using a focused resonance laser beam. The key feature of this method is the combination of bubble formation around the gold nanoparticle upon local plasmonic heating to open a ‘door’ on the membrane and the optical forces to ‘push’ the particle. To my knowledge, this is the first time that these two effects have been combined for this purpose. As delivering drugs, genes, and other substances into cells is a critical technique for medicine, cell biology, and

biotechnology, one can consider, in the future, using this technique to inject small molecules into cells using nanoparticles, including gold spheres as well as more complex structures, as a 'ferry.' In this case, the wavelength of the injection laser can also be tuned close to the plasmonic resonance frequency of the 'ferry' structure, for example, in the near-infrared region, which will be more compatible in biological samples. In addition, if this laser printing and injection technique could be scaled to situations outside of a microscope, it has the potential to become a standard tool in the biochemical modification of cells.

In the second part of the experiments in this thesis, the gold nanoparticles played dual roles: as an extracellular signal source to optothermally generate a series of force pulses that are applied to the cell, and as the intracellular biosensors to pick up the vibrations that are induced by the force pulses at the scale of a single molecule. By analyzing the motions of the intracellular detector particles with power spectra, the fN forces that were applied to the intracellular particles can be estimated, which is the key to studying the dynamic cellular mechanics. Although the force spectroscopy of biomolecules has been achieved using AFM, magnetic tweezers, and optical tweezers, the concept that is introduced in this thesis provides a new approach to applying a local force to the living cell in an elegant way and probing this force in a simple, efficient, and safe manner. This measurement suggests the future possibility to resolve an fN force at a targeted position inside of a living cell using a single nanoparticle or map the magnitudes and directions of the external forces propagating throughout the entire cell body.

In summary, many of the important optical and thermophysical properties of gold nanoparticles have been discussed and applied to conduct the research in this thesis. It is suggested that a laser that is delivering nano-objects into a living cell and single particle force spectroscopy in *vivo* are within reach, though challenges still exist and more studies are still required. However, it is becoming increasingly possible to control and read biological information at the cellular and molecular levels by simply switching on the laser.

Appendix

Calculations

(A) Temperature Distribution around Gold Nanoparticles

Estimation of laser beam size

To simulate the temperature distribution around gold nanoparticles under cw laser irradiation, the laser beam size must be estimated. The laser beam that was used in this work follows the Gaussian distribution, and its transverse electric field and intensity distributions are well approximated by the Gaussian function, which in 2-dimensional coordinates, can be written as:

$$f(x,y) = Ae^{-\frac{x^2+y^2}{2\sigma^2}} \quad \text{(A 1)}$$

where A is the intensity and σ is a constant that is connected to the beam size.

The beam diameter or beam width is the diameter along any specified line that is perpendicular to the beam axis and intersects it. The definition of beam diameter used here is full width at half maximum (FWHM), which indicates the width of the Gaussian curve that is measured between those points on the y-axis, which are half of the maximum amplitude. This value is related to the σ value in the Gaussian function according to:

$$FWHM = 2\sqrt{2ln2}\,\sigma \quad \text{(A 2)}$$

To measure the FWHM experimentally in this work, a reflection image of the laser beam that was focused on the glass substrate was captured by the digital camera under the dark field microscope (**Figure A1a**). Then, the image was analyzed with the software Gwyddion 2.31 (free to use). The intensity distribution of the laser beam at its focal point (**Figure A1b**) was generated from the dark field image of the beam spot. The distribution curve in the two-dimensional coordinate was obtained by plotting the curve through the largest cross-section of the beam spot (**Figure A1c**, black line: profile curve). By fitting the distribution curve into the Gaussian function (**Figure A1c**, red line: fit curve) using

equation (A 1), the σ value was obtained. Therefore, FWHM can be calculated by equation (A 2).

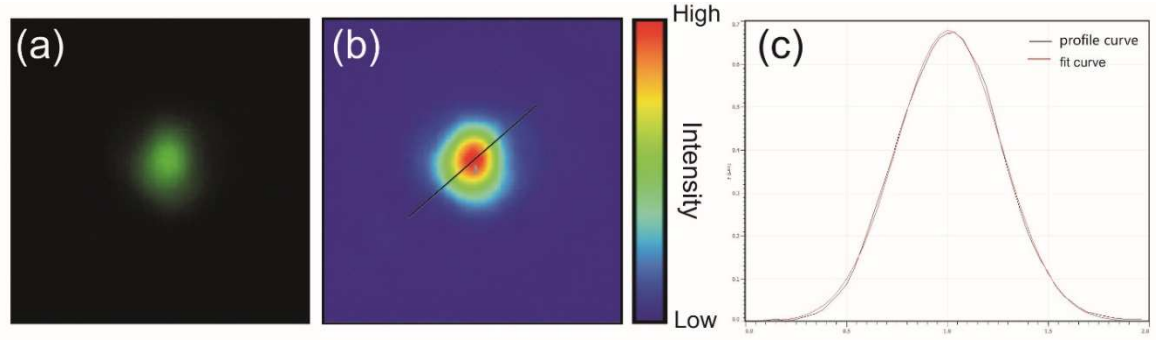

Figure A1 | Measurement of the laser beam diameter. (a) Dark field image of the reflection of the beam spot at its focal point. (b) The intensity distribution of the beam spot at the focal point. The solid black line indicates the largest cross-section of the spot. (c) The plotted 2D intensity curve (black line) and fitted curve as a Gaussian function (red line). As a result, σ is calculated as 256 nm; therefore, FWHM = 604 nm in this case

Simulation of temperature distribution

The finite element method (FEM), or finite element analysis (FEA), is a computational technique used to obtain approximate solutions of boundary value problems in engineering. The whole problem domain is divided into an equivalent system of many smaller bodies or units (finite elements) that are interconnected at points which are common to two or more elements (nodes or nodal points) and boundary lines or surfaces. The individual equation for defined boundary conditions between each element is solved. Therefore, many simple element equations over many small subdomains are connected to approximate a more complex equation over a larger domain. In this work, the steady-state heat distribution around a gold nanoparticle upon irradiation with a CW laser beam was numerically calculated using finite-element analysis by COMSOL Multiphysics software 4.3a. In the heat transfer module, the surrounding medium and AuNPs were modeled as spheres with radium R_{medium}(10 µm)>>R_{AuNP}(80 nm). The outer boundary of the medium sphere is thermally insulated. The heat transfer equation was simplified into:

$$\rho(\boldsymbol{r})C_p(\boldsymbol{r})\frac{\partial T(\boldsymbol{r},t)}{\partial t} - \nabla k(\boldsymbol{r})\nabla T(\boldsymbol{r},t) = Q \quad \text{(A 3)},$$

where $\rho(\vec{r})$=19320 kg/m^3 is the mass density of gold, $C_p(\vec{r})$ = 0.128 J/(kg·K) is the heat capacity of gold at a constant pressure, $k(\vec{r})$=317 W/(m·K) is the thermal conductivity of gold, and $\vec{r}$ and t are the spatial coordinates and time, respectively. Q is the laser power density per gold volume (W/m^3):

$$Q = \frac{P}{V_{AuNP}} \quad \text{(A 4)},$$

where V_{AuNP} (m^3) the volume of a gold nanoparticle, and P is the laser power that is exerted on each gold nanoparticle, which is connected to the beam diameter value and obtained by integrating the 2D Gaussian function:

$$P = \int_{-\frac{l}{2}}^{\frac{l}{2}}\int_{-\frac{l}{2}}^{\frac{l}{2}} f(x,y)\,dx\,dy \quad \text{(A 5)}$$

where $f(x,y)$ is the 2D Gaussian function (equation(A 1), l is the length of an imaginary square which has the same value of area as C_{abs} , the absorption cross-section of a gold nanoparticle. For a gold nanoparticle with a diameter of 80 nm, the absorption cross-section can be determined by the Mie theory simulation ($C_{abs} = 0.01825\ nm^2$). Therefore:

$$l = \sqrt{C_{abs}} \quad \text{(A 6)}$$

The reason for using $[-\frac{l}{2}, \frac{l}{2}]$ as an integration range instead of the radius of absorption cross-section of a gold nanoparticle $[-\sqrt{\frac{C_{abs}}{\pi}}, \sqrt{\frac{C_{abs}}{\pi}}\ ]$ is that a larger area is involved in the calculation for the latter case, which will result in the overestimation of the calculated

laser power at the gold nanoparticle. A schematic diagram of this explanation is shown in **Figure A2**.

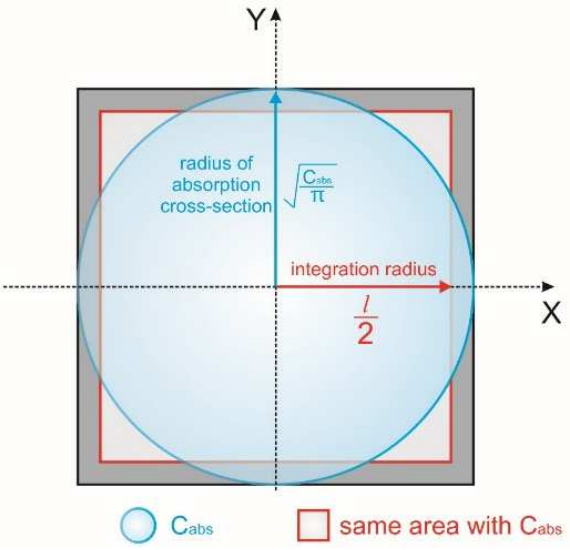

Figure A2 | Integration area of calculating the laser power at a single gold nanoparticle. The blue circle coved area indicates the absorption cross-section of the gold nanoparticle. However, when integrating the 2D Gaussian function, the radius of the absorption cross-section should not be used as the integration range since this will result in a larger calculated area (dark square). Instead, an imaginary square (red square) that has the same area with the absorption cross-section is created and the length of this square should be the correct integration range.

(B) Optical Forces

The calculation of the optical forces that are exerted on a gold nanoparticle (80 nm) by a focused laser beam ($\lambda = 532$ nm) is based on the theory that is described in Section 2.1.3. The force equations were solved with the software 'Mathematica 9.0' by Wolfram Research.

For a focused Gaussian laser beam in cylindrical coordinates as shown in **Figure B1**, the mathematical expression for the electric field follows the equation:

$$\mathbf{E}(\boldsymbol{r}, z) = \mathbf{E_0}\sqrt{\frac{2}{\pi}}\frac{w_0}{w(z)}e^{-\frac{r^2}{w(z)^2}}e^{-i\left[kz+k\frac{r^2}{2R(z)}-\psi(z)\right]} \quad \text{(B 1)}$$

where $k = 2\pi n/\lambda$ is the wave vector, $\mathbf{E_0} = \sqrt{2\mu_0 c_o P}/w_0$ is the maximum amplitude of the electric field in focus with $\mu_0 = 4\pi \times 10^{-7}\ \mathrm{N/A^2}$ as the vacuum permeability, c_o as the speed of light in a vacuum, P as the applied laser power, and where $w_0 = \lambda/\pi\mathrm{NA}$ the waist size (NA is the numerical aperture of the objective lens). $w(z)$ is the width (radius) of the beam along the z-axis direction:

$$\mathrm{w(z)} = w_0\sqrt{1 + (z/z_R)^2} \quad \text{(B 2)}$$

where $z_R = \pi w_0^2/\lambda$, the Rayleigh distance, which is the length along the propagation direction of a beam from the focal point to the place where the area of the cross-section is doubled[176]. R(z) is the radius of curvature as a function of distance along the beam and $\psi(z)$ is called the Gouy phase at the z-axis, and is given by[177]

$$\mathrm{R(z)} = \mathrm{z}[1 + (z_R/z)] \quad \text{(B 3)}$$

$$\psi(z) = arctan(z/z_R) \quad \text{(B 4)}$$

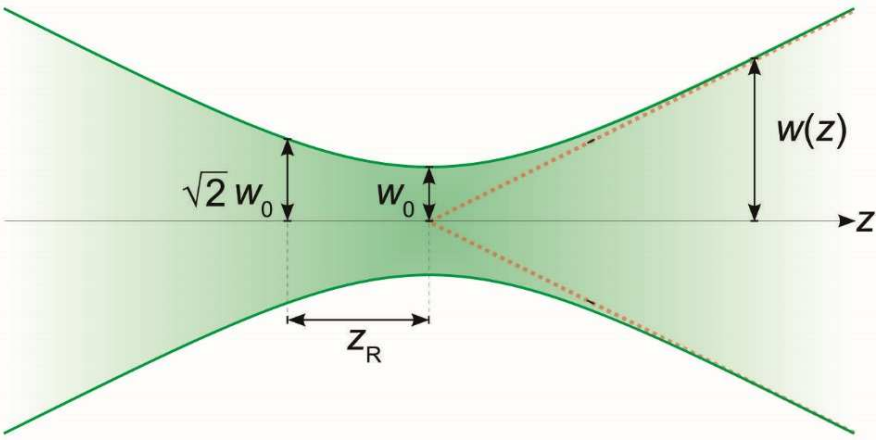

Figure B1 | The focused Gaussian laser beam in cylindrical coordinates.

Combining equation (B 1) and the total force expression in equation (2.18), '$\mathbf{F}_{\boldsymbol{Total}} = \frac{1}{4}\varepsilon_0\varepsilon_m\alpha'\nabla(\mathbf{E}^*\mathbf{E}) + \frac{1}{2}\varepsilon_0\varepsilon_m\alpha'' Im\{\sum_{i=x,y,z}\mathbf{E}_i^*\nabla\mathbf{E}\}$', we obtain the expression for the gradient force and scattering force in the radial r- and z-directions:

$$F_{grad}^{r}(r,z) = -\frac{2\varepsilon_0}{\pi}\alpha_{Re}E_0^2\frac{rw_0^2}{w(z)^4}e^{-\frac{2r^2}{w(z)^2}} \tag{B 5}$$

$$F_{grad}^{z}(r,z) = -\frac{\varepsilon_0}{\pi}\alpha_{Re}E_0^2\frac{zw_0^4}{z_0^2}\left(\frac{1}{w(z)^4} - \frac{2r^2}{w(z)^6}\right)e^{-\frac{2r^2}{w(z)^2}} \tag{B 6}$$

$$F_{scat}^{r}(r,z) = \frac{\varepsilon_0}{\pi}\alpha_{Im}E_0^2\frac{rw_0^2}{w(z)^2}\frac{kr}{R(z)}e^{-\frac{2r^2}{w(z)^2}} \tag{B 7}$$

$$F_{scat}^{z}(r,z) = \frac{\varepsilon_0}{\pi}\alpha_{Im}E_0^2\frac{w_0^2}{w(z)^2}\left[k\left(1 - \frac{r^2(z^2-z_0^2)}{2(z^2+z_0^2)^2}\right) + \frac{w_0^2}{z_0w_0^2}\right]e^{-\frac{2r^2}{w(z)^2}} \tag{B 8}$$

(C) Fourier-Based Solution of the Langevin Equation

In Chapter 4, the cell is exposed to a series of force pulses generated locally in the vicinity of the cell body. These forces were then picked up by the intracellular gold nanoparticles and induce the vibration of these particles. To probe the values of these time-dependent driving forces, firstly, the displacement of the intracellular particles $x(t)$ is analyzed by the Langevin equation under the assumption that only viscous drag force and thermal force are considered

$$m\ddot{x} = -\gamma\dot{x} + F_{thermal}(t) + F_s\,. \tag{C 1}$$

Here m denotes the mass of gold nanoparticle, γ the viscous friction coefficient, $\xi(t)$ the thermal random force and F_s the system force, i.e. the force applied on the detectors.

Equation (C 1) cannot be solved in a standard way due to the presence of the stochastic force $F_{thermal}(t)$. However, the solution can be found through the average power spectral density

$$\langle S_x(f)\rangle = \frac{\langle \hat{x}(f)\hat{x}(f)^*\rangle}{t_{msr}}, \tag{C 2}$$

Where $\langle \dots \rangle$ denotes the expectation value, $S_x(f)$ the signal strength detected in Fourier space and t_{msr} the total measurement time. * represents the complex conjugate. In order to build a connection between equation (C 2) and the Langevin equation, equation (C 1) is Fourier transformed

$$m\hat{\ddot{x}}(f) = -\gamma\hat{\dot{x}}(f) + \hat{F}_{thermal}(f) + \hat{F}_s\,, \tag{C 3}$$

and use following expression

$$\hat{\dot{x}}(f) = i2\pi f\hat{x}(f)\,, \tag{C 4}$$

$$\hat{\ddot{x}}(f) = -(2\pi)^2 f^2 \hat{x}(f), \tag{C 5}$$

leads to the expression

$$\hat{x}(f) = \frac{\hat{F}_{thermal}(f) + \hat{F}_s(f)}{i2\pi\gamma f - (2\pi)^2 f^2 m}. \tag{C 6}$$

Now, inserting equation (C 6) into (C 3) provides

$$\langle S_x(f) \rangle = \frac{1}{t_{msr}} \cdot \frac{\langle \hat{F}_{thermal}(f)^2 \rangle + \langle \hat{F}_s(f)^2 \rangle + \langle \hat{F}_{thermal}(f) \rangle \cdot \langle \hat{F}_s(f) \rangle}{(2\pi f)^4 m^2 + (2\pi\gamma f)^2}. \tag{C 7}$$

Since the gold nanoparticles are in the low Reynolds number liquid (i.e., the velocity is thermally relaxed at each instant of time), the inertial term $m\ddot{x}$ can be neglected[178]. Thus, equation (C 7) simplifies to

$$\langle S_x(f) \rangle \approx \frac{\langle \hat{F}_{thermal}(f)^2 \rangle + \langle \hat{F}_s(f)^2 \rangle + \langle \hat{F}_{thermal}(f) \rangle \cdot \langle \hat{F}_s(f) \rangle}{t_{msr} \cdot (2\pi\gamma f)^2}. \tag{C 8}$$

Now, the Fourier transformed systematic force $\hat{F}_s(f)$ must be found. In the study presented in Chapter 4, this force is assumed to be proportional to the laser power and is a repeated step function which can be written as

$$F_s(t) = F_s \sum_{k=0}^{N-1} h(t - k t_{osc}), \tag{C 9}$$

where

$$h(t) = H(t) - H(t - \frac{t_{osc}}{2}) \tag{C 10}$$

with $t_{osc} = 2\pi/f_{chopper}$ being the chopper period length and $H(t)$ the Heaviside step function. *N* is the number of oscillations (total pulse number). The Fourier transform of $F_s(t)$ reads:

$$\begin{aligned}\hat{F}_s(f) &= F_s \cdot \int_{-\infty}^{\infty} \sum_{k=0}^{N-1} h(t - kt_{osc}) e^{-i2\pi ft} dt \\ &= F_s \cdot \int_{-\infty}^{\infty} [h(t) + h(t - t_{osc}) + \cdots + h(t - (N-1)t_{osc})]\, e^{-i2\pi ft} dt\end{aligned} \tag{C 11}$$

Using the identity[179]

$$\int_{-\infty}^{\infty} h(t-a) e^{-i2\pi ft} dt = e^{-i2\pi fa} \int_{-\infty}^{\infty} h(t) e^{-i2\pi ft} dt \tag{C 12}$$

on each term of equation (C 11) gives:

$$\begin{aligned}\hat{F}_s(f) &= F_s \cdot \left[\int_{-\infty}^{\infty} h(t) e^{-i2\pi ft}\, dt + e^{-i2\pi ft_{osc}} \int_{-\infty}^{\infty} h(t) e^{-i2\pi ft} dt \right. \\ &\qquad \left. + \cdots + e^{-i2\pi f(N-1)t_{osc}} \int_{-\infty}^{\infty} h(t) e^{-i2\pi ft} dt \right] \\ &= F_s \cdot \left(\sum_{k=0}^{N-1} \left(e^{-i2\pi ft_{osc}} \right)^k \right) \int_{-\infty}^{\infty} h(t) e^{-i2\pi ft} dt\end{aligned} \tag{C 13}$$

Using the geometric series expression[179]

$$\sum_{k=0}^{N-1} r^k = \frac{1 - r^N}{1 - r} \tag{C 14}$$

With $N = \frac{t_{msr}}{t_{osc}}$ and plug equation (C 10) into equation (C 13) gives:

$$\hat{F}_s(f) = F_s \cdot \frac{1 - e^{-i2\pi f t_{msr}}}{1 - e^{-i2\pi f t_{osc}}} \cdot \int_{-\infty}^{\infty} \left[H(t) - H\left(t - \frac{t_{osc}}{2}\right) \right] e^{-i2\pi f t} dt$$

$$= F_s \cdot \frac{1 - e^{-i2\pi f t_{msr}}}{1 - e^{-i2\pi f t_{osc}}} \cdot \int_{0}^{\frac{t_{osc}}{2}} e^{-i2\pi f t} dt$$

$$= F_s \cdot \frac{1 - e^{-i2\pi f t_{msr}}}{1 - e^{-i2\pi f t_{osc}}} \cdot \frac{i}{2\pi f} \cdot \left(e^{-i2\pi f t_{osc}} - 1 \right) \quad \text{(C 15)}$$

In the following, $\hat{F}_s(f)^2$ is calculated as:

$$\hat{F}_s(f)^2 = \hat{F}_s(f) \cdot \hat{F}_s(f)^*$$

$$= \frac{{F_s}^2}{(2\pi)^2 f^2} \cdot \frac{1 - e^{-i2\pi f t_{msr}}}{1 - e^{-i2\pi f t_{osc}}} \cdot \frac{1 - e^{i2\pi f t_{msr}}}{1 - e^{i2\pi f t_{osc}}} \cdot \left(e^{-i2\pi f t_{osc}} - 1 \right) \left(e^{i2\pi f t_{osc}} - 1 \right)$$

$$= \frac{{F_s}^2}{(2\pi)^2 f^2} \cdot \left(\frac{1 - cos2\pi f t_{msr}}{1 - cos2\pi f t_{osc}} \right) \cdot (1 - cos\pi f t_{osc})$$

$$= \frac{{F_s}^2}{2\pi^2 f^2} \cdot \left(\frac{sin\, \pi f t_{msr}}{sin\, \pi f t_{osc}} \cdot sin\, \frac{\pi}{2} f t_{osc} \right)$$

$$= \frac{{F_s}^2}{8\pi^2 f^2} \cdot \left(\frac{sin\pi f t_{msr}}{cos\frac{\pi}{2} f t_{osc}} \right)^2 \quad \text{(C 16)}$$

Inserting equation (C 15) and equation (C 16), and using $\langle F_{thermal}(t) \rangle = 0$,[170] the final expression of (C 8) reads:

$$\langle S_x(f) \rangle = \frac{\langle \hat{\xi}(f)^2 \rangle}{t_{msr}(2\pi\gamma f)^2} + \frac{{F_s}^2}{2\gamma^2 t_{msr}(2\pi f)^4} \cdot \left(\frac{sin\pi f t_{msr}}{cos\frac{\pi}{2} f t_{osc}} \right)^2 \quad \text{(C 17)}$$

References

1. Khlebtsov, N.G. and L.A. Dykman, *Optical properties and biomedical applications of plasmonic nanoparticles.* Journal of Quantitative Spectroscopy & Radiative Transfer, 2010. 111(1): p. 1-35.
2. Mie, G., *Articles on the optical characteristics of turbid tubes, especially colloidal metal solutions.* Annalen Der Physik, 1908. 25(3): p. 377-445.
3. Boisselier, E. and D. Astruc, *Gold nanoparticles in nanomedicine: preparations, imaging, diagnostics, therapies and toxicity.* Chemical Society Reviews, 2009. 38(6): p. 1759-1782.
4. Panyala, N.R., E.M. Pena-Mendez, and J. Havel, *Gold and nano-gold in medicine: overview, toxicology and perspectives.* Journal of Applied Biomedicine, 2009. 7(2): p. 75-91.
5. Dykman, L.A. and V.A. Bogatyrev, *Gold nanoparticles: Preparation, functionalisation, applications in biochemistry and immunochemistry.* Uspekhi Khimii, 2007. 76(2): p. 199-213.
6. Dykman, L.A. and N.G. Khlebtsov, *Gold Nanoparticles in Biology and Medicine: Recent Advances and Prospects.* Acta Naturae, 2011. 3(2): p. 34-55.
7. Myroshnychenko, V., J. Rodriguez-Fernandez, I. Pastoriza-Santos, A.M. Funston, C. Novo*, et al.*, *Modelling the optical response of gold nanoparticles.* Chemical Society Reviews, 2008. 37(9): p. 1792-1805.
8. Kang, B., L.A. Austin, and M.A. El-Sayed, *Real-time molecular imaging throughout the entire cell cycle by targeted plasmonic-enhanced Rayleigh/Raman spectroscopy.* Nano Letters, 2012. 12(10): p. 5369-5375.
9. Zeng, S., H.P. Ho, and K.T. Yong, *Nanomaterials enhanced surface plasmon resonance for biological and chemical sensing applications.* Chemical Society Reviews, 2014.
10. Kang, B., L.A. Austin, and M.A. El-Sayed, *Observing Real-Time Molecular Event Dynamics of Apoptosis in Living Cancer Cells using Nuclear-Targeted Plasmonically Enhanced Raman Nanoprobes.* Acs Nano, 2014. 8(5): p. 4883-4892.
11. Kang, B., M.M. Afifi, L.A. Austin, and M.A. El-Sayed, *Exploiting the Nanoparticle Plasmon Effect: Observing Drug Delivery Dynamics in Single Cells via Raman/Fluorescence Imaging Spectroscopy.* Acs Nano, 2013. 7(8): p. 7420-7427.
12. Govorov, A.O. and H.H. Richardson, *Generating heat with metal nanoparticles.* Nano Today, 2007. 2(1): p. 30-38.
13. Baffou, G. and R. Quidant, *Thermo-plasmonics: using metallic nanostructures as nano-sources of heat.* Laser & Photonics Reviews, 2013. 7(2): p. 171-187.

14. Fedoruk, M., M. Meixner, S. Carretero-Palacios, T. Lohmuller, and J. Feldmann, *Nanolithography by Plasmonic Heating and Optical Manipulation of Gold Nanoparticles.* Acs Nano, 2013. 7(9): p. 7648-7653.

15. Pustovalov, V.K., A.S. Smetannikov, and V.P. Zharov, *Photothermal and accompanied phenomena of selective nanophotothermolysis with gold nanoparticles and laser pulses.* Laser Physics Letters, 2008. 5(11): p. 775-792.

16. Xiaohua Huang and M.A. El-Sayed, *Gold nanoparticles: Optical properties and implementations in cancer diagnosis and photothermal therapy.* Journal of Advanced Research, 2010. 1(1): p. 13-28.

17. Kotaidis, V., C. Dahmen, G. von Plessen, F. Springer, and A. Plech, *Excitation of nanoscale vapor bubbles at the surface of gold nanoparticles in water.* Journal of Chemical Physics, 2006. 124(18): p. 1847021-1847027.

18. Siems, A., S.A.L. Weber, J. Boneberg, and A. Plech, *Thermodynamics of nanosecond nanobubble formation at laser-excited metal nanoparticles.* New Journal of Physics, 2011. 13: p. 043018.

19. Lapotko, D., *Optical excitation and detection of vapor bubbles around plasmonic nanoparticles.* Optics Express, 2009. 17(4): p. 2538-2556.

20. Lukianova-Hleb, E., Y. Hu, L. Latterini, L. Tarpani, S. Lee*, et al.*, *Plasmonic Nanobubbles as Transient Vapor Nanobubbles Generated around Plasmonic Nanoparticles.* Acs Nano, 2010. 4(4): p. 2109-2123.

21. Lukianova-Hleb, E.Y., A.P. Samaniego, J. Wen, L.S. Metelitsa, C.C. Chang*, et al.*, *Selective gene transfection of individual cells in vitro with plasmonic nanobubbles.* Journal of Controlled Release, 2011. 152(2): p. 286-293.

22. Urban, A.S., S. Carretero-Palacios, A.A. Lutich, T. Lohmuller, J. Feldmann*, et al.*, *Optical trapping and manipulation of plasmonic nanoparticles: fundamentals, applications, and perspectives.* Nanoscale, 2014. 6(9): p. 4458-4474.

23. Do, J., K.N. Sediq, K. Deasy, D.M. Coles, J. Rodriguez-Fernandez*, et al.*, *Photonic Crystal Nanocavities Containing Plasmonic Nanoparticles Assembled Using a Laser-Printing Technique.* Advanced Optical Materials, 2013. 1(12): p. 946-951.

24. Urban, A.S., A.A. Lutich, F.D. Stefani, and J. Feldmann, *Laser Printing Single Gold Nanoparticles.* Nano Letters, 2010. 10(12): p. 4794-4798.

25. Do, J., R. Schreiber, A.A. Lutich, T. Liedl, J. Rodriguez-Fernandez*, et al.*, *Design and Optical Trapping of a Biocompatible Propeller-like Nanoscale Hybrid.* Nano Letters, 2012. 12(9): p. 5008-5013.

26. Norregaard, K., L. Jauffred, K. Berg-Sorensen, and L.B. Oddershede, *Optical manipulation of single molecules in the living cell.* Physical Chemistry Chemical Physics, 2014. 16(25): p. 12614-12624.

27. Dufes, C., I.F. Uchegbu, and A.G. Schatzlein, *Dendrimers in gene delivery.* Advanced Drug Delivery Reviews, 2005. 57(15): p. 2177-2202.

28. Torchilin, V.P., *Recent advances with liposomes as pharmaceutical carriers.* Nature Reviews Drug Discovery, 2005. 4(2): p. 145-160.

29. Pack, D.W., A.S. Hoffman, S. Pun, and P.S. Stayton, *Design and development of polymers for gene delivery.* Nature Reviews Drug Discovery, 2005. 4(7): p. 581-593.

30. Klein, R.M., E.D. Wolf, R. Wu, and J.C. Sanford, *High-velocity microprojectiles for delivering nucleic acids into living cells. .* Nature, 1987. 327(6117): p. 70-73.

31. Bodles-Brakhop, A.M., R. Heller, and R. Draghia-Akli, *Electroporation for the Delivery of DNA-based Vaccines and Immunotherapeutics: Current Clinical Developments.* Molecular Therapy, 2009. 17(4): p. 585-592.

32. Mitragotri, S., *Innovation - Healing sound: the use of ultrasound in drug delivery and other therapeutic applications.* Nature Reviews Drug Discovery, 2005. 4(3): p. 255-260.

33. Tsukakoshi, M., S. Kurata, Y. Nomiya, Y. Ikawa, and T. Kasuya, *A Novel Method of DNA Transfection by Laser Microbeam Cell Surgery.* Applied Physics B: Lasers and Optics, 1984. 35(3): p. 135-140.

34. Tao, W., J. Wilkinson, E.J. Stanbridge, and M.W. Berns, *Direct Gene-Transfer into Human Cultured-Cells Facilitated by Laser Micropuncture of the Cell-Membrane.* Proceedings of the National Academy of Sciences, 1987. 84(12): p. 4180-4184.

35. Waleed, M., S.U. Hwang, J.D. Kim, I. Shabbir, S.M. Shin*, et al.*, *Single-cell optoporation and transfection using femtosecond laser and optical tweezers.* Biomedical Optics Express, 2013. 4(9): p. 1533-1547.

36. Praveen, B.B., D.J. Stevenson, M. Antkowiak, K. Dholakia, and F.J. Gunn-Moore, *Enhancement and optimization of plasmid expression in femtosecond optical transfection.* Journal of Biophotonics, 2011. 4(4): p. 229-235.

37. Stevenson, D.J., F.J. Gunn-Moore, P. Campbell, and K. Dholakia, *Single cell optical transfection.* Journal of the Royal Society Interface, 2010. 7(47): p. 863-871.

38. Clark, I.B., E.G. Hanania, J. Stevens, M. Gallina, A. Fieck*, et al.*, *Optoinjection for efficient targeted delivery of a broad range of compounds and macromolecules into diverse cell types.* Journal of Biomedical Optics, 2006. 11(1): p. 014034.

39. McDougall, C., D.J. Stevenson, C.T.A. Brown, F. Gunn-Moore, and K. Dholakia, *Targeted optical injection of gold nanoparticles into single mammalian cells.* Journal of Biophotonics, 2009. 2(12): p. 736-743.

40. Kyrsting, A., P.M. Bendix, D.G. Stamou, and L.B. Oddershede, *Heat Profiling of Three-Dimensionally Optically Trapped Gold Nanoparticles using Vesicle Cargo Release.* Nano Letters, 2011. 11(2): p. 888-892.

41. Yao, C.P., R. Rahmanzadeh, E. Endl, Z.X. Zhang, J. Gerdes*, et al.*, *Elevation of plasma membrane permeability by laser irradiation of selectively bound nanoparticles.* Journal of Biomedical Optics,, 2005. 10(6): p. 0640121-0640128.

42. Baffou, G., J. Polleux, H. Rigneault, and S. Monneret, *Super-Heating and Micro-Bubble Generation around Plasmonic Nanoparticles under cw Illumination.* Journal of Physical Chemistry C, 2014. 118(9): p. 4890-4898.

43. Carlson, M.T., A.J. Green, and H.H. Richardson, *Superheating Water by CW Excitation of Gold Nanodots.* Nano Letters, 2012. 12(3): p. 1534-1537.

44. Delcea, M., N. Sternberg, A.M. Yashchenok, R. Georgieva, H. Baumler*, et al.*, *Nanoplasmonics for Dual-Molecule Release through Nanopores in the Membrane of Red Blood Cells.* Acs Nano, 2012. 6(5): p. 4169-4180.

45. Xiong, R., K. Raemdonck, K. Peynshaert, I. Lentacker, I. De Cock*, et al.*, *Comparison of gold nanoparticle mediated photoporation: vapor nanobubbles outperform direct heating for delivering macromolecules in live cells.* Acs Nano, 2014. 8(6): p. 6288-6296.

46. Heinemann, D., M. Schomaker, S. Kalies, M. Schieck, R. Carlson*, et al.*, *Gold Nanoparticle Mediated Laser Transfection for Efficient siRNA Mediated Gene Knock Down.* Plos One, 2013. 8(3): p. e58604.

47. Heinemann, D., M. Schomaker, D. Motekaitis, J. Krawinkel, D. Killian*, et al. Gold nanoparticle mediated cell manipulation using fs and ps laser pulses for cell perforation and transfection*. in *Proceedings of SPIE 7925, Frontiers in Ultrafast Optics: Biomedical, Scientific, and Industrial Applications Xi*. 2011. San Francisco, California, USA.

48. Orsinger, G.V., J.D. Williams, and M. Romanowski, *Focal Activation of Cells by Plasmon Resonance Assisted Optical Injection of Signaling Molecules.* Acs Nano, 2014. 8(6): p. 6151-6162.

49. Wu, T.-H., T. Teslaa, S. Kalim, C.T. French, S. Moghadam*, et al.*, *Photothermal Nanoblade for Large Cargo Delivery into Mammalian Cells.* Analytical Chemistry, 2011. 83(4): p. 1321-1327.

50. Lin, C.P. and M.W. Kelly, *Cavitation and acoustic emission around laser-heated microparticles.* Applied Physics Letters, 1998. 72(22): p. 2800-2802.

51. Hansen, P.M., V.K. Bhatia, N. Harrit, and L. Oddershede, *Expanding the optical trapping range of gold nanoparticles.* Nano Letters, 2005. 5(10): p. 1937-1942.

52. Urban, A.S., T. Pfeiffer, M. Fedoruk, A.A. Lutich, and J. Feldmann, *Single-Step Injection of Gold Nanoparticles through Phospholipid Membranes.* Acs Nano, 2011. 5(5): p. 3585-3590.

53. Howes, P.D., R. Chandrawati, and M.M. Stevens, *Colloidal nanoparticles as advanced biological sensors.* Science, 2014. 346(6205): p. 53.

54. Huefner, A., D. Septiadi, B.D. Wilts, I.I. Patel, W.L. Kuan*, et al.*, *Gold nanoparticles explore cells: Cellular uptake and their use as intracellular probes.* Methods, 2014. 68(2): p. 354-363.

55. Yuan, H., J.K. Register, H.N. Wang, A.M. Fales, Y. Liu*, et al.*, *Plasmonic nanoprobes for intracellular sensing and imaging.* Analytical and Bioanalytical Chemistry, 2013. 405(19): p. 6165-6180.

56. Ohlinger, A., A. Deak, A.A. Lutich, and J. Feldmann, *Optically Trapped Gold Nanoparticle Enables Listening at the Microscale.* Physical Review Letters, 2012. 108(1): p. 0181011-0181015.

57. Janmey, P.A. and C.A. McCulloch, *Cell mechanics: Integrating cell responses to mechanical stimuli.* Annual Review of Biomedical Engineering, 2007. 9: p. 1-34.

58. Bao, G. and S. Suresh, *Cell and molecular mechanics of biological materials.* Nature Materials, 2003. 2(11): p. 715-725.

59. Nikukar, H., S. Reid, P.M. Tsimbouri, M.O. Riehle, A.S.G. Curtis*, et al.*, *Osteogenesis of Mesenchymal Stem Cells by Nanoscale Mechanotransduction.* Acs Nano, 2013. 7(3): p. 2758-2767.

60. Lo, C.M., H.B. Wang, M. Dembo, and Y.L. Wang, *Cell movement is guided by the rigidity of the substrate.* Biophysical Journal, 2000. 79(1): p. 144-152.

61. Ito, Y., T. Kimura, Y. Ago, K. Nam, K. Hiraku*, et al.*, *Nano-vibration effect on cell adhesion and its shape.* Bio-Medical Materials and Engineering, 2011. 21(3): p. 149-158.

62. Ito, Y., T. Kimura, K. Nam, A. Katoh, T. Masuzawa*, et al.*, *Effects of Vibration on Differentiation of Cultured PC12 Cells.* Biotechnology and Bioengineering, 2011. 108(3): p. 592-599.

63. Engler, A.J., S. Sen, H.L. Sweeney, and D.E. Discher, *Matrix elasticity directs stem cell lineage specification.* Cell, 2006. 126(4): p. 677-689.

64. Ingber, D.E., *Mechanobiology and diseases of mechanotransduction.* Annals of Medicine, 2003. 35(8): p. 564-577.

65. Hahn, C. and M.A. Schwartz, *The Role of Cellular Adaptation to Mechanical Forces in Atherosclerosis.* Arteriosclerosis Thrombosis and Vascular Biology, 2008. 28(12): p. 2101-2107.

66. Seol, Y. and K.C. Neuman, *SnapShot: Force Spectroscopy and Single-Molecule Manipulation.* Cell, 2013. 153(5): p. 1168.

67. Neuman, K.C. and A. Nagy, *Single-molecule force spectroscopy: optical tweezers, magnetic tweezers and atomic force microscopy.* Nature Methods, 2008. 5(6): p. 491-505.

68. Alcaraz, J., L. Buscemi, M. Grabulosa, X. Trepat, B. Fabry*, et al.*, *Microrheology of human lung epithelial cells measured by atomic force microscopy.* Biophysical Journal, 2003. 84(3): p. 2071-2079.

69. Hiratsuka, S., Y. Mizutani, M. Tsuchiya, K. Kawahara, H. Tokumoto*, et al.*, *The number distribution of complex shear modulus of single cells measured by atomic force microscopy.* Ultramicroscopy, 2009. 109(8): p. 937-941.

70. Kollmannsberger, P. and B. Fabry, *Linear and Nonlinear Rheology of Living Cells.* Annual Review of Materials Research, 2011. 41: p. 75-97.

71. Kollmannsberger, P. and B. Fabry, *High-force magnetic tweezers with force feedback for biological applications.* Review of Scientific Instruments, 2007. 78(11): p. 1143011-1143016.

72. Balland, M., N. Desprat, D. Icard, S. Fereol, A. Asnacios*, et al.*, *Power laws in microrheology experiments on living cells: Comparative analysis and modeling.* Physical Review E, 2006. 74(2): p. 0219111-20191117.

73. Mas, J., A.C. Richardson, S.N.S. Reihani, L.B. Oddershede, and K. Berg-Sorensen, *Quantitative determination of optical trapping strength and viscoelastic moduli inside living cells.* Physical Biology, 2013. 10(4): p. 0460061-04600610.

74. Mizuno, D., D.A. Head, F.C. MacKintosh, and C.F. Schmidt, *Active and Passive Microrheology in Equilibrium and Nonequilibrium Systems.* Macromolecules, 2008. 41(19): p. 7194-7202.

75. Fischer, M., A.C. Richardson, S.N.S. Reihani, L.B. Oddershede, and K. Berg-Sorensen, *Active-passive calibration of optical tweezers in viscoelastic media.* Review of Scientific Instruments, 2010. 81(1): p. 0151031-01510310.

76. Maier, S.A., *Plasmonics: Fundamentals and Applications*. 2007: Springer Science+Business Media LLC.

77. H. Kuwata, H. Tamaru, K. Esumi, and K. Miyano, *Resonant light scattering from metal nanoparticles: Practical analysis beyond rayleigh approximation.* Applied physics letters, 2003. 83(22): p. 4625–4627.

78. Mie, G., *Beiträge zur Optik trüber Medien, speziell kolloidaler Metallösungen.* Annalen der Physik, 1908. 25(3): p. 377-445.

79. Sergei Yushanov, J.S. Crompton, and K.C. Koppenhoefer. *Mie Scattering of Electromagnetic Waves* in *Expert from the Proceedings of the 2013 COMSOL Conference in Boston*. 2013. Boston.

80. Dienerowitz, M., *Plasmonic effects upon optical trapping of metal nanoparticles*. 2010, the University of St. Andrews.

81. Harris, N., M.J. Ford, and M.B. Cortie, *Optimization of plasmonic heating by gold nanospheres and nanoshells.* J Phys Chem B, 2006. 110(22): p. 10701-10707.

82. Perner, M., S. Gresillon, J. Marz, G. von Plessen, J. Feldmann*, et al.*, *Observation of hot-electron pressure in the vibration dynamics of metal nanoparticles.* Phys Rev Lett, 2000. 85(4): p. 792-795.

83. Perner, M., P. Bost, U. Lemmer, G. vonPlessen, J. Feldmann*, et al.*, *Optically induced damping of the surface plasmon resonance in gold colloids.* Physical Review Letters, 1997. 78(11): p. 2192-2195.

84. Perner, M., S. Gresillon, J. Marz, G. von Plessen, J. Feldmann*, et al.*, *Observation of hot-electron pressure in the vibration dynamics of metal nanoparticles.* Physical Review Letters, 2000. 85(4): p. 792-795.

85. Link, S. and M.A. El-Sayed, *Shape and size dependence of radiative, non-radiative and photothermal properties of gold nanocrystals.* International Reviews in Physical Chemistry, 2000. 19(3): p. 409-453.

86. Fann, W.S., R. Storz, H.W. Tom, and J. Bokor, *Electron thermalization in gold.* Phys Rev B Condens Matter, 1992. 46(20): p. 13592-13595.

87. Sun, C., F. Vallee, L.H. Acioli, E.P. Ippen, and J.G. Fujimoto, *Femtosecond-tunable measurement of electron thermalization in gold.* Phys Rev B Condens Matter, 1994. 50(20): p. 15337-15348.

88. Hodak, J., I. Martini, and G.V. Hartland, *Ultrafast study of electron-phonon coupling in colloidal gold particles.* Chemical Physics Letters, 1998. 284(1-2): p. 135-141.

89. Schoenlein, R.W., W.Z. Lin, J.G. Fujimoto, and G.L. Eesley, *Femtosecond Studies of Nonequilibrium Electronic Processes in Metals.* Physical Review Letters, 1987. 58(16): p. 1680-1683.

90. Elsayedali, H.E., T. Juhasz, G.O. Smith, and W.E. Bron, *Femtosecond Thermoreflectivity and Thermotransmissivity of Polycrystalline and Single-Crystalline Gold-Films.* Physical Review B, 1991. 43(5): p. 4488-4491.

91. Hu, M. and G.V. Hartland, *Heat dissipation for Au particles in aqueous solution: Relaxation time versus size.* Journal of Physical Chemistry B, 2002. 106(28): p. 7029-7033.

92. Baffou, G. and H. Rigneault, *Femtosecond-pulsed optical heating of gold nanoparticles.* Physical Review B, 2011. 84(3): p. 0354151-03541513.

93. Kitz, M., S. Preisser, A. Wetterwald, M. Jaeger, G.N. Thalmann*, et al.*, *Vapor bubble generation around gold nanoparticles and its application to damaging of cells.* Biomedical Optics Express, 2011. 2(2): p. 291-304.

94. Wagner, D.S., N.A. Delk, E.Y. Lukianova-Hleb, J.H. Hafner, M.C. Farach-Carson*, et al.*, *The in vivo performance of plasmonic nanobubbles as cell theranostic agents in zebrafish hosting prostate cancer xenografts.* Biomaterials, 2010. 31(29): p. 7567-7574.

95. Yao, C.P., R. Rahmanzadeh, E. Endl, Z.X. Zhang, J. Gerdes*, et al.*, *Elevation of plasma membrane permeability by laser irradiation of selectively bound nanoparticles.* Journal of Biomedical Optics, 2005. 10(6): p. 0640121-0640128.

96. Lukianova-Hleb, E.Y., A.P. Samaniego, J.G. Wen, L.S. Metelitsa, C.C. Chang*, et al.*, *Selective gene transfection of individual cells in vitro with plasmonic nanobubbles.* Journal of Controlled Release, 2011. 152(2): p. 286-293.

97. Anderson, L.J.E., E. Hansen, E.Y. Lukianova-Hleb, J.H. Hafner, and D.O. Lapotko, *Optically guided controlled release from liposomes with tunable plasmonic nanobubbles.* Journal of Controlled Release, 2010. 144(2): p. 151-158.

98. Eghtedari, M., A. Oraevsky, J.A. Copland, N.A. Kotov, A. Conjusteau*, et al.*, *High sensitivity of in vivo detection of gold nanorods using a laser optoacoustic imaging system.* Nano Letters, 2007. 7(7): p. 1914-1918.

99. Huhn, D., A. Govorov, P.R. Gil, and W.J. Parak, *Photostimulated Au Nanoheaters in Polymer and Biological Media: Characterization of Mechanical Destruction and Boiling.* Advanced Functional Materials, 2012. 22(2): p. 294-303.

100. Fang, Z., Y.R. Zhen, O. Neumann, A. Polman, F.J. Garcia de Abajo*, et al.*, *Evolution of light-induced vapor generation at a liquid-immersed metallic nanoparticle.* Nano Letters, 2013. 13(4): p. 1736-1742.

101. Caupin, F. and E. Herbert, *Cavitation in water: a review.* Comptes Rendus Physique, 2006. 7(9-10): p. 1000-1017.

102. Qin, Z. and J.C. Bischof, *Thermophysical and biological responses of gold nanoparticle laser heating.* Chemical Society Reviews, 2012. 41(3): p. 1191-1217.

103. Harada, Y. and T. Asakura, *Radiation forces on a dielectric sphere in the Rayleigh scattering regime.* Optics Communications, 1996. 124(5-6): p. 529-541.

104. Wright, W.H., G.J. Sonek, and M.W. Berns, *Parametric Study of the Forces on Microspheres Held by Optical Tweezers.* Applied Optics, 1994. 33(9): p. 1735-1748.

105. Nieminen, T.A., V.L.Y. Loke, A.B. Stilgoe, G. Knoner, A.M. Branczyk*, et al.*, *Optical tweezers computational toolbox.* Journal of Optics a-Pure and Applied Optics, 2007. 9(8): p. S196-S203.

106. Loudon, R. and S.M. Barnett, *Theory of the radiation pressure on dielectric slabs, prisms and single surfaces.* Optics Express, 2006. 14(24): p. 11855-11869.

107. De, M., P.S. Ghosh, and V.M. Rotello, *Applications of Nanoparticles in Biology.* Advanced Materials, 2008. 20(22): p. 4225-4241.

108. Murphy, C.J., A.M. Gole, J.W. Stone, P.N. Sisco, A.M. Alkilany*, et al.*, *Gold Nanoparticles in Biology: Beyond Toxicity to Cellular Imaging.* Accounts of Chemical Research, 2008. 41(12): p. 1721-1730.

109. Urban, A.S., S. Carretero-Palacios, A.A. Lutich, T. Lohmuller, J. Feldmann*, et al.*, *Optical trapping and manipulation of plasmonic nanoparticles: fundamentals, applications, and perspectives.* Nanoscale, 2014. 6(9): p. 4458-4474.

110. Stevenson, D.J., F. Gunn-Moore, and K. Dholakia, *Light forces the pace: optical manipulation for biophotonics.* Journal of Biomedical Optics, 2010. 15(4): p. 041503.

111. Ramser, K. and D. Hanstorp, *Optical manipulation for single-cell studies.* Journal of Biophotonics, 2010. 3(4): p. 187-206.

112. Urban, P., S.R. Kirchner, C. Muhlbauer, T. Lohmuller, and J. Feldmann, *Reversible control of current across lipid membranes by local heating.* Scientific Reports, 2016. 6: p. 226861-226867.

113. Alberts B, J.A., Lewis J, *Molecular Biology of the Cell*. 4th ed. The Lipid Bilayer. 2002, New York: Garland Science.

114. Karp, G., *Cell and Molecular Biology: Concepts and Experiments*. 6th ed. 2010: John Wiley & Sons, Inc.

115. Zhao, F., Y. Zhao, Y. Liu, X.L. Chang, C.Y. Chen*, et al.*, *Cellular Uptake, Intracellular Trafficking, and Cytotoxicity of Nanomaterials.* Small, 2011. 7(10): p. 1322-1337.

116. Ishimoto, H., K. Yanagihara, N. Araki, H. Mukae, N. Sakamoto*, et al.*, *Single-cell observation of phagocytosis by human blood dendritic cells.* Jpn J Infect Dis, 2008. 61(4): p. 294-297.

117. Rappoport, J.Z., *Focusing on clathrin-mediated endocytosis.* Biochem J, 2008. 412(3): p. 415-423.

118. Khan, J.A., B. Pillai, T.K. Das, Y. Singh, and S. Maiti, *Molecular effects of uptake of gold nanoparticles in HeLa cells.* Chembiochem, 2007. 8(11): p. 1237-1240.

119. Brandenberger, C., C. Muhlfeld, Z. Ali, A.G. Lenz, O. Schmid*, et al.*, *Quantitative evaluation of cellular uptake and trafficking of plain and polyethylene glycol-coated gold nanoparticles.* Small, 2010. 6(15): p. 1669-1678.

120. Dausend, J., A. Musyanovych, M. Dass, P. Walther, H. Schrezenmeier*, et al.*, *Uptake mechanism of oppositely charged fluorescent nanoparticles in HeLa cells.* Macromol Biosci, 2008. 8(12): p. 1135-1143.

121. Lin, J.Q., H.W. Zhang, Z. Chen, and Y.G. Zheng, *Penetration of Lipid Membranes by Gold Nanoparticles: Insights into Cellular Uptake, Cytotoxicity, and Their Relationship.* Acs Nano, 2010. 4(9): p. 5421-5429.

122. Chithrani, B.D., A.A. Ghazani, and W.C.W. Chan, *Determining the size and shape dependence of gold nanoparticle uptake into mammalian cells.* Nano Letters, 2006. 6(4): p. 662-668.

123. Ghosh, P., G. Han, M. De, C.K. Kim, and V.M. Rotello, *Gold nanoparticles in delivery applications.* Advanced Drug Delivery Reviews, 2008. 60(11): p. 1307-1315.

124. Dykman., L.A. and N.G. Khlebtsov., *Uptake of Engineered Gold Nanoparticles into Mammalian Cells.* Chemical Reviews, 2014. 114(2): p. 1258-1288.

125. Weihs, D., T.G. Mason, and M.A. Teitell, *Bio-microrheology: A frontier in microrheology.* Biophysical Journal, 2006. 91(11): p. 4296-4305.

126. Levi, V. and E. Gratton, *Exploring dynamics in living cells by tracking single particles.* Cell Biochemistry and Biophysics, 2007. 48(1): p. 1-15.

127. Saxton, M.J. and K. Jacobson, *Single-particle tracking: Applications to membrane dynamics.* Annual Review of Biophysics and Biomolecular Structure, 1997. 26: p. 373-399.

128. Dupont, A. and D.C. Lamb, *Nanoscale three-dimensional single particle tracking.* Nanoscale, 2011. 3(11): p. 4532-4541.

129. Dix, J.A. and A.S. Verkman, *Crowding effects on diffusion in solutions and cells.* Annual Review of Biophysics, 2008. 37: p. 247-263.

130. Einstein, A., *Investigations on the Theory of the Brownian Movement*. 1956, New York: Dover.

131. A, E., *On the movement of small particles suspended in a stationary liquid demanded by the molecular-kinetic theory of heat.* Annalen der Physik (Leipzig), 1905. 17: p. 549-560.

132. Gal, N., D. Lechtman-Goldstein, and D. Weihs, *Particle tracking in living cells: a review of the mean square displacement method and beyond.* Rheologica Acta, 2013. 52(5): p. 425-443.

133. Saxton, M.J. and K. Jacobson, *Single-particle tracking: applications to membrane dynamics.* Annu. Rev. Biophys. Biomol. Struct., 1997. 26: p. 373-399.

134. Brangwynne, C.P., G.H. Koenderink, F.C. MacKintosh, and D.A. Weitz, *Cytoplasmic diffusion: molecular motors mix it up.* Journal of Cell Biology, 2008. 183(4): p. 583-587.

135. Guo, M., A.J. Ehrlicher, M.H. Jensen, M. Renz, J.R. Moore*, et al.*, *Probing the Stochastic, Motor-Driven Properties of the Cytoplasm Using Force Spectrum Microscopy.* Cell, 2014. 158(4): p. 822-832.

136. Bracewell, R.N., *The Fourier Transform and Its Applications*. 3rd ed. 2000, Boston: McGraw-Hill.

137. Dorf, R.C.T., Ronald J., *Pocket Book of Electrical Engineering Formulas*. 1st ed. Vol. 2016. 1993: CRC Press.

138. Wikipedia. *Nyquist frequency*. 27 March 2016 [cited 2016 31 March]; Available from: https://en.wikipedia.org/wiki/Nyquist_frequency.

139. D. Potts, G.S., and M. Tasche, *Fast Fourier transforms for nonequispaced data: A tutorial*, in *Modern Sampling Theory: Mathematics and Applications*. 2001.

140. Stein, J.Y., *Digital Signal Processing: A Computer Science Perspective*. 2000: Wiley.

141. Wurm, F.M. and D. Hacker, *First CHO genome.* Nature Biotechnology, 2011. 29(8): p. 718-720.

142. Riehemann, K., S.W. Schneider, T.A. Luger, B. Godin, M. Ferrari*, et al.*, *Nanomedicine-Challenge and Perspectives.* Angewandte Chemie International Edition, 2009. 48(5): p. 872-897.

143. Ryu, J.H., S. Lee, S. Son, S.H. Kim, J.F. Leary*, et al.*, *Theranostic nanoparticles for future personalized medicine.* Journal of Controlled Release, 2014. 190: p. 477-484.

144. Sperling, R.A., P. Rivera gil, F. Zhang, M. Zanella, and W.J. Parak, *Biological applications of gold nanoparticles.* Chem Soc Rev, 2008. 37(9): p. 1896-1908.

145. Burda, C., X.B. Chen, R. Narayanan, and M.A. El-Sayed, *Chemistry and properties of nanocrystals of different shapes.* Chemical Reviews, 2005. 105(4): p. 1025-1102.

146. Sperling, R.A. and W.J. Parak, *Surface modification, functionalization and bioconjugation of colloidal inorganic nanoparticles.* Therapeutic Innovation & Regulatory Science, 2013. 47(1): p. 1333-1383.

147. Shukla, R., V. Bansal, M. Chaudhary, A. Basu, R.R. Bhonde*, et al.*, *Biocompatibility of gold nanoparticles and their endocytotic fate inside the cellular compartment: A microscopic overview.* Langmuir, 2005. 21(23): p. 10644-10654.

148. Xie, J., S. Lee, and X.Y. Chen, *Nanoparticle-based theranostic agents.* Advanced Drug Delivery Reviews, 2010. 62(11): p. 1064-1079.

149. Chou, L.Y.T., K. Ming, and W.C.W. Chan, *Strategies for the intracellular delivery of nanoparticles.* Chemical Society Reviews,, 2011. 40(1): p. 233-245.

150. Lee, C.W., M.J. Chen, J.Y. Cheng, and P.K. Wei, *Morphological studies of living cells using gold nanoparticles and dark-field optical section microscopy.* Journal of Biomedical Optics, 2009. 14(3): p. 034016.

151. Pissuwan, D., T. Niidome, and M.B. Cortie, *The forthcoming applications of gold nanoparticles in drug and gene delivery systems.* Journal of Controlled Release, 2011. 149(1): p. 65-71.

152. Ba, H.J., J. Rodriguez-Fernandez, F.D. Stefani, and J. Feldmann, *Immobilization of Gold Nanoparticles on Living Cell Membranes upon Controlled Lipid Binding.* Nano Letters, 2010. 10(8): p. 3006-3012.

153. Cho, E.C., J.W. Xie, P.A. Wurm, and Y.N. Xia, *Understanding the Role of Surface Charges in Cellular Adsorption versus Internalization by Selectively Removing Gold Nanoparticles on the Cell Surface with a I-2/KI Etchant.* Nano Letters, 2009. 9(3): p. 1080-1084.

154. Chen, C.K., M.H. Chang, H.T. Wu, Y.C. Lee, and T.J. Yen, *Enhanced vibrational spectroscopy, intracellular refractive indexing for label-free biosensing and bioimaging by multiband plasmonic-antenna array.* Biosens. Bioelectron., 2014. 60: p. 343-350.

155. Liang, X.J., A.Q. Liu, C.S. Lim, T.C. Ayi, and P.H. Yap, *Determining refractive index of single living cell using an integrated microchip.* Sens. Actuators, A, 2007. 133(2): p. 349-354.

156. Florin, E.L., V.T. Moy, and H.E. Gaub, *Adhesion Forces between Individual Ligand-Receptor Pairs.* Science, 1994. 264(5157): p. 415-417.

157. Carlson, M.T., A.J. Green, and H.H. Richardson, *Superheating Water by CW Excitation of Gold Nanodots.* Nano Letters, 2012. 12(3): p. 1534-1537.

158. Lukianova-Hleb, E.Y., D.S. Wagner, M.K. Brenner, and D.O. Lapotko, *Cell-specific transmembrane injection of molecular cargo with gold nanoparticle-generated transient plasmonic nanobubbles.* Biomaterials, 2012. 33(21): p. 5441-5450.

159. Letfullin, R.R., C. Joenathan, T.F. George, and V.P. Zharov, *Laser-induced explosion of gold nanoparticles: potential role for nanophotothermolysis of cancer.* Nanomedicine, 2006. 1(4): p. 473-480.

160. Petrova, H., M. Hu, and G.V. Hartland, *Photothermal properties of gold nanoparticles.* Zeitschrift Fur Physikalische Chemie-International Journal of Research in Physical Chemistry & Chemical Physics, 2007. 221(3): p. 361-376.

161. Li, M., T. Lohmuller, and J. Feldmann, *Optical injection of gold nanoparticles into living cells.* Nano Letters, 2015. 15(1): p. 770-775.

162. Yamane, D., Y.C. Wu, T.H. Wu, H. Toshiyoshi, M.A. Teitell*, et al.*, *Electrical Impedance Monitoring of Photothermal Porated Mammalian Cells.* Journal of Laboratory Automation, 2014. 19(1): p. 50-59.

163. Wang, Z.X. and L.N. Ma, *Gold nanoparticle probes.* Coordination Chemistry Reviews, 2009. 253(11-12): p. 1607-1618.

164. Jans, H. and Q. Huo, *Gold nanoparticle-enabled biological and chemical detection and analysis.* Chemical Society Reviews,, 2012. 41(7): p. 2849-2866.

165. Akinori Takami , Hideaki Kurita , and S. Koda, *Laser-Induced Size Reduction of Noble Metal Particles.* Journal of Physical Chemistry B, 1999. 103(8): p. 1226-1232.

166. Nyquist, H., *Certain topics in telegraph transmission theory (Reprinted from Transactions of the A. I. E. E., February, pg 617-644, 1928).* Proceedings of the Ieee, 2002. 90(2): p. 280-305.

167. Goychuk, I., *Viscoelastic subdiffusion: From anomalous to normal.* Physical Review E, 2009. 80(4).

168. Mason, T.G. and D.A. Weitz, *Optical Measurements of Frequency-Dependent Linear Viscoelastic Moduli of Complex Fluids.* Physical Review Letters, 1995. 74(7): p. 1250-1253.

169. Lemons, D.S. and A. Gythiel, *Paul Langevin's 1908 paper ''On the theory of Brownian motion''.* American Journal of Physics, 1997. 65(11): p. 1079-1081.

170. Kubo, R., *The fluctuation-dissipation theorem.* Reports on Progress in Physics, 1966. 29(Part I): p. 255-284.

171. Wirtz, D., *Particle-Tracking Microrheology of Living Cells: Principles and Applications.* Annual Review of Biophysics, 2009. 38: p. 301-326.

172. Kuimova, M.K., S.W. Botchway, A.W. Parker, M. Balaz, H.A. Collins*, et al.*, *Imaging intracellular viscosity of a single cell during photoinduced cell death.* Nature Chemistry, 2009. 1(1): p. 69-73.

173. Fushimi, K. and A.S. Verkman, *Low Viscosity in the Aqueous Domain of Cell Cytoplasm Measured by Picosecond Polarization Microfluorimetry.* Journal of Cell Biology, 1991. 112(4): p. 719-725.

174. Mason, T.G., K. Ganesan, J.H. vanZanten, D. Wirtz, and S.C. Kuo, *Particle tracking microrheology of complex fluids.* Physical Review Letters, 1997. 79(17): p. 3282-3285.

175. Igor Goychuk, P.H., *Subdiffusive dynamics in washboard potentials: two different approaches and different universality classes.* Fractional Dynamics, Recent Advances (World Scientific), 2011: p. 305-327.

176. Siegman, A.E., *Lasers*. 1986: University Science Books.

177. Bandres, M.A. and J.C. Gutierrez-Vega, *Ince-Gaussian beams.* Optics Letters, 2004. 29(2): p. 144-146.

178. Goychuk, I. and P. Hanggi, *Anomalous escape governed by thermal 1/f noise.* Physical Review Letters, 2007. 99(20): p. 2006011-2006014.

179. Lindballe, T.B., M.V.G. Kristensen, K. Berg-Sorensen, S.R. Keiding, and H. Stapelfeldt, *Pulsed laser manipulation of an optically trapped bead: Averaging thermal noise and measuring the pulsed force amplitude.* Optics Express, 2013. 21(2): p. 1986-1996.